

TECHNISCHE UNIVERSITÄT MÜNCHEN

Fakultät für Chemie

**Magnetic Resonance Spectroscopic Imaging
of Metabolism and pH
for Tumor Characterization *in vivo*
using Hyperpolarized ^{13}C -labelled Biosensors**

Stephan Maximilian Düwel

Vollständiger Abdruck der von der Fakultät für Chemie
der Technischen Universität München zur Erlangung des akademischen Grades eines

Doktors der Naturwissenschaften (Dr. rer. nat.)

genehmigten Dissertation.

Vorsitzender:

Prof. Dr. Bernd Reif

Prüfer der Dissertation:

1. Prof. Dr. Steffen J. Glaser
2. Prof. Dr. Axel Haase
3. Prof. Dr. Silvio Aime (schriftliche Beurteilung)
Prof. Dr. Markus Schwaiger (mündliche Prüfung)

Die Dissertation wurde am 17.08.2017 bei der Technischen Universität München
eingereicht und durch die Fakultät für Chemie am 09.10.2017 angenommen.

Abstract

Nuclear magnetic resonance (NMR) is based on quantum mechanical interactions between nuclear spins, magnetic fields and radiofrequency waves. This basic physical phenomenon gives rise to a broad spectrum of research fields, ranging as far as from fundamental research in the field of NMR spectroscopy to applied medical research in the field of magnetic resonance imaging (MRI). Dissolution dynamic nuclear polarization (DNP) revolutionized the field of liquid-state NMR by bringing nuclear spins into a hyperpolarized state, temporarily increasing the NMR signal by a factor of more than 10^4 . Carbon magnetic resonance spectroscopic imaging (^{13}C -MRSI) *in vivo* is made possible by the combination of DNP and MRI, establishing the field of metabolic imaging, which allows to non-invasively study metabolism in real-time within living organisms.

In this context, this thesis describes the development and application of new techniques combining methods from the fields of NMR, ^{13}C -MRSI and DNP for the study of tumor metabolism *in vivo*. A highlight of this work is the identification and development of zymonic acid resulting in a novel technique for the imaging of extracellular pH. The presented research consists on the one hand of a combination of methods to study tumor perfusion, metabolism and necrosis for the characterization of tumors and treatment response, and on the other hand of a novel technique for extracellular pH imaging. This work is thus structured into the following two sections:

- An implementation for hyperpolarized imaging of tumor perfusion, metabolism and necrosis using selectively ^{13}C -labeled urea, pyruvate and fumarate, respectively, is presented. *In vivo* experiments demonstrate the utility of this multiparametric imaging method in an orthotopic hepatocellular carcinoma (HCC) model system before and after an intervention by transcatheter arterial embolization (TAE).
- Zymonic acid is identified, synthesized, hyperpolarized and introduced as a novel, selectively ^{13}C -labeled molecule for hyperpolarized imaging of extracellular pH based on pH-dependent changes in chemical shift. *In vitro* investigations in buffer and blood phantoms show the robustness of this approach as a method for imaging of pH. *In vivo* measurements in bladder, kidney and tumor demonstrate the feasibility of this method for preclinical research. An extensive characterization of the biocompatibility and toxicity of zymonic acid further substantiates its potential for clinical translation.

In this work, changes in tumor perfusion, cancer metabolism, necrosis formation and tumor pH are investigated by a combination of existing and novel methods from NMR, ^{13}C -MRSI and DNP; the results underline the importance of continuously expanding imaging methods for a more precise and comprehensive tumor characterization and earlier therapy response evaluation with the aim of selecting, monitoring and individualizing cancer therapies.

Kurzzusammenfassung

Die Kernspinresonanz (engl. NMR) basiert auf der quantenmechanischen Wechselwirkung zwischen Kernspins, Magnetfeldern und Radiowellen. Auf diesem grundlegenden physikalischen Phänomen baut ein breites Spektrum an Forschungsgebieten von der Grundlagenforschung im Bereich der NMR-Spektroskopie bis zur angewandten medizinischen Forschung im Bereich der Magnetresonanzbildgebung (engl. MRI) auf. Die dynamische Kernspinpolarisation (engl. DNP) revolutionierte die NMR in Flüssigkeiten, indem sie Kernspins in einen hyperpolarisierten Zustand bringt und dabei das NMR-Signal vorübergehend um einen Faktor größer 10^4 verstärkt. Die spektroskopische Kohlenstoff-MRI (^{13}C -MRSI) wird *in vivo* durch die Kombination von DNP und MRI ermöglicht und erlaubt als sogenannte metabolische Bildgebung die nicht-invasive Echtzeituntersuchung des Metabolismus lebender Organismen.

In diesem Kontext beschreibt die vorliegende Dissertation die Entwicklung und Anwendung von neuen Techniken zur Untersuchung von Tumormetabolismus *in vivo* durch die Kombination von Methoden aus den Bereichen NMR, ^{13}C -MRSI und DNP. Eine zentrale Entwicklung dieser Arbeit ist die Identifizierung und Entwicklung von Zymonsäure, was zu einer neuartigen Technik für die extrazelluläre pH-Bildgebung führt. Die bearbeiteten Themen bestehen einerseits aus einer Kombination von Methoden zur Untersuchung von Tumorperfusion, -metabolismus und -nekrose mit dem Ziel der Charakterisierung von Tumoren und deren Therapien, und andererseits aus einer neuartigen Technik zur extrazellulären pH-Bildgebung. Die vorliegende Arbeit ist daher in die folgenden zwei Abschnitte gegliedert:

- Eine Methode zur Bildgebung von Tumorperfusion, -metabolismus und -nekrose mittels selektiv ^{13}C -markiertem und hyperpolarisiertem Harnstoff, Pyruvat und Fumarat wird vorgestellt. Der Nutzen dieser multiparametrischen Bildgebungsmethode wird anhand von *in vivo* Experimenten an einem Modellsystem eines orthotopen hepatozellulären Karzinoms (HCC) vor und nach einer Intervention mittels transarterieller Embolisation (TAE) aufgezeigt.
- Zymonsäure wird identifiziert, synthetisiert, hyperpolarisiert und als neues, selektiv ^{13}C -markiertes Molekül für die hyperpolarisierte pH-Bildgebung basierend auf pH-abhängigen Änderungen von chemischen Verschiebungen eingeführt. *In vitro* Untersuchungen in Puffer und Blut zeigen die geringe Störanfälligkeit dieser Methode. *In vivo* Messungen in Blase, Niere und Tumor demonstrieren die Umsetzbarkeit der Methode in der präklinischen Forschung. Eine umfangreiche Charakterisierung der Biokompatibilität und Toxizität von Zymonsäure untermauert das Potential zur klinischen Umsetzung.

In dieser Arbeit werden Änderungen der Tumorperfusion, des Krebszellmetabolismus, der Nekrosebildung und des pH von Tumoren durch eine Kombination von existierenden und neuartigen Methoden aus NMR, ^{13}C -MRSI und DNP untersucht; die Ergebnisse unterstreichen die Bedeutung einer kontinuierlichen Erweiterung von Bildgebungsmethoden für eine präzisere, umfassendere Charakterisierung von Tumoren und für eine frühere Bewertung eines Therapieansprechens mit dem Ziel der Selektion, Überwachung und Individualisierung von Tumorbehandlungen.

Contents

Abstract	i
Kurzzusammenfassung	iii
1 Introduction	1
2 Theory and Methods	5
2.1 Magnetic Resonance Spectroscopic Imaging	6
2.1.1 Signal equation	6
2.1.2 Slice selective two dimensional chemical shift imaging	7
2.2 Hyperpolarization	10
2.2.1 Dissolution Dynamic Nuclear Polarization	11
2.3 Cell death detection using hyperpolarized ^{13}C -fumarate <i>in vivo</i>	12
2.4 pH determination <i>in vivo</i>	16
2.4.1 Chemical exchange and pH-dependent NMR spectra	17
2.4.2 Phosphorus pH spectroscopy <i>in vivo</i>	18
2.4.2.1 Intracellular pH using inorganic phosphate	19
2.4.2.2 Extracellular pH using 3-APP	20
2.4.2.3 Spectra analysis techniques	22
2.4.3 Hyperpolarized pH imaging <i>in vivo</i>	23
2.4.3.1 ^{13}C -bicarbonate	24
2.4.3.2 ^{13}C -zymonic acid	26
3 Multiparametric human hepatocellular carcinoma characterization and therapy response evaluation by hyperpolarized ^{13}C-MRSI	31
Summary	31
3.1 Introduction	32
3.2 Materials and methods	33
3.3 Results	36
3.4 Discussion	39
3.5 Conclusions	43
3.6 Acknowledgements	43
3.7 Appendix A: Supplementary Material	44

4	Imaging of pH <i>in vivo</i> using hyperpolarized ¹³C-labeled zymonic acid	47
	Summary	47
4.1	Introduction	48
4.2	Results	49
	4.2.1 Synthesis and hyperpolarization of ZA	49
	4.2.2 <i>In vitro</i> pH measurement	49
	4.2.3 <i>In vivo</i> probe characterization	50
	4.2.4 <i>In vivo</i> pH measurement in rat bladder	52
	4.2.5 <i>In vivo</i> pH measurement in rat kidneys	52
	4.2.6 <i>In vivo</i> pH measurement in rat tumors	53
4.3	Discussion	55
4.4	Methods	59
	4.4.1 Synthesis of selectively ¹³ C-labeled ZA	59
	4.4.2 Cell experiments	59
	4.4.3 Characterization of ZA	60
	4.4.4 Hyperpolarization with dissolution DNP	61
	4.4.5 Buffer and blood phantom preparation	61
	4.4.6 Spectroscopy and imaging procedure	62
	4.4.7 Animal handling and tumor implantation	62
	4.4.8 Toxicopathological study	63
	4.4.9 Back-calculation of pH values and maps	64
	4.4.10 MALDI mass spectrometry imaging	64
	4.4.11 Phosphor pH reference measurements	65
	4.4.12 Optical and electrode pH reference measurements	65
4.5	Acknowledgments	66
4.6	Author contributions	66
4.7	Competing interests	66
4.8	Appendix A: Supplementary Information	67
5	Conclusion	85
	Bibliography	89
	List of publications	107
	Curriculum vitae	I
	Acknowledgements	V

1 Introduction

“I was not spared the shock which every physicist, accustomed to the classical way of thinking, experienced when he came to know of Bohr’s « basic postulate of quantum theory » for the first time.”

— Wolfgang Pauli (* 1900; † 1958)

The experimental demonstration by *Otto Stern* and *Walther Gerlach* in 1922, that the spatial orientation of angular momenta is quantized [52], was the beginning of an exciting road of a series of experimental realizations of quantum mechanical phenomena. This early discovery was followed by the invention of nuclear magnetic resonance (NMR) in liquids and solids by *Felix Bloch* and *Edward M. Purcell* in 1946 [14, 15, 132], which today has turned into an indispensable standard method for chemical structure determination. A combination of the spin echo method discovered by *Erwin Hahn* in 1950 [64] and the application of linear magnetic field gradients in three-dimensions for the spatial localization of NMR signals, as proposed by *Peter Mansfield* and *Paul C. Lauterbur* in 1973, was the foundation of magnetic resonance imaging (MRI, see also Section 2.1). Due to its non-invasiveness, non-ionizing radiation, excellent soft-tissue contrast and theoretically unlimited number of differing contrasts, MRI has today been established as an indispensable tool in medical diagnostics.

Conceptually, one of the main challenges of MRI is its inherently low sensitivity, resulting from low spin polarization levels at thermal equilibrium due to the small energy difference between nuclear spin states. In traditional proton MRI (^1H -MRI), this limitation is compensated by the high natural abundance and high concentration ($\sim\text{M}$) of protons in the human body. In the case of carbon MRI (^{13}C -MRI), with an even lower sensitivity due to a lower natural abundance and a smaller magnetic moment, this limitation cannot be compensated as easily because of the low *in vivo* concentrations (μM – mM) of the molecules of interest containing ^{13}C nuclei. However, several hyperpolarization techniques allow to temporarily push polarization levels far beyond thermal equilibrium [123]. The most versatile method, dissolution dynamic nuclear polarization (DNP, see also Section 2.2.1), revolutionized the field of liquid-

state NMR by temporarily increasing NMR signals by more than four orders of magnitude above thermal equilibrium [11].

The future fate of DNP and the field of metabolic imaging will largely depend on a successful search for sensor molecules reporting on clinically relevant parameters [10]. Currently, a large number of hyperpolarizable and ^{13}C -labeled molecules are being investigated preclinically. These report on biologically significant parameters as diverse as perfusion, necrosis, metabolism or pH [82]. An even more challenging step is the translation of hyperpolarized ^{13}C -MRSI probes from preclinical settings into the clinic. The preclinically most researched and clinically most promising substance to date is selectively ^{13}C -labeled pyruvate [20, 71]. The conversion of hyperpolarized pyruvate to its downstream metabolites alanine, lactate and bicarbonate allows to probe specific biochemical pathways in real-time and thus to gain new insights into metabolism *in vivo*. A clinical study in prostate cancer patients using hyperpolarized ^{13}C -pyruvate has already produced first results [120]. Recently, promising initial metabolic images of hyperpolarized ^{13}C -pyruvate in the human heart of healthy subjects were reported [31].

Within this context, this work describes the development and application of new techniques for tumor characterization and monitoring of response to treatment *in vivo*. It ranges from a combination of methods for the imaging of tumor perfusion, metabolism and necrosis, to a novel technique for extracellular pH imaging. This thesis is thus structured into two parts:

Multiparametric human hepatocellular carcinoma characterization and therapy response evaluation by hyperpolarized ^{13}C -MRSI

In the first part of this work, a method to image tumor perfusion, metabolism and necrosis using selectively ^{13}C -labeled and hyperpolarized urea, pyruvate and fumarate is implemented and applied *in vivo* (Chapter 3).

Pyruvate and its downstream metabolites lactate and alanine are used for the analysis of *in vivo* glucose metabolism of untreated [6, 20, 58] and treated tumor tissue [34, 35, 127]. Fumarate and its metabolite malate has been evaluated for the detection of early stages of tissue necrosis [16, 17, 51, 109, 167]. When, as a result of necrosis, the cell membrane integrity breaks down, the enzyme fumarase can be accessed by the injected fumarate and is rapidly converted to malate, which in turn is used to quantify the amount of tissue damage (see also Section 2.3). Urea has been demonstrated to be a feasible perfusion agent, since it represents an endogenous, metabolically inactive molecule, which can conveniently be copolarized and injected together with pyruvate [116, 117].

Hepatocellular carcinoma (HCC) represents an ideal tumor model to test multiparametric methods for tumor characterization and therapy response evaluation. HCC belongs to the six most common cancer types in humans and accounts for one-third of cancer-related deaths worldwide [46]. Only a minority of patients with HCC is eligible for curative treatment options (i.e. liver transplantation, surgical resection and tumor ablation) [94–96]. In the case of unresectable HCC, transcatheter arterial chemoembolization (TACE) [104, 161], molecularly targeted therapies, such

as the multikinase inhibitor sorafenib [96, 171], or combinations thereof can be employed. Treating the genetically and molecularly diverse HCC could benefit from a pretherapeutic tumor-specific assessment by selecting the treatment with the best-predicted response. Early response monitoring could help the development of novel therapeutic concepts.

Over recent years, several new imaging techniques have been introduced into HCC management aimed at a comprehensive tumor characterization for therapy response prediction and monitoring. These include a structural and functional analysis by MR-based diffusion imaging [19, 24, 118, 124, 170] and perfusion imaging [12, 170], as well as positron emission tomography (PET)-based metabolic imaging [90, 158]. Up to now, only a small number of studies has explored pyruvate in HCC for tissue characterization [33, 174] or therapy response evaluation [32], or in Myc-driven liver cancer with features of HCC and hepatoblastoma [67].

Recently, hyperpolarized ^{13}C -fumarate was used to quantify and localize necrosis caused by renal injury in an ischemia and reperfusion model in rats [122].

The goal of this study was to test the potential for HCC management by combining the ^{13}C -labeled and hyperpolarized substrates urea, pyruvate and fumarate. For this purpose, hyperpolarized ^{13}C -MR measurements with $[1-^{13}\text{C}]$ pyruvate, $[1,4-^{13}\text{C}_2]$ fumarate and $[^{13}\text{C},^{15}\text{N}_2]$ urea were performed *in vivo* in orthotopic rat HCC before and after an intervention by transcatheter arterial embolization (TAE). While the acquired perfusion and necrosis data show clear trends in response to the treatment, the information derived from the metabolic activity is less conclusive. This work thus emphasizes the relevance of multiparametric techniques for tumor characterization and therapy response evaluation.

Imaging of pH *in vivo* using hyperpolarized ^{13}C -labeled zymonic acid

In the second part of this work, selectively ^{13}C -labeled and hyperpolarized zymonic acid is developed and applied as a novel probe for the imaging of extracellular pH *in vivo* (Chapter 4).

The combination of ^{13}C -MRSI using hyperpolarized ^{13}C -urea, ^{13}C -pyruvate and ^{13}C -fumarate already allows for a first multiparametric characterization of tumors and enables an evaluation of their response to treatment (see Chapter 3). Meanwhile, an important additional parameter is the change in extracellular pH caused by tumors. This circumstance can be used for an even more comprehensive tumor characterization, as well as for treatment response monitoring. Since many cellular processes are highly sensitive to changes in proton concentrations, maintaining acid-base balance is critical for living species. In humans, pH is regulated within a narrow pH range mainly by the bicarbonate buffer system. However, tumors can cause an acidification of their extracellular environment during aerobic glycolysis and increased export of lactic acid, which is an effect that can even be further enhanced by the reduced buffering capacity of tumor interstitial fluid and poor tumor perfusion [79]. Even more general, local deviations from the systemic pH are not only caused by cancer, but also by other pathologies such as inflammation, infection, ischemia, renal failure or pulmonary disease [56].

Because of this potentially broad impact, non-invasive imaging of local pH changes

has been a major goal in biomedical research (see also Section 2.4), even though so far no technique to measure extracellular pH has been applicable in the clinic: The majority of approaches for non-invasive pH imaging focused on MRI because of its high spatial resolution and excellent soft-tissue contrast. In addition, optical methods [66] and radioactive tracers [141] for positron-emission-tomography (PET) have been developed. Magnetic resonance spectroscopy (MRS)-based pH sensor molecules exploit pH-induced changes in NMR parameters, such as chemical shifts of individual atomic nuclei, which are sensitive to the protonation state of the molecule and therefore the surrounding pH [56]; the current gold standard for measuring extracellular pH via MR uses ^{31}P spectroscopy and is described in Section 2.4.2. To increase sensitivity, gadolinium and lanthanide complexes as well as iodinated contrast agents with pH-dependent chemical exchange or relaxation properties were developed [26, 37, 107]. Endogenous amide proton transfer chemical exchange saturation transfer (APT-CEST) experiments [180], utilizing the pH-dependent proton exchange from predominantly intracellular proteins, are currently evaluated to study pH in the brain *in human*. Still, until now a non-invasive clinical method for pH imaging is missing.

Previously, hyperpolarized ^{13}C -bicarbonate has been proposed as a probe for clinical pH imaging [50], but has up to now only been used for preclinical hyperpolarized pH imaging. This technique is based on the determination of pH from the ratio of the $^{13}\text{CO}_2/\text{H}^{13}\text{CO}_3^-$ equilibrium, but although a pioneering idea, it faces a multitude of challenges (see also Section 2.4.3.1).

Recently, other groups have made progress towards developing alternative molecules for hyperpolarized pH imaging as well, also based on pH-dependent chemical shifts (see also Section 2.4.3), including ^{13}C -dicarboxylic acids [86], ^{13}C -Good's buffers [44], and ^{15}N -pyridine derivatives [74]. However, to date these molecules could only be shown to detect pH changes *in vitro*.

A novel probe for MRI of extracellular pH *in vivo* is hyperpolarized $[1,5-^{13}\text{C}_2]$ zymonic acid, presented in this work. It is shown that zymonic acid can be used to non-invasively image extracellular pH both *in vitro* and *in vivo* in bladder, kidneys and a MAT B III tumor model. Zymonic acid is characterized as a non-toxic compound with a long lifetime of its hyperpolarized signal. Furthermore, it is demonstrated that the reported pH is robust towards changes in concentration, temperature, ionic strength and protein concentration, making this extracellular pH sensor primed for further preclinical and clinical studies.

In this work, new imaging methods for non-invasive studies of tumor metabolism and pH are developed and applied *in vivo*, based on an interplay of techniques from the areas of NMR, ^{13}C -MRI and DNP. First, a combination of hyperpolarized imaging methods to study tumor perfusion, cancer metabolism and cell necrosis is presented. Second, zymonic acid is identified and developed as a novel technique which can be used to additionally image the extracellular pH of tumors. The overarching goal of this thesis is the contribution of novel methods to the continuously expanding number of available imaging modalities for more precise and comprehensive tumor characterizations and therapy response evaluations.

2 Theory and Methods

“Historically, the record is clear. Chemistry, for example, was cobbled together from mystical alchemy, metallurgy, physics, mineralogy, medicine, and cookery, eliminating incompatibilities as it evolved and consolidated into a more-or-less unified discipline. Physics has been formed, and enriched, by contributions from astronomy, mechanics, mathematics, chemistry, and other sciences. We have recently observed the rationalization of much of biology by chemistry, with the help of physics.”

— Paul C. Lauterbur (* 1929; † 2007)

Nuclear magnetic resonance (NMR) is based on nuclear spin magnetic moments of nuclei in atoms being influenced by their chemical environment while interacting with external magnetic fields. This can be used to non-destructively study microscopic and macroscopic structures of molecules in liquids and solids. The introduction of spatially varying magnetic field strengths into the field of NMR enables the acquisition of spatially resolved signals, opening up the world of magnetic resonance spectroscopic imaging (MRSI). The method of dissolution dynamic nuclear polarization (DNP) temporarily increases the intrinsically weak NMR signal drastically, allowing a plethora of MRSI methods to be applied for studying metabolism of living organisms, thus taking the field of metabolic imaging to a new level.

This chapter briefly describes the physical basics and fundamental methods of the work covered in this thesis. For in-depth explanations of the underlying phenomena, the reader is referred to standard NMR and MRI textbooks [59, 63, 81, 91] or the literature cited directly in the following sections.

First, the two concepts of magnetic resonance spectroscopic imaging (Section 2.1) and hyperpolarization (Section 2.2), with a focus on dissolution dynamic nuclear polarization (Section 2.2.1), are introduced, before Section 2.3 gives an example of how the two techniques can be applied to a suitable metabolic substrate to detect cell death *in vivo*.

Then, an introduction to central methods for the determination of pH *in vivo* is given (Section 2.4), including the description of chemical exchange as the basis for pH-dependent NMR spectra (Section 2.4.1) and phosphorus spectroscopy as the current gold standard to non-invasively measure pH *in vivo* (Section 2.4.2).

Finally, the two currently available sensors for hyperpolarized *in vivo* pH imaging (Section 2.4.3), ^{13}C -bicarbonate (Section 2.4.3.1) and the novel ^{13}C -labeled *in vivo* pH imaging probe zymonic acid (Section 2.4.3.2), are described.

2.1 Magnetic Resonance Spectroscopic Imaging

One of the conceptually easiest and most robust imaging sequences, which is able to simultaneously collect spatial and spectral information, is the slice selective two dimensional (2D) chemical shift imaging (CSI) sequence (see Fig. 2.1). In brief, this sequence excites nuclear spins selectively from the desired tissue slice of interest (with the coordinate system's z -dimension defined to be perpendicular to this slice), then uses phase encoding both in the x - and y -dimension of the excited slice, before acquiring free induction decays (FIDs) for every point in the reciprocal space. A three dimensional (2D spatial, 1D spectral) Fourier transform then leads to the desired chemical shift spectrum for every point in the image space. Thorough discussions of this sequence can be found in standard MRI textbooks [59, 63, 81, 91].

First, Section 2.1.1 introduces the theoretical concept of the signal equation as the basis of MRSI with data acquired in the reciprocal space, before Section 2.1.2 describes slice selection, phase encoding and characteristic imaging parameters specifically relevant for slice selective two dimensional chemical shift imaging.

2.1.1 Signal equation

In the presence of a static magnetic field with a linearly varying magnetic field strength and gradient $\vec{\nabla}B(\vec{r}) = \vec{G}$, the Larmor frequency ω' of spin $1/2$ -particles with gyromagnetic ratio γ is not only a function of the static magnetic field strength and the particles' chemical environment, but also of their spatial coordinate \vec{r} according to

$$\omega'(\vec{r}) = \omega + \gamma\vec{G} \cdot \vec{r}. \quad (2.1)$$

The magnetic resonance spectroscopic imaging (MRSI) signal equation

$$s(t) \propto \iiint \rho(\vec{r}, \omega) e^{i(\omega + \gamma\vec{G} \cdot \vec{r})t} d^3r d\omega \quad (2.2)$$

then expresses the expected NMR signal as a function of time (the free induction decay, FID) as an integral over the spatial extent and over all chemical shift frequencies in a sample with the spectral spin density $\rho(\vec{r}, \omega)$. By defining the reciprocal

space vector

$$\vec{k}(t) = \frac{\gamma}{2\pi} \int_0^t \vec{G}(t') dt' \quad (2.3)$$

where \vec{G} is the gradient of a linearly varying magnetic field, and by using the relation $\omega = 2\pi f$, the signal equation 2.2 simplifies to the Fourier transform of the spectral spin density according to

$$s(\vec{k}, t) \propto \iiint \rho(\vec{r}, f) e^{i2\pi(ft + \vec{k} \cdot \vec{r})} d^3r df. \quad (2.4)$$

Consequently, the signal $s(\vec{k}, t)$ and the spectral spin density $\rho(\vec{r}, f)$ constitute two functions representing a Fourier transform pair

$$\begin{aligned} s(\vec{k}, t) &\propto \mathcal{F}\{\rho(\vec{r}, f)\} \\ \rho(\vec{r}, f) &\propto \mathcal{F}^{-1}\{s(\vec{k}, t)\} \end{aligned} \quad (2.5)$$

and the desired spectral spin density $\rho(\vec{r}, f)$ can thus be calculated from the acquired signal $s(\vec{k}, t)$ by the inverse Fourier transform

$$\rho(\vec{r}, f) \propto \iiint s(\vec{k}, t) e^{-i2\pi(ft + \vec{k} \cdot \vec{r})} d^3k dt. \quad (2.6)$$

2.1.2 Slice selective two dimensional chemical shift imaging

The addition of a slice selective excitation pulse can reduce the dimensionality of the inverse Fourier transform from four to three dimensions, and thus drastically reduce the number of FIDs that need to be collected in the reciprocal space and consequently also significantly reduce the total time needed to acquire a 2D magnetic resonance spectroscopy image.

Slice selection. With a spatially varying magnetic field strength, linear in the z -dimension only and with gradient $\vec{\nabla}B(\vec{r}) = G_z \vec{z}$, equation 2.1 relating Larmor frequency and gradient strength reduces to

$$\omega'(z) = \omega + \gamma G_z z. \quad (2.7)$$

A radiofrequency (RF) excitation pulse of bandwidth $\Delta\omega'$, meaning that this pulse only excites spins within a range $\Delta\omega'$ of frequencies, then only excites spins within a slice perpendicular to the z -dimension with slice thickness

$$\Delta z = \frac{\Delta\omega'}{\gamma G_z}. \quad (2.8)$$

An RF pulse in shape of a sinc-function, $\text{sinc}(t) = \sin(t)/t$, can conveniently be used to excite spins in a tissue slice, as it leads to a nearly rectangular excitation profile in the z -dimension. With the bandwidth $\Delta\omega'$ of a sinc-pulse being inversely propor-

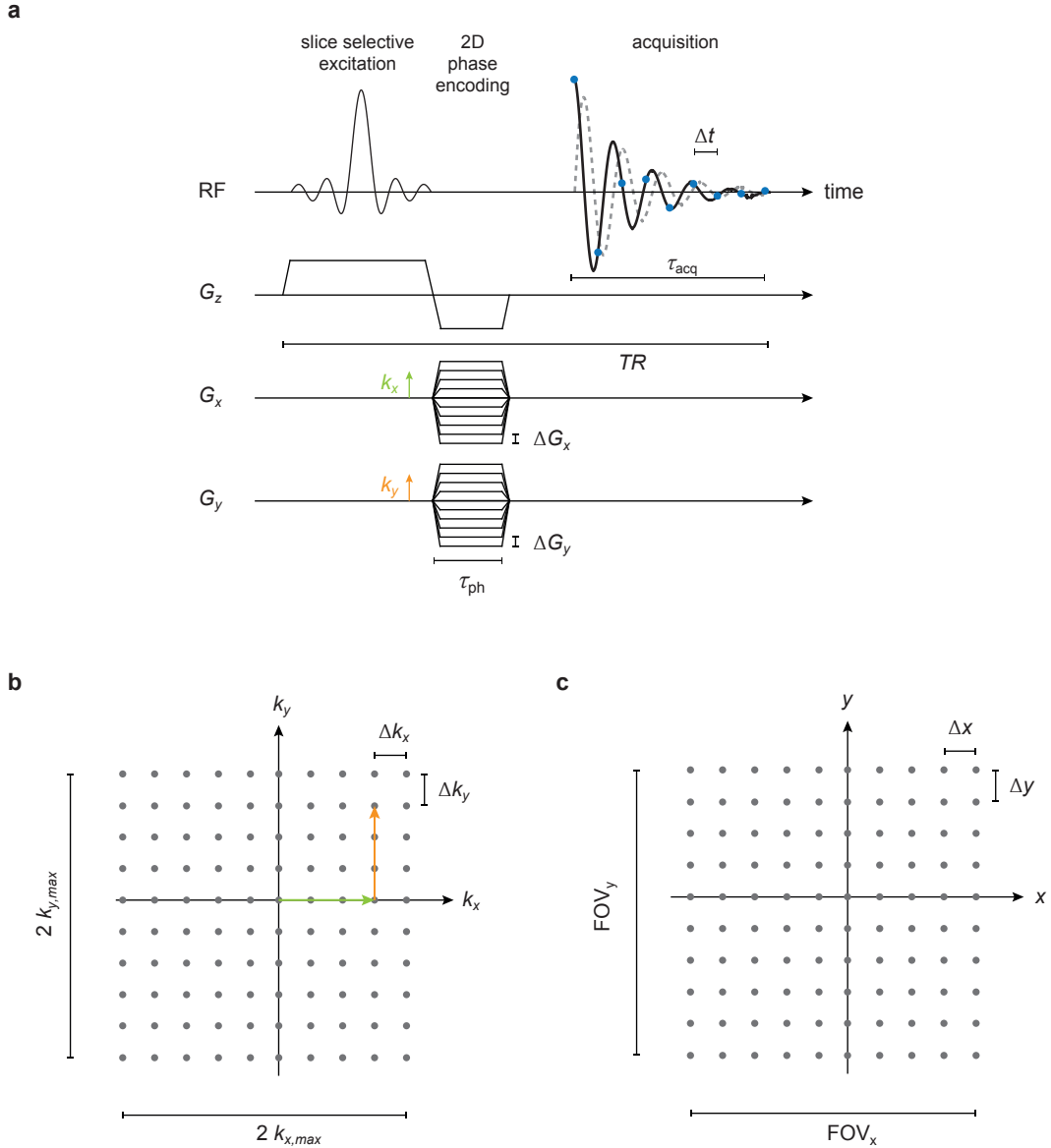


Figure 2.1: Magnetic resonance spectroscopic imaging (MRSI) with a slice selective two dimensional (2D) chemical shift imaging (CSI) sequence. (a) The sequence diagram shows an excitation using a slice selective radiofrequency sinc-pulse, a two dimensional phase encoding in the x/y -direction of duration τ_{ph} , and a signal acquisition of the real (solid) and imaginary (dashed) part of the free induction decay (FID), with a sampling frequency of $1/\Delta t$ and an acquisition time τ_{acq} . (b) Repeatedly iterating over the sequence in **a** with a repetition time TR and different phase encodings by the application of varying gradient strengths $G_{x/y}$, an FID is recorded at every coordinate (k_x, k_y) in the reciprocal space (k -space). (c) A Fourier transformation from the reciprocal space shown in **b** to the real space (image-space) results in a spin density spectrum as a function of frequency/chemical shift at every coordinate (x, y) . RF, radiofrequency; G_z , slice selective gradient in z -direction; $G_{x/y}$, phase encoding gradient in x/y -direction; $\text{FOV}_{x/y}$, field of view in x/y -direction.

tional to the duration τ_p of the pulse, $\Delta\omega' \propto 1/\tau_p$, it is evident from equation 2.7 that a desired slice thickness can be achieved by choosing the appropriate gradient strength G_z and pulse length τ_p .

2D-spatial encoding and 1D-spectral encoding. After a slice selective excitation of a slice perpendicular to the z -dimension, the application of a linear magnetic field gradient in the x/y -dimension $\vec{\nabla}B(\vec{r}) = G_x\vec{x} + G_y\vec{y}$ of duration τ_{ph} before the acquisition of a free induction decay allows us to simplify equation 2.1 (relating Larmor frequency and gradient strength) and equation 2.3 (defining the reciprocal space vector) to

$$\omega'(x, y) = \omega + \gamma(G_x x + G_y y) \quad (2.9)$$

$$\vec{k} = \frac{\gamma}{2\pi}(G_x\vec{x} + G_y\vec{y})\tau_{ph}. \quad (2.10)$$

With these two relations and the omission of the third spatial dimension because of the aforementioned slice selection perpendicular to the z -dimension, we can explicitly give a reduced dimensionality analog of the Fourier transform pair 2.4 and 2.6 by

$$s(k_x, k_y, t) \propto \iiint \rho(x, y, f) e^{i2\pi(ft + k_x x + k_y y)} dx dy df \quad (2.11)$$

$$\rho(x, y, f) \propto \iiint s(k_x, k_y, t) e^{-i2\pi(ft + k_x x + k_y y)} dk_x dk_y dt. \quad (2.12)$$

The acquisition of a free induction decay signal $s(k_x, k_y, t)$ as a function of time t at every point (k_x, k_y) in k -space (see Fig. 2.1) thus allows us to calculate the underlying, spatially resolved spectral spin density $\rho(x, y, f)$, by application of a three dimensional (2D-spatial and 1D-spectral) inverse Fourier transform as given by equation 2.12.

Characteristic chemical shift imaging parameters. Several essential image properties are related to fundamental parameters of the acquisition sequence, owing to the in practice discrete instead of continuous sampling of the k -space and of the free induction decay signal (see Fig. 2.1). The maximum spatial extent, from which signals can be acquired in real space, is commonly called the field of view (FOV). For the case of a two dimensional phase encoding, it is governed by the step size $\Delta k_{x/y}$ in the reciprocal space by

$$FOV_{x/y} = \frac{1}{\Delta k_{x/y}} = \frac{2\pi}{\gamma \Delta G_{x/y} \tau_{ph}}. \quad (2.13)$$

Thus, to acquire signals from larger samples, an acquisition with smaller step sizes $\Delta k_{x/y}$ in the reciprocal space is needed, which can be achieved by smaller gradient step sizes $\Delta G_{x/y}$ and/or shorter phase encoding durations τ_{ph} . The resolution of the image in real space can be characterized by the distances $\Delta x/y$ between the x/y -coordinates, at which frequency/chemical shift spectra are recorded. This can

be described by

$$\Delta x/y = \frac{FOV_{x/y}}{N_{x/y}} = \frac{1}{N_{x/y}\Delta k_{x/y}} = \frac{1}{2k_{x/y,\max}} \quad (2.14)$$

where $N_{x/y}$ is the number of k -space points acquired in the $k_{x/y}$ -dimension. Therefore, the resolution of the image in real space can be improved by increasing the maximum values in k -space, at which free induction decays are acquired. Finally, the time domain in which the signal is acquired and the frequency domain of the frequency/chemical shift axis are related, so that the range of detectable frequencies $2f_{\max}$ and the distance between two data points Δf in the frequency/chemical shift axis are given by

$$2f_{\max} = \frac{1}{\Delta t} \quad (2.15)$$

$$\Delta f = \frac{2f_{\max}}{N_t} = \frac{1}{N_t\Delta t} = \frac{1}{\tau_{\text{acq}}} \quad (2.16)$$

where $1/\Delta t$ is the sampling rate of the free induction decay, τ_{acq} is the duration of the acquired free induction decay and N_t is the number of acquisition points of the free induction decay. Consequently, the range of detectable frequencies can be enlarged by increasing the sampling rate and the frequency/chemical shift resolution can be improved by increasing the duration of the signal acquisition.

2.2 Hyperpolarization

Hyperpolarization is a method which can be used to overcome the severe sensitivity limitations of conventional magnetic resonance spectroscopic imaging by significantly increasing NMR signal amplitudes. In recent years, four fundamentally different hyperpolarization techniques have become established: Spin exchange optical pumping (SEOP), signal amplification by reversible exchange in shield enables alignment transfer to heteronuclei (SABRE-SHEATH), direct parahydrogen induced polarization (PHIP), and dissolution dynamic nuclear polarization (DNP). A review on extracellular pH imaging [69] provides additional details with regard to each hyperpolarization method:

- SEOP can be used to polarize noble gases, e.g. ^{129}Xe . In a first step, circularly polarized laser light selectively excites a specific transition of an alkali metal vapor. Then, the polarization is transferred from the polarized electrons of the alkali metal atoms to the nuclei of the noble gas atoms by spin exchange collisions of the alkali metal and the noble gas atoms [9].
- SABRE transfers polarization from parahydrogen to the molecule of interest using an activated catalyst, e.g. a transient metal [3], most efficient in the variant of SABRE-SHEATH, where the magnetic field strength in the device is shielded by microtesla-metals [157, 159].

- PHIP transfers polarization from parahydrogen to the molecule of interest by chemical addition of hyperpolarized parahydrogen directly to a suitable unsaturated precursor molecule [18, 42, 84, 138].
- DNP transfers polarization from highly polarized electrons, provided by free stable radicals at liquid helium temperatures and at high magnetic fields, to the nucleus of the frozen molecule of interest via microwaves [10, 11], followed by dissolution to produce a room temperature solution of highly polarized spins.

On the one hand, both SABRE and PHIP do not require cryogenics and could thus offer a cheaper approach to hyperpolarization than DNP. On the other hand, SABRE needs a catalyst to bind to the target compound and PHIP requires a suitable unsaturated precursor molecule, restricting these methods to specific molecular classes, making dissolution-DNP the most general method to hyperpolarize nuclear spins.

The next Section 2.2.1 contains a theoretical description of the polarization level reached by the ^{13}C -DNP method, which will later on be used to hyperpolarize ^{13}C -fumaric acid, ^{13}C -pyruvic acid and ^{13}C -urea in Chapter 3, and ^{13}C -zymonic acid in Chapter 4.

2.2.1 Dissolution Dynamic Nuclear Polarization

In an external magnetic field \vec{B}_0 with the magnetic field strength B_0 , spin $1/2$ particles, such as electrons (e^-), protons (^1H) or carbon-13 (^{13}C) atoms, can be described by the Zeeman effect using superpositions of two eigenstates $|\pm\rangle$ with eigenenergies

$$E_{\pm} = \pm E_m = \pm \hbar \gamma B_0 / 2 \quad (2.17)$$

where \hbar is the reduced Planck constant and γ is the gyromagnetic ratio of the spin $1/2$ particles in $\text{rad s}^{-1} \text{T}^{-1}$ (Zeeman splitting). At thermal equilibrium, the populations n_{\pm} of these two energy eigenstates are governed by the Boltzmann distribution

$$\frac{n_{\pm}}{n_{-} + n_{+}} = \frac{e^{-E_{\pm}/E_t}}{e^{-E_{-}/E_t} + e^{-E_{+}/E_t}} \quad (2.18)$$

with the thermal energy $E_t = k_B T$, where k_B is the Boltzmann constant and T is the absolute temperature. Then, the ratio between the difference and the sum of these two populations characterizes the imbalance of the occupation of the two energy levels, the so-called thermal polarization

$$P_{\text{thermal}} = \frac{n_{-} - n_{+}}{n_{-} + n_{+}} = \tanh\left(\frac{E_m}{E_t}\right) = \tanh\left(\frac{\hbar \gamma B_0}{2k_B T}\right). \quad (2.19)$$

At a typical clinical magnetic field strength (3 T) and at room temperature (293 K), thermal ^{13}C polarization amounts to just 0.0003 % (= 3 parts per million). Even at a drastically reduced temperature of 1.2 K and a slightly increased magnetic field strength of 3.35 T (these are typical conditions of the commercially available Oxford Instruments HyperSense DNP Polarizer), thermal ^{13}C polarization only increases to approximately 0.07 %. However, due to the considerably higher gyromagnetic ratio of electrons compared to ^{13}C nuclear spins, thermal e^- polarization increases from 0.7 % to more than 95 % under the same conditions. Dissolution dynamic nuclear polarization (DNP, Fig. 2.2) exploits this fact, and in a first step transfers thermal polarization from free electrons to nuclear spins using microwave irradiation via the hyperfine interaction in a strong external magnetic field at very low temperatures [1]. In a second step, a heated and pressurized solvent such as water is used to dissolve the sample while preserving the hyperpolarization [11]. The drastically up-lifted polarization level P_{hyper} of a hyperpolarized sample can then conveniently be determined experimentally according to

$$P_{\text{hyper}} = \frac{S_{\text{hyper}}}{S_{\text{thermal}}} P_{\text{thermal}} \quad (2.20)$$

where S_{hyper} is the hyperpolarized signal, S_{thermal} is the thermal signal and P_{thermal} is the theoretical thermal polarization, all from the same sample. Here, the thermal signal can either be acquired under the same experimental conditions as the hyperpolarized signal, or it can be extrapolated to comparable conditions, taking into account parameters such as temperature, longitudinal relaxation, transverse relaxation, number of averages, magnetic field strength, flip angle and the type of sequence used to collect the data.

The magnitude M_0 of the NMR-detectable net magnetization \vec{M}_0 is then given as the product of the spin density ρ_0 , the elementary spin $1/2$ magnetic moment $\hbar\gamma/2$ and the spin polarization P as [63]

$$M_0 = \rho_0 \frac{\hbar\gamma}{2} P. \quad (2.21)$$

2.3 Cell death detection using hyperpolarized ^{13}C -fumarate *in vivo*

The endogenous molecule fumarate can be ^{13}C -labeled and hyperpolarized, and then be used to identify already small amounts of diffuse cellular necrosis *in vivo*.

Necrosis is a type of cell injury resulting in the premature death of cells in living tissue, leading to damaged cell membranes, which in turn become increasingly permeable for compounds to both enter and leave the cell. Necrosis is a valuable parameter since the level of tumor cell death after drug treatment is considered to be a good prognostic indicator for treatment outcome [167]. In addition, necrosis

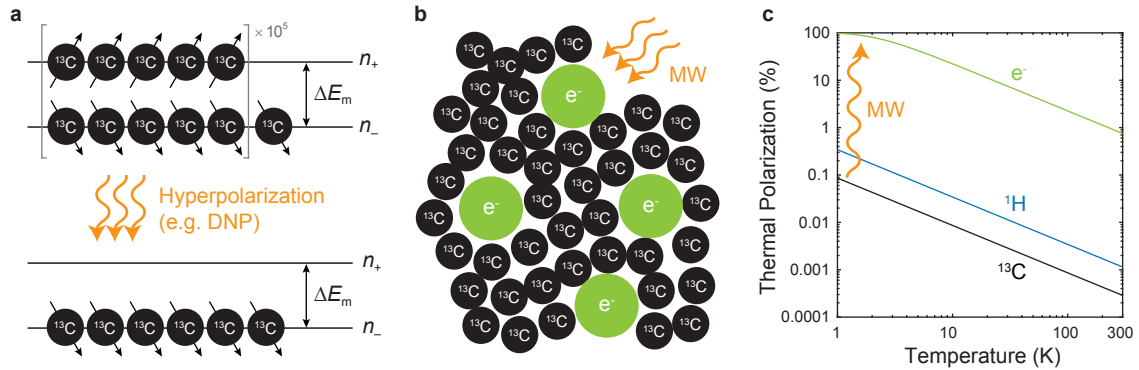
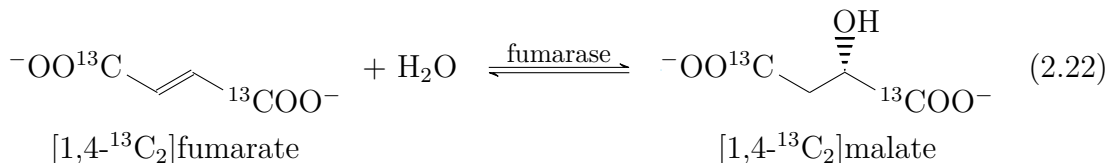


Figure 2.2: Hyperpolarization created by dissolution dynamic nuclear polarization (DNP). (a) Populations n_{\pm} of the two energy eigenstates of ^{13}C nuclei in an external magnetic field with an energy difference of $\Delta E_m = E_+ - E_-$ at thermal equilibrium (top) and in a hyperpolarized state (bottom). At room temperature (293 K) and at a typical clinical magnetic field strength (3 T), thermal ^{13}C polarization is only on the order of parts per million. With a hypothetical polarization level of 100% in the hyperpolarized state, all ^{13}C atoms would populate the lower energy state. (b) For the hyperpolarization of ^{13}C -labeled molecules using DNP, the molecules have to be mixed with a radical, e.g. the Trityl radical OX063, and brought into a glassy state, so that a microwave (MW) can transfer polarization from the unpaired valence electrons (e^-), provided by the radicals, to the ^{13}C atoms of interest. (c) At a magnetic field strength of 3.35 T, even at a temperature as low as 1.2 K (typical conditions of the commercially available Oxford Instruments Hypersense DNP Polarizer), thermal ^{13}C polarization only amounts to 0.07%, but due to the considerably higher gyromagnetic ratio of electrons compared to ^{13}C , thermal e^- polarization can reach more than 95%. Under optimal conditions, the hyperpolarization procedure can lift the polarization level of ^{13}C molecules to the one of electrons.

could play a role in the study of tumor development, since necrosis can lead to inflammation, and a persistent inflammatory response can in turn stimulate tumor development.

Fumarate is a tricarboxylic acid (TCA) cycle intermediate, which, catalyzed by the enzyme fumarate hydratase (i.e. fumarase), is hydrated to malate. If used for hyperpolarized experiments, fumarate and malate are ^{13}C -labeled at the carbon positions one and four.



In healthy tissue, fumarase only exists intracellularly, but both in the cytosol and in mitochondria. Under normal conditions, fumarate is only to a moderate degree transported into cells across the plasma membrane by dicarboxylic acid transporters and further across the mitochondrial membrane in exchange for malate, inorganic phosphate or aspartate. Thus, if hyperpolarized ^{13}C -fumarate is brought into the bloodstream by e.g. an intravenous injection, only a small amount of fumarate can get in contact with fumarase within the lifetime of the hyperpolarized signal due to the slow uptake in healthy tissue, consequently leading to a very small amount of detected ^{13}C -malate.

Because of the impaired cell membrane barrier, the situation is different in necrotic tissue. The enzyme fumarase can leave the cell, and then bind to the extracellular matrix, remain transiently because of poor tissue perfusion or get released into the blood stream. At the same time, fumarate can more easily enter the cell than before. Both of these changes lead to the fact that, due to the frequent contact of fumarate with fumarase both inside and outside the cell, and because besides water, fumarase does not require any co-substrates or co-enzymes to function, hyperpolarized and intravenously injected ^{13}C -fumarate is readily converted to ^{13}C -malate. This leads to an increased signal by the produced ^{13}C -malate and therefore reflects elevated levels of necrosis.

Marker of early tumor response to therapy. Gallagher et al. were the first to use hyperpolarized ^{13}C -fumarate to demonstrate that the production of malate from fumarate positively correlates with cellular necrosis using an EL-4 murine lymphoma tumor model treated with the chemotherapeutic agent etoposide [51]. The production of malate from injected fumarate thus represents an early marker of tumor therapy response both *in vitro* and *in vivo*. Subsequently, the same effect was demonstrated *in vivo* first by treating the same EL-4 murine lymphoma tumor model with the vascular disrupting agent (VDA) combretastatin-A4-phosphate (CA4P) [17], second by treating a subcutaneous human breast adenocarcinoma xenograft (MDA-MB-231) in mice with the chemotherapeutic drug doxorubicin [167] or sorafenib [109], and third by treating two subcutaneous human colorectal adenocarcinoma xenograft models (LoVo and HT29) in mice with the antiangiogenic anti-VEGF therapy drug bevacizumab [16].

Fumarase catalyzed conversion of hyperpolarized ^{13}C -fumarate to malate was also used to study the impact of ischemia reperfusion in the hind limb of mice on malate production by fumarase *in vivo* [73].

Early diagnosis of acute kidney injury. Finally, the fumarase catalyzed conversion of hyperpolarized ^{13}C -fumarate to malate was used to study acute kidney injury *in vivo*, a common medical problem for hospitalized patients associated with significant morbidity and mortality. First, the hyperpolarized quantification of necrosis allowed the early detection of acute tubular necrosis, by studying chemically induced nephropathy in mice using folic acid, and was able to differentiate it from glomerulonephritis, an acute inflammatory condition [30]. Second, hyperpolarized ^{13}C -fumarate was used to quantify and localize necrosis caused by renal injury in a unilateral ischemia and reperfusion model in rats [122].

On the one hand, using ^{13}C -fumarate for *in vivo* detection of necrosis faces several challenges [16, 17, 30, 51, 109, 122, 167]: Under *in vivo* conditions, it is very difficult or even unfeasible to coinject pyruvate and fumarate, since lactate, malate and pyruvate hydrate can only insufficiently be spectrally resolved. The spatial resolution of ^{13}C images is worse compared to diffusion-weighted MRI, which detects loss of cellularity, representing the end result of extensive cellular necrosis. After treatment with CA4P, fumarate exhibits an increased longitudinal relaxation rate, probably because of dipole-dipole interactions between ^{13}C nuclei, ^1H nuclei and paramagnetic deoxyhemoglobin and methemoglobin known to accumulate in regions of induced hemorrhage. Since malate is an asymmetric molecule (in contrast to the symmetric fumarate molecule), it exhibits two distinct NMR resonances leading to a lower SNR than fumarate. Due to the transport of fumarase out of the cell during necrosis, diffuse malate signal might also be detected outside necrotic regions.

On the other hand, using fumarate for detection of necrosis *in vivo* possesses unmatched advantages [16, 17, 30, 51, 109, 122, 167]: Diffusion-weighted MRI can detect loss of cellularity with higher resolution, but this only represents the end result of extensive cellular necrosis and there is currently no method to specifically image early necrosis *in vivo* other than ^{13}C -fumarate. Furthermore, fumarate is an endogenous molecule and thus non-toxic. As the equilibrium constant of fumarase favors the formation of malate, since fumarase is exclusively intracellular, and because transport of fumarate across the cell membrane is slow, the background signal in healthy tissue is minimal but the malate signal in necrotic areas shows detectable SNR. In addition, the method exhibits positive contrast (with more necrosis leading to a larger malate signal) and is therefore inherently more sensitive than a negative contrast experiment, which could suffer more from reduced tissue perfusion.

Altogether, hyperpolarized ^{13}C -fumarate represents a method to provide a spatially differentiated diagnosis of early acute kidney injury and represents a method to detect early treatment response to tumor therapy by measuring cellular necrosis *in vivo*, even in the absence of any change in tumor size or apparent diffusion coefficient.

2.4 pH determination *in vivo*

Pathologies characterized by abnormal metabolism can disturb pH regulatory mechanisms in the human body and lead to changes of the extracellular pH. Furthermore, the extracellular pH can be critical for disease progression and drug efficiency.

Therefore, a large number of different approaches and modalities have been suggested for non-invasive imaging of extracellular pH *in vivo*. A review on extracellular pH imaging [69] provides an extensive listing of molecules from a multitude of different classes of pH sensors. Positron emission tomography (PET) tracers show a pH-dependent tracer distribution [22, 45, 80] or insert into cell membranes in areas of acidic extracellular pH [38, 101, 160]. Optical pH imaging methods are pH-sensitive fluorescence ratio imaging microscopy (FRIM) or pH-dependent fluorescence lifetime imaging microscopy (FLIM) [8, 36, 156, 179]. Optoacoustic techniques also offer a pH-sensitive probe [27]. Proton MRI can be used to image extracellular pH by using exogenous molecules with pH-dependent relaxivities, affecting the longitudinal spin lattice relaxation constant (T_1) of water [99, 110, 178]. To determine the absolute pH in proton MRI, the *in vivo* molecule concentration can be determined by PET or by a subsequent or simultaneous injection of an additional, pH-insensitive substance [47, 133]. Several exogenous paramagnetic (PARACEST) and diamagnetic (DIACEST) complexes have been developed to image extracellular pH, based on pH-dependent chemical exchange saturation transfer (CEST) [4, 5, 25, 26, 72, 97, 98, 114, 149, 152, 176, 177]. Although suffering from the intrinsically low sensitivity of conventional NMR for the detection of molecules at low concentration, sensors with pH-dependent changes in chemical shift of ^1H , ^{19}F and ^{31}P were used to estimate the extracellular pH *in vivo* [54, 70, 126, 131, 151]. Furthermore, several biocompatible nanoparticles, nanogels and quantum dots, based on a variety of mechanisms, have been proposed for pH imaging [23, 93, 125, 164, 172, 175].

However, to this day, none of the methods to spatially image extracellular pH is available in the clinic, making it necessary to continue the search for novel pH imaging probes and modalities.

Section 2.4.1 introduces chemical exchange as one of the basic concepts behind pH sensor molecules and illustrates the difference between slow and fast chemical exchange. Then, Section 2.4.2 describes the determination of pH using phosphorus spectroscopy, currently considered the gold standard to non-invasively determine pH *in vivo*, which can be used to measure both intra- and extracellular pH. Finally, Section 2.4.3 introduces the method of hyperpolarized pH imaging and specifically describes ^{13}C -bicarbonate and ^{13}C -zymonic acid in more detail, the only two molecules that have currently been used for the acquisition of hyperpolarized MRI of pH in preclinical studies.

2.4.1 Chemical exchange and pH-dependent NMR spectra

If a molecule contains one or more NMR active nuclei with chemical shifts depending on the protonation state of the molecule, this molecule could be used as an NMR-based pH sensor. The center of the pH sensitivity range of the molecule is determined by the logarithmic acid dissociation constant pK_a , derived from the equilibrium constant describing the chemical equilibrium between the protonated (acid) and deprotonated (base) form of the pH-sensitive molecule. The nature of the pH-dependent NMR spectra depends on the type of chemical exchange between the protonated and deprotonated form of the molecule.

First, the protonated and deprotonated form of the pH-sensitive molecule can be in intermediate exchange, meaning that the exchange rate k between the two forms of the molecule is of the same order as the difference $\Delta\nu$ (in Hz) between the NMR resonance frequencies of the two forms of the molecule, $k \approx \Delta\nu$. In this case, a broad linewidth is characteristic for the resulting resonance signal, which is unfavorable for an effective pH determination.

Second, the protonated and deprotonated form of the pH-sensitive molecule can be in slow exchange, meaning that the exchange rate between the two forms of the molecule is much smaller than the difference between the NMR resonance frequencies of the two forms of the molecule, $k \ll \Delta\nu$. In this case, two distinct chemical shifts of the protonated and deprotonated form of the molecule (with chemical shifts δ_{\min} and δ_{\max} or vice versa) are observed, with the signal intensities I_{HA} and I_{A^-} proportional to the concentrations $[\text{HA}]$ of the protonated and $[\text{A}^-]$ of the deprotonated form of the molecule (Fig. 2.3a). The pH can then be calculated from the ratio of the observed signal intensities by

$$\text{pH} = pK_a + \log_{10} \left(\frac{[\text{A}^-]}{[\text{HA}]} \right) = pK_a + \log_{10} \left(\frac{I_{\text{A}^-}}{I_{\text{HA}}} \right). \quad (2.23)$$

An example of this type of pH sensor molecule with slow chemical exchange is bicarbonate, described in more detail in Section 2.4.3.1.

Third, the protonated and deprotonated form of the pH-sensitive molecule can be in fast exchange, meaning that the exchange rate between the two forms is much greater than the difference between the NMR resonance frequencies of the two forms of the molecule, $k \gg \Delta\nu$. In this case, the NMR spectrum consists of a single peak and its observed chemical shift δ is the mean of the chemical shifts of the protonated and deprotonated form of the molecule (with chemical shifts δ_{\min} and δ_{\max} or vice versa), weighted by the concentrations $[\text{HA}]$ of the protonated and $[\text{A}^-]$ of the deprotonated form of the molecule (Fig. 2.3b). The pH can then be calculated from the observed chemical shift δ by

$$\text{pH} = pK_a + \log_{10} \left(\frac{[\text{A}^-]}{[\text{HA}]} \right) = pK_a \pm \log_{10} \left(\frac{\delta - \delta_{\min}}{\delta_{\max} - \delta} \right) \quad (2.24)$$

with a positive sign if $\delta_{\min} = \delta_{\text{HA}}$ and $\delta_{\max} = \delta_{\text{A}^-}$, and a negative sign if $\delta_{\min} = \delta_{\text{A}^-}$

and $\delta_{\max} = \delta_{\text{HA}}$. A more detailed derivation of this equation is given in Section 2.4.3.2 for the fast chemical exchange molecule zymonic acid.

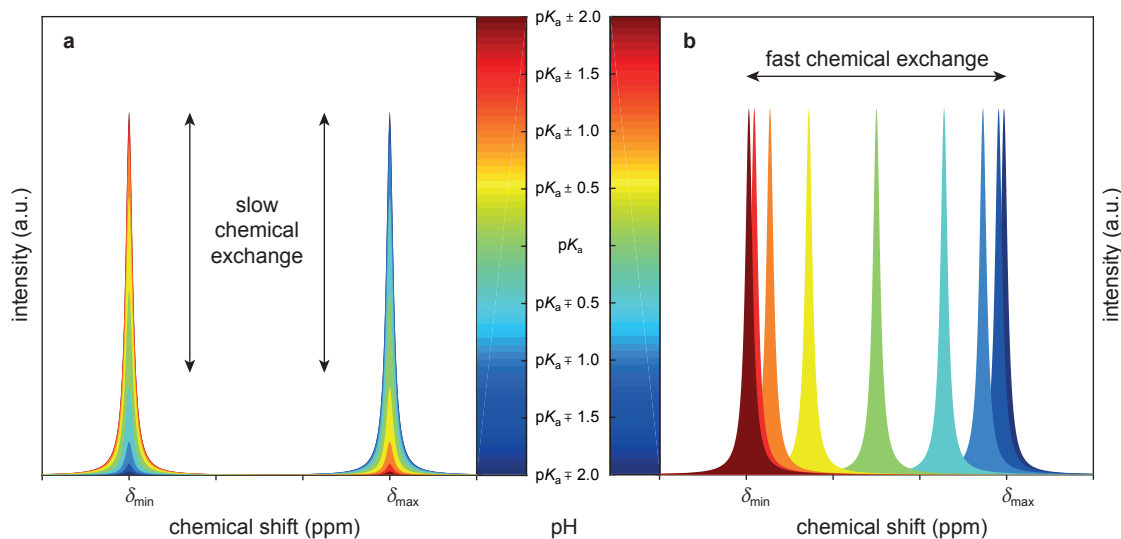


Figure 2.3: Slow and fast chemical exchange leading to pH-dependent, either signal intensity modulated or chemical shift modulated NMR spectra. (a) Slow chemical exchange between the protonated (acid) and deprotonated (base) form of a molecule leads to pH-dependent signal intensities of the two forms of the molecule, with the same signal intensity of the two forms at a pH equal to the logarithmic acid dissociation constant $\text{p}K_a$. (b) Fast chemical exchange between the protonated (acid) and deprotonated (base) form of a molecule leads to a pH-dependent chemical shift of the molecule, with the biggest change in chemical shift at a pH equal to the logarithmic acid dissociation constant $\text{p}K_a$. In both cases, δ_{\min} and δ_{\max} are the chemical shifts of the two different, either protonated or deprotonated forms of the molecule.

2.4.2 Phosphorus pH spectroscopy *in vivo*

Due to its comparatively easy implementation, its ability to measure both intra- and extracellular pH, and its long history of successful use in research, phosphorus-31 (^{31}P) spectroscopy can currently be considered the quasi “gold standard” for pre-clinical non-invasive determination of pH *in vivo*. Its widespread usage is documented in a number of review papers [26, 55–57, 65, 150].

Several advantageous properties of the ^{31}P nucleus make phosphorus spectroscopy possible in a variety of biological systems. Because of its NMR active spin $1/2$, its presence at 100% natural abundance, and its gyromagnetic ratio of $\sim 17\text{ MHz T}^{-1}$ resulting in a sensitivity of $\sim 6.6\%$ compared to ^1H [147], plus a short enough longitudinal relaxation rate T_1 so that efficient signal averaging is possible, ^{31}P spectra can be acquired within several minutes. A large number of endogenous molecules contain phosphorus atoms, but because a typical ^{31}P spectrum spans approximately

40 ppm and in large parts exhibits a wide enough peak separation (Fig. 2.4c), the positions of specific peaks of interest can often be successfully analyzed.

Most prominently, the chemical shift of the endogenous molecule inorganic phosphate (P_i) can be used to measure intracellular pH both *in vitro* and *in vivo* [115], and the exogenous compound 3-aminopropylphosphonate (3-APP) allows the spectroscopic determination of extracellular pH *in vivo* [54].

Although (localized) ^{31}P spectra can be acquired within a reasonable amount of time, magnetic resonance spectroscopic imaging (MRSI) for the determination of extracellular pH *in vivo* using ^{31}P is impractical due to its low sensitivity and accompanying requirements on magnetic field homogeneity and minimal movement to achieve a sufficient signal to noise ratio (SNR). In addition, the exogenous compound 3-APP does not cross the blood-brain barrier [119] and is not safe for use *in human* [100].

The usual convention for *in vivo* phosphorus spectra is to use phosphocreatine (PCr) as a ^{31}P chemical shift reference set to $\delta_{\text{PCr}} = 0$ ppm. In tissues where PCr cannot be observed, α -adenoside triphosphate (α -ATP) can alternatively be used as ^{31}P chemical shift reference. This is possible, because at physiological pH values above pH 6.1, both PCr with a logarithmic acid dissociation constant of $\text{p}K_a(\text{PCr}) = 4.6$ and α -ATP with a logarithmic acid dissociation constant of $\text{p}K_a(\alpha\text{-ATP}) = 4.85$ are fully deprotonated, so that their chemical shifts do not depend on pH [100].

2.4.2.1 Intracellular pH (pH_i) measurements using P_i

Moon et al. were the first to use the chemical shift of inorganic phosphate (P_i) to estimate the intracellular pH of intact red cells in whole blood [115]. Griffiths et al. then pioneered the measurement of tumor intracellular pH *in vivo* [62]. The claim, that the pH reported by inorganic phosphate is usually indeed strongly weighted towards the intracellular pH, can experimentally be confirmed by identifying the source of the P_i signal through determination of both the relative volumes of the relevant compartments (such as intra- and extracellular) in the tissue of interest and of the concentrations of inorganic phosphate in these compartments [2, 26]. Using a form of the Henderson-Hasselbalch equation

$$\text{pH}_i(\delta) = \text{p}K_a + \log_{10} \left(\frac{\delta - \delta_{\min}}{\delta_{\max} - \delta} \right), \quad (2.25)$$

the intracellular pH (pH_i) can be expressed as a function of the observed chemical shift δ of inorganic phosphate, where $\text{p}K_a$ is the logarithmic acid dissociation constant of inorganic phosphate, δ_{\min} is the limiting minimum (acid) chemical shift of inorganic phosphate and δ_{\max} is the limiting maximum (base) chemical shift of inorganic phosphate [54]. Thus, depending on whether the chemical shifts in the ^{31}P spectra were referenced to either phosphocreatine (PCr) or to α -adenoside

triphosphate (α -ATP), the intracellular pH can be calculated from the chemical shift of inorganic phosphate with the appropriate numerical values, summarized in Table 2.1.

Table 2.1: Parameters to calculate pH values from ^{31}P chemical shifts of P_i and 3-APP. Values were obtained by Ojugo et al. by fitting the appropriate Henderson-Hasselbalch equations 2.25 or 2.26 to NMR titration curves consisting of chemical shifts of 19 different pH values between pH 5.0 and pH 9.0 with ionic strength I and temperature ϑ closely mimicking *in vivo* conditions [126]. P_i , inorganic phosphate; 3-APP, 3-aminopropylphosphonate; PCr, phosphocreatine; α -ATP, α -adenoside triphosphate; $\text{p}K_a$, logarithmic acid dissociation constant; δ_{\min} , limiting minimum chemical shift; δ_{\max} , limiting maximum chemical shift.

sensor molecule	chemical shift reference	$\text{p}K_a$	δ_{\min}/ppm	δ_{\max}/ppm	titration conditions	reference
P_i	PCr	6.68 ± 0.02	3.31	5.72	$I = 0.25 \text{ M}$ $\vartheta = 37^\circ \text{C}$	[126]
P_i	α -ATP	6.75 ± 0.03	10.89	13.28	$I = 0.25 \text{ M}$ $\vartheta = 37^\circ \text{C}$	[126]
3-APP	PCr	6.85 ± 0.03	23.53	27.01	$I = 0.25 \text{ M}$ $\vartheta = 37^\circ \text{C}$	[126]
3-APP	α -ATP	6.79 ± 0.04	31.07	34.62	$I = 0.25 \text{ M}$ $\vartheta = 37^\circ \text{C}$	[126]

2.4.2.2 Extracellular pH (pH_e) measurements using 3-aminopropylphosphonate (3-APP)

Gillies et al. introduced the exogenous compound 3-aminopropylphosphonate (3-APP, Fig. 2.4a) to measure extracellular pH, initially demonstrated in two types of tumor cells both *in vitro* and *in vivo*. 3-APP is non-toxic and its chemical shift is clearly separable from ^{31}P signals of endogenous molecules (Fig. 2.4c) and is not significantly affected by temperature or ionic strength. At the same time, 3-APP possesses a $\text{p}K_a$ in the physiological pH range, it can be injected intraperitoneally (i.p.) and it is neither internalized nor metabolized [54].

Analogously to the evaluation of ^{31}P spectra for the determination of the intracellular pH from the chemical shift of inorganic phosphate, the extracellular pH (pH_e) can be calculated as a function of the observed chemical shift δ of 3-APP using a form of the Henderson-Hasselbalch equation

$$\text{pH}_e(\delta) = \text{p}K_a - \log_{10} \left(\frac{\delta - \delta_{\min}}{\delta_{\max} - \delta} \right) \quad (2.26)$$

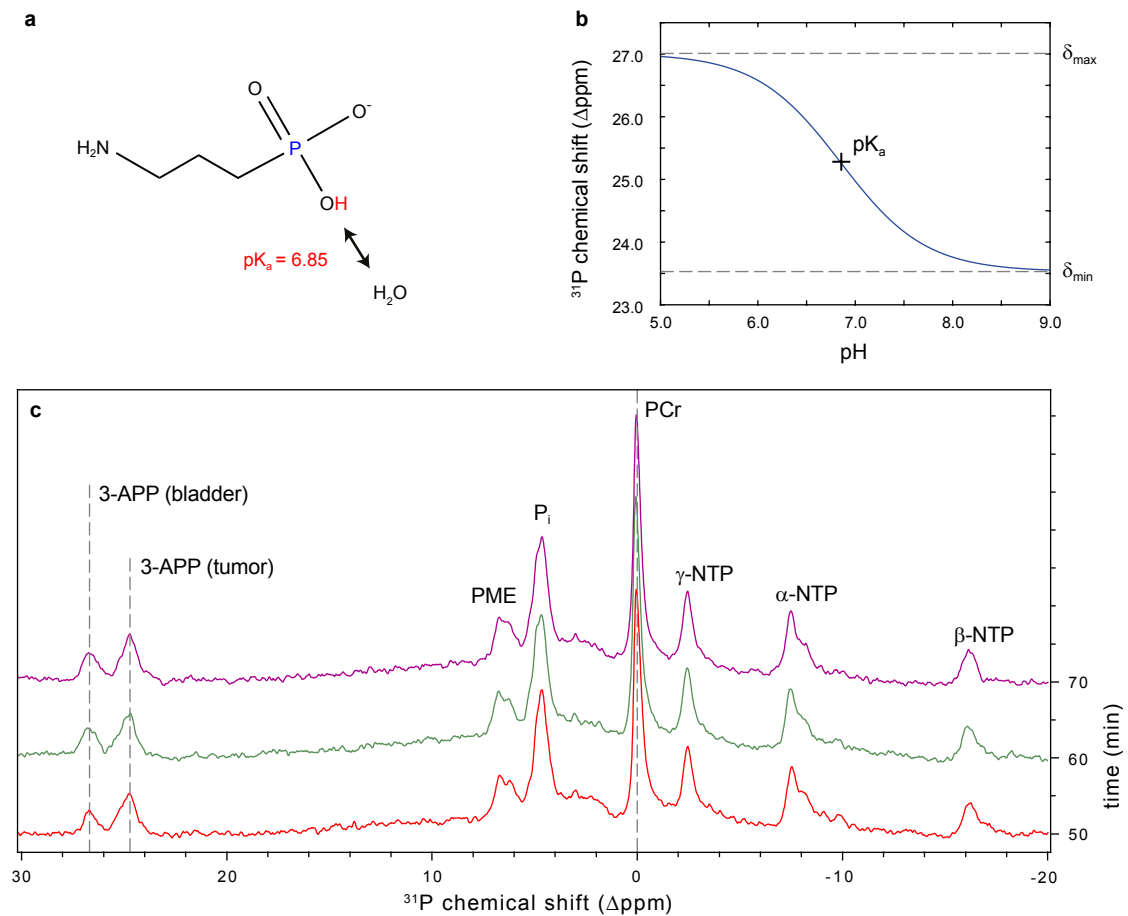


Figure 2.4: Determination of extracellular pH using 3-APP based on ^{31}P spectroscopy. (a) Structure of 3-aminopropylphosphonate (3-APP) with the relevant pK_a of the exchangeable proton (red) and the NMR active ^{31}P nucleus (blue). (b) Chemical shift of 3-APP with the ^{31}P spectra referenced to phosphocreatine (PCr) set to 0 ppm as a function of pH, illustrating the fit parameters from [126] with $pK_a = 6.85$, limiting acid chemical shift $\delta_{\max} = 27.01$ ppm and limiting base chemical shift $\delta_{\min} = 23.53$ ppm of 3-APP. (c) Representative ^{31}P spectra acquired 50, 60 and 70 min after i.p. injection of 3 mL of 64 mg mL^{-1} 3-APP into a rat with a ^{31}P transmit receive loop coil placed directly above the subcutaneous MAT B III tumor. The 3-APP signal with the chemical shift corresponding to a pH of 7.2 stems from the extracellular pH in the tumor, whereas the 3-APP signal with the chemical shift corresponding to a pH of 6.0 comes from abundant 3-APP in the nearby bladder. Further substances visible in the spectrum are phosphomonoesters (PME), inorganic phosphate (P_i), α -nucleoside triphosphate (α -NTP), β -nucleoside triphosphate (β -NTP) and γ -nucleoside triphosphate (γ -NTP). Peak assignments were done according to [59], taking into account that the NTP signals in tumors originate from all four nucleotide bases (ATP, CTP, GTP, UTP), in contrast to normal tissue, where the NTP signal stems predominantly from adenosine triphosphate (ATP) only [119].

with the appropriate numerical values from Table 2.1, where pK_a is the logarithmic acid dissociation constant of 3-APP, δ_{\min} is the limiting minimum (base) chemical shift of 3-APP, δ_{\max} is the limiting maximum (acid) chemical shift of 3-APP [54].

Note that the sign in equation 2.26 in front of the logarithm is changed compared to equation 2.25, reflecting the fact that phosphonates (i.e. 3-APP) shift to lower chemical shifts at higher pH values, compared with phosphates (i.e. P_i), which shift to higher chemical shifts at higher pH values [54, 126]. From Fig. 2.4b it can be seen that 3-APP exhibits a sensitivity of 1.7 ppm per pH around its pK_a [126].

Representative ^{31}P spectra of a subcutaneous MAT B III tumor acquired in a rat after i.p. injection of 3-APP are shown in Fig. 2.4c. The 3-APP peak corresponding to a pH of 7.2 stems from the extracellular pH in the tumor, the 3-APP peak corresponding to a pH of 6.0 comes from abundant 3-APP in the nearby bladder. In addition, endogenous ^{31}P signals from phosphomonoesters (PME), inorganic phosphate (P_i , which could be used to determine the intracellular pH), phosphocreatine (PCr, which was used as chemical shift reference and set to 0 ppm), α -nucleoside triphosphate (α -NTP), β -nucleoside triphosphate (β -NTP) and γ -nucleoside triphosphate (γ -NTP) are visible in these spectra.

2.4.2.3 Techniques for the analysis of spectra containing pH information

In the analysis of phosphorus spectra, several postprocessing techniques can be used to either correct for spectral distortions or to extract characteristic information from the peak profile of the pH-sensitive resonances. These include spectral intensity adjustments to correct for skewed spectra introduced by the nonlinear relationship (equations 2.25 and 2.26) between the pH scale and the ppm scale [60] and the extraction of several statistical parameters describing the line shape of the pH profile characterizing the underlying pH distribution [100].

Once the ppm scale has been converted to the pH scale using the appropriate Henderson-Hasselbalch equation (equation 2.25 or 2.26), the intensity of the pH distribution profile has to be divided by the derivative of that equation to correct for the non-linear relationship between the ppm scale and the pH scale [2]. The corrected intensity I_{corr} can therefore be expressed as

$$I_{\text{corr}}(\text{pH}) \propto I(\delta) \left| \frac{d\text{pH}(\delta)}{d\delta} \right|^{-1} \propto I(\delta) \frac{(\delta_{\max} - \delta)(\delta - \delta_{\min})}{(\delta_{\max} - \delta_{\min})} \quad (2.27)$$

with the same variables and parameters as used in equation 2.25 or 2.26. To simplify the expression, the proportionality sign drops an irrelevant factor of $\ln(10)$ stemming from the derivative of the decadic logarithm, since it is common practice to display the intensity scale in arbitrary units [2, 60].

For a narrow pH signal at precisely the pK_a , this intensity correction does not result in a change in the determined pH, but the broader a pH distribution or the

further away the center of a pH distribution from the pK_a , the larger the intensity correction factor and thus the larger the change in the determined pH distribution. Although this correction is relatively small compared to the uncertainties of the absolute value of the pH due to uncertainties in the values of pK_a , δ_{\min} and δ_{\max} (e.g. due to different chemical environments depending on the cellular surroundings), it can be of importance when looking at relative changes in well reproducible experimental settings. The method is only valid, if the dominant effect on the line shape is the underlying pH distribution, and not other factors, such as magnetic field inhomogeneities or line broadening caused by filtering during postprocessing of the acquired data.

After applying the spectral intensity correction, the calculation of one or several statistical parameters of the determined tumor pH profile, such as weighted mean, weighted median, modes, skewness (asymmetry), kurtosis (peakedness) and entropy (smoothness), as well as relative sizes of the tissue volumes under investigation, estimated by integration or fitting the pH profile to multiple modes, might be a possibility to extract useful information from more complicated pH distribution profiles [100], such as a correlation between pH heterogeneity and the extent of tumor necrosis in tissue [29].

2.4.3 Hyperpolarized pH imaging *in vivo*

Hyperpolarization is an effective method to significantly increase NMR signal amplitudes to overcome sensitivity limitations of conventional magnetic resonance spectroscopic imaging, as described in Section 2.2.

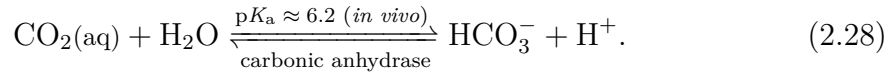
In vitro, a number of hyperpolarizable molecules from different molecular classes have been proposed to measure pH within the physiologically and pathologically relevant pH range of pH 5–8. The successful MR acquisition of pH images of buffered phantoms was demonstrated using hyperpolarized $[2-^{13}\text{C}]$ diethylmalonic acid, belonging to the group of ^{13}C -labeled dicarboxylic acids [86], using ACES, a member of the Good's buffers family [44], and using ^{15}N -pyridine, as a representative of the group of ^{15}N -labeled pyridine derivatives [74]. Furthermore, ^{15}N -imidazole [148] as well as the two chelators DOTP [75] and a modified cryptophane cage [139], loaded with hyperpolarized ^{89}Y and hyperpolarized ^{129}Xe , respectively, have been shown to be pH-sensitive within the physiologically and pathologically relevant pH range.

In vivo, ^{13}C -bicarbonate and $[1,5-^{13}\text{C}_2]$ zymonic acid are the only molecules, which have currently been both hyperpolarized and used for MRI of pH in preclinical studies. The next two sections will first describe pH imaging using hyperpolarized ^{13}C -bicarbonate and second introduce the novel hyperpolarized probe $[1,5-^{13}\text{C}_2]$ zymonic acid for pH imaging. Later on, zymonic acid will extensively be characterized and applied *in vivo* in Chapter 4.

2.4.3.1 pH imaging using ^{13}C -bicarbonate

^{13}C -Bicarbonate is the only molecule, which has previously successfully been both hyperpolarized and used for pH imaging *in vivo*.

While intracellular pH buffering is dominated by inorganic phosphate (P_i) and proteins [49], bicarbonate (HCO_3^-) is the main extracellular buffering capacity in mammalian tissue [50], with a plasma bicarbonate concentration in humans of ~ 24 mM. The chemical equilibrium between bicarbonate and carbon dioxide is used to keep the extracellular acid-base balance tightly controlled between pH 7.35–7.45. To compensate for too acidic pH values in the blood, bicarbonate binds with excess protons forming carbonic acid, which in aqueous conditions immediately dissociates into water and carbon dioxide according to



Carbon dioxide is then removed from the system by exhalation so that the pH can return to physiological values. In the opposite case of too basic pH values in the blood, the exact reverse mechanism is used to decrease the pH to physiological values. Since the concentration of water is commonly taken as constant, the *in vivo* equilibrium concentrations of this reaction

$$K_a = \frac{[\text{HCO}_3^-][\text{H}^+]}{[\text{CO}_2]} \quad (2.29)$$

are characterized by the logarithmic acid dissociation constant [46, 145]

$$\text{p}K_a = -\log_{10}(K_a/\text{mol}) \approx 6.2. \quad (2.30)$$

Steady state equilibrium concentrations can quickly be reached if the enzyme carbonic anhydrase is present, which increases the reaction rate to up to 10^6 reactions per second. Measuring the equilibrium concentrations of bicarbonate and carbon dioxide then allows the determination of the associated pH according to the Henderson-Hasselbalch equation

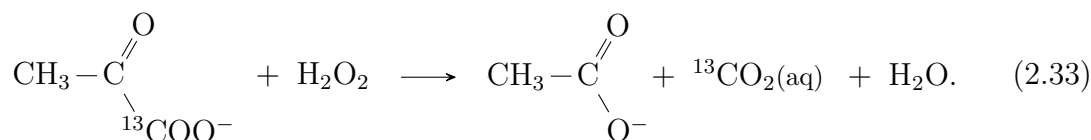
$$\text{pH} = \text{p}K_a + \log_{10} \left(\frac{[\text{HCO}_3^-]}{[\text{CO}_2]} \right). \quad (2.31)$$

Despite the high endogenous concentration of bicarbonate, the low ^{13}C natural abundance of only 1.1% and the low sensitivity of the ^{13}C nuclear spins prevent determining *in vivo* pH values from endogenous bicarbonate directly. However, exogenous, ^{13}C -labeled, hyperpolarized and intravenously injected bicarbonate can be used to measure the equilibrium concentrations of bicarbonate and carbon dioxide to perform pH imaging *in vivo*. The signal intensities of the NMR resonances of bicarbonate $I_{\text{H}^{13}\text{CO}_3^-}$ and carbon dioxide $I_{^{13}\text{CO}_2}$, whose chemical exchange rate is slow on the NMR time scale, are used to calculate the necessary ratio of the equilibrium

concentrations to determine the pH, resulting in

$$\text{pH} = \text{p}K_a + \log_{10} \left(\frac{I_{\text{H}^{13}\text{CO}_3^-}}{I_{^{13}\text{CO}_2}} \right). \quad (2.32)$$

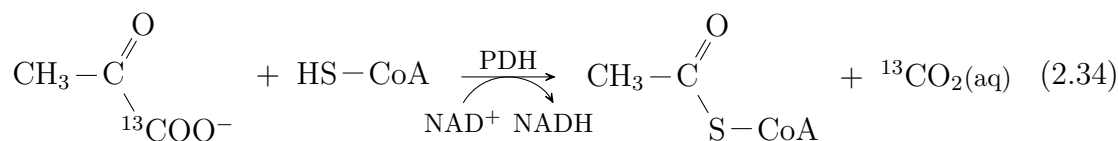
Extracellular pH. Gallagher et al. were the first to use hyperpolarized cesium bicarbonate to measure the average tumor interstitial pH/extracellular tissue pH in a mouse tumor model of subcutaneously implanted EL-4 lymphoma cells *in vivo* [49, 50]. The same method with optimized parameters was used to determine the extracellular pH in induced acute subcutaneous sterile inflammation in rats *in vivo* [143, 144]. Ghosh et al. avoided the usage of toxic cesium for extracellular pH measurements and demonstrated the *in vitro* carbonic anhydrase catalyzed production of hyperpolarized bicarbonate from carbon dioxide by decarboxylation of hyperpolarized pyruvic acid using hydrogen peroxide (H_2O_2) [53] according to



This reaction can also be performed with other α -keto carboxylic acids, such as α -ketoisocaproate [53].

In a similar approach, hyperpolarized ^{13}C -labeled bicarbonate was formed from hyperpolarized 1,2-glycerol- ^{13}C -carbonate in the presence of sodium hydroxide and heat after dissolution, and was then used to measure the extracellular pH in a transgenic adenocarcinoma of the mouse prostate murine model *in vivo* [85].

Intracellular pH. Schroeder et al. injected hyperpolarized pyruvic acid intravenously and then observed the *in vivo* formation of hyperpolarized carbon dioxide and bicarbonate in the healthy rat heart [145]. In this reaction, pyruvate is transported from the extracellular space into the cytosol by monocarboxylate transporters (MCT) before pyruvate dehydrogenase (PDH) inside the mitochondria converts pyruvate into acetyl-CoA and hyperpolarized carbon dioxide according to



where NAD^+ is the oxidized form of nicotinamide adenine dinucleotide, NADH is the reduced form of nicotinamide adenine dinucleotide, and $\text{HS}-\text{CoA}$ is the coenzyme A. The still hyperpolarized carbon dioxide is then assumed to rapidly diffuse into the cytosol and equilibrate with bicarbonate by the help of the enzyme carbonic anhydrase (CA). In these experiments, the pH determined from the equilibrium between bicarbonate and carbon dioxide correlated with the pH measured from ^{31}P inorganic phosphate (P_i) measurements and is thus considered to represent the intracellular pH of the studied cardiac myocytes.

On the one hand, using bicarbonate for *in vivo* pH imaging possesses several advantages [49, 50, 53, 143, 145]: Bicarbonate is an endogenous molecule, it can be infused into patients at relatively high concentrations without toxic effects and it is already licensed for 1 M injections. In addition, ratiometric methods are independent of probe concentration, the pK_a of the equilibrium makes bicarbonate sensitive in the pathological pH range of interest and the chemical shift difference of ~ 36 ppm between bicarbonate and carbon dioxide is large enough to be discriminated even at low magnetic field strengths. Furthermore, the inside of erythrocytes and the surface of tumor cells usually exhibit high carbonic anhydrase activity so that the steady state of the equilibrium between bicarbonate and carbon dioxide is quickly reached.

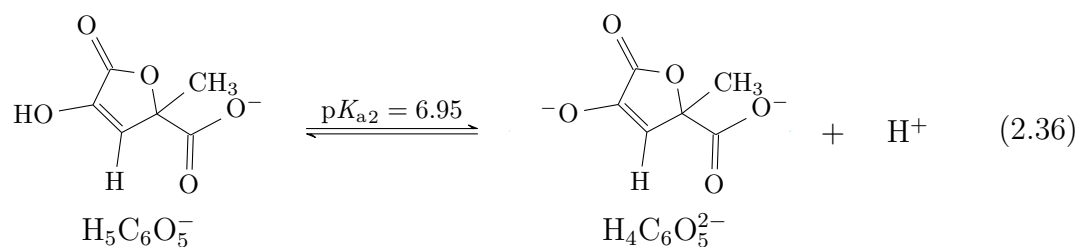
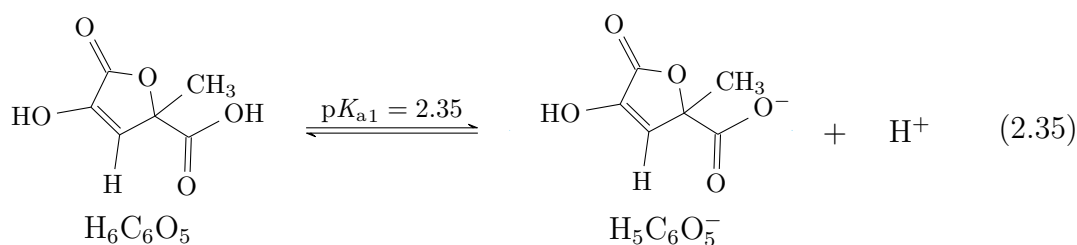
On the other hand, using bicarbonate for *in vivo* pH imaging also faces a number of challenges [49, 50, 53, 143, 145]: Cesium, which is mostly used in the direct hyperpolarization of bicarbonate, is toxic and has to be removed before injection using an ion-exchange column reducing the available polarization due to the additionally required time. Although hydrogen peroxide is relatively safe *in vivo*, excessive levels of unreacted hydrogen peroxide also have to be removed from the system before injection, requiring an additional step before the hyperpolarized compound can be used. In some of the reported experiments, an increased blood pH and a reduced breathing rate directly after administration of bicarbonate was observed, hinting to an induced acute metabolic alkalosis by the injection of the large amount of bicarbonate. Additionally, depending on which method is used and which tissue is studied, a sufficiently high pyruvate dehydrogenase activity is needed and a sufficient amount of carbonic anhydrase is necessary to guarantee that the ratio between bicarbonate and carbon dioxide is indeed coming from the same cellular compartment and equivalent to the concentration ratios of the molecule pools *in vivo*; e.g. in cardiac myocytes, carbonic anhydrase activity is only modest and could even be further inhibited by low intracellular pH and pharmacological membrane transport inhibitors. Furthermore, bicarbonate measurements suffer from low signal to noise: both sodium bicarbonate (~ 1 M) and cesium bicarbonate (~ 4 – 6 M) are relatively insoluble, polarization is lost during dissolution by outgassing of carbon dioxide, both substances have a short *in vivo* polarization lifetime of $T_1 \approx 10$ s at 3 T, and due to the ratio of bicarbonate to carbon dioxide of ~ 10 :1 at physiological pH values, the very low carbon dioxide signal intensity must be accurately quantified in order to achieve a reliable pH measurement result. At last, as can be seen from the fact that in two different scenarios, the equilibrium between bicarbonate and carbon dioxide can either report on the extracellular or the intracellular pH, it is not clear to which degree the pH reported by hyperpolarized bicarbonate is in general weighted towards the extracellular or intracellular pH *in vivo*.

2.4.3.2 pH imaging using hyperpolarized ^{13}C -zymonic acid

The molecule zymonic acid, which will be introduced in Chapter 4 as a novel ^{13}C -labeled and hyperpolarized biosensor for *in vivo* pH imaging, was first discovered in 1899, but since then has rarely been mentioned in the literature.

Zymonic acid, with its IUPAC name 4-hydroxy-2-methyl-5-oxo-2,5-dihydrofuran-2-carboxylic acid, is sometimes also referred to as α -keto- γ -valerolactone- γ -carboxylic acid, 2-hydroxy-4-methyl-4-carboxy-buten-(2)-olid-(4,1), 4-hydroxy-2-keto-4-methylglutaric acid lactone or α -hydroxy- γ - $\Delta^{\alpha,\beta}$ -butenolide- γ -carboxylic acid.

Wolff [168, 169] and de Jong [76, 77] were the first to describe parapyrvic acid and zymonic acid as condensation products of pyruvic acid under the influence of HCl. Zymonic acid received its trivial name from the Greek word “zyme” meaning “leaven” or “yeast” since it had mistakenly been identified as a metabolite produced by yeasts [155]. Only later it was realized that zymonic acid can occur as a chemical impurity in pyruvic acid [87, 105] and that this explained the observation of zymonic acid among the metabolic products of yeasts [155]. The two pK_a values of zymonic acid have been determined to be 2.35 for the carboxy group and 6.95 for the enolic hydroxy group [87, 112]:

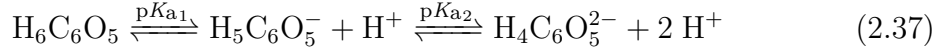


Evidence suggests that zymonic acid’s ring structure does not break up during acid-base titrations [112, 155, 169]. Zymonic acid’s melting point has been determined to be 115–116 °C [21, 68], its paper chromatographic retention factor [130, 162], UV and IR data were recorded [13, 21, 105]. There has long been confusion about whether zymonic acid is present as an enol or ketone, but a general study about the keto-enol-equilibrium of cyclic α -diketones [146] and proton NMR data made clear that zymonic acid is present as an enol [13, 105]. Temporarily, it was erroneously assumed that zymonic acid inhibits the tricarboxylic acid cycle [112], but it was later realized that not zymonic acid but rather parapyrvic acid was inhibiting α -ketoglutaric oxidase [113], although it is very unlikely that this inhibitory effect will occur *in vivo* [111]. Recently, fluoro analogues of zymonic acid have been produced [153] and zymonic acid has been discovered among the products of multiphase photolysis of pyruvic acid during atmospheric studies [129, 134, 135].

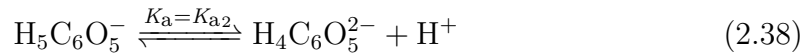
A single, pH-dependent chemical shift of a pH sensor molecule can be observed, if

this sensor molecule contains an NMR active nucleus, if its acid and conjugate base concentrations are at equilibrium and if the acid and conjugate base forms of the molecule are in fast chemical exchange (see Section 2.4.1 and [2]).

Zymonic acid is such a pH sensor molecule, with two dissociable protons with logarithmic acid dissociation constants $pK_{a1} = 2.35$ and $pK_{a2} = 6.90$:



In the pathologically and physiologically interesting pH range of pH 5–8, there is rapid hydrogen exchange between the relevant acid ($\text{H}_5\text{C}_6\text{O}_5^-$) and conjugate base ($\text{H}_4\text{C}_6\text{O}_5^{2-}$) form: in this pH range, the carboxy group is fully deprotonated due to its low pK_{a1} and the acid base equilibrium concentrations are determined by the second logarithmic acid dissociation constant pK_{a2} . Thus, the relevant equilibrium reaction (equation 2.38) and the relevant equilibrium concentrations (equation 2.39) of this chemical equilibrium can be described by



and

$$K_a = \frac{[\text{H}^+][\text{H}_4\text{C}_6\text{O}_5^{2-}]}{[\text{H}_5\text{C}_6\text{O}_5^-]} \quad (2.39)$$

Taking the decadic logarithm and using the identities $\text{pH} = -\log_{10}([\text{H}^+]/\text{mol})$ as well as $\text{p}K_a = -\log_{10}(K_a/\text{mol})$, this results in the well known Henderson-Hasselbalch equation

$$\text{pH} = \text{p}K_a + \log_{10} \left(\frac{[\text{H}_4\text{C}_6\text{O}_5^{2-}]}{[\text{H}_5\text{C}_6\text{O}_5^-]} \right) \quad (2.40)$$

$$= \text{p}K_a + \log_{10} \left(\frac{\chi_{\text{base}}}{\chi_{\text{acid}}} \right) \quad (2.41)$$

with the introduction of the concept of mole fractions

$$\chi_{\text{acid}} = \frac{[\text{H}_5\text{C}_6\text{O}_5^-]}{[\text{H}_5\text{C}_6\text{O}_5^-] + [\text{H}_4\text{C}_6\text{O}_5^{2-}]} \quad \text{and} \quad \chi_{\text{base}} = \frac{[\text{H}_4\text{C}_6\text{O}_5^{2-}]}{[\text{H}_5\text{C}_6\text{O}_5^-] + [\text{H}_4\text{C}_6\text{O}_5^{2-}]}, \quad (2.42)$$

where χ_{acid} is the mole fraction of the acid form of the pH sensor molecule and χ_{base} is the mole fraction of the base form of the pH sensor molecule.

In the case of fast chemical exchange between the conjugate acid and base forms, which means that the site lifetimes are much shorter than the reciprocal of the resonance frequency difference between the two sites, the observed chemical shift δ is a mean of the chemical shift of the acid form of the pH sensor molecule δ_{acid} and the chemical shift of the base form of the pH sensor molecule δ_{base} , weighted by the respective acid and base mole fractions

$$\delta = \chi_{\text{acid}} \delta_{\text{acid}} + \chi_{\text{base}} \delta_{\text{base}}. \quad (2.43)$$

With the identity $\chi_{\text{acid}} + \chi_{\text{base}} = 1$, this leads to the two expressions

$$\chi_{\text{acid}} = \frac{\delta - \delta_{\text{base}}}{\delta_{\text{acid}} - \delta_{\text{base}}} \quad \text{and} \quad \chi_{\text{base}} = \frac{\delta - \delta_{\text{acid}}}{\delta_{\text{base}} - \delta_{\text{acid}}}, \quad (2.44)$$

which, by substitution into equation 2.41 in order to eliminate the two variables χ_{acid} and χ_{base} , result in the same form of the Henderson-Hasselbalch equation as was used to determine the intracellular pH (pH_i) from the observed chemical shift of inorganic phosphate (P_i , cf. equation 2.25), but this time to determine the extracellular pH (pH_e) from the observed chemical shift δ of zymonic acid by

$$\text{pH}_e(\delta) = \text{p}K_a + \log_{10} \left(\frac{\delta - \delta_{\text{min}}}{\delta_{\text{max}} - \delta} \right) \quad (2.45)$$

using the identities $\delta_{\text{acid}} = \delta_{\text{min}}$ and $\delta_{\text{base}} = \delta_{\text{max}}$ with the appropriate parameters from Table 2.2.

By solving equation 2.45 for δ and using the definition $\Delta\delta = \delta_{\text{max}} - \delta_{\text{min}}$ to eliminate δ_{max} , we can calculate the inverse of equation 2.45 and express the observed chemical shift δ as a function of pH according to

$$\delta(\text{pH}) = \delta_{\text{min}} + \frac{\Delta\delta}{1 + 10^{(\text{p}K_a - \text{pH})}}. \quad (2.46)$$

Fitting this equation to an NMR titration curve derived from chemical shifts of zymonic acid at six different pH values between pH 5–8 as shown in Fig. 4.1, equation 2.46 was used in Chapter 4 to extract the parameters for the calculation of extracellular pH values from ^{13}C chemical shifts of zymonic acid; the fitted parameters are summarized in Table 2.2.

Table 2.2: Parameters to calculate extracellular pH values from ^{13}C chemical shifts of zymonic acid. Values were obtained by fitting the Henderson-Hasselbalch equation 2.46 to NMR titration curves consisting of chemical shifts of zymonic acid at six different pH values between pH 5–8 as shown in Fig. 4.1 with ionic strength I and temperature ϑ . The ppm scale was referenced to the ^{13}C -chemical shift of ^{13}C -urea, which is usually observed at 165.5 ppm and which was set to 0 ppm. ZA, zymonic acid; $\text{p}K_a$, logarithmic acid dissociation constant; δ_{min} , limiting minimum (acid) chemical shift; δ_{max} , limiting maximum (base) chemical shift.

sensor molecule	atom position	chemical shift reference	$\text{p}K_a$	$\delta_{\text{min}}/\text{ppm}$	$\Delta\delta/\text{ppm}$	$\delta_{\text{max}}/\text{ppm}$	titration conditions
ZA	C ₁	urea	6.90	8.52	5.13	13.65	$I = 0.20 \text{ M}$
ZA	C ₅	urea	6.90	12.57	2.57	15.14	$\vartheta = 25 \text{ }^\circ\text{C}$

3 Multiparametric human hepatocellular carcinoma characterization and therapy response evaluation by hyperpolarized ^{13}C -MRSI

“It is a tribute to the inherent harmony and the organic growth of our branch of science that every advance in physics is largely due to the developments that preceded it.”

— Felix Bloch (* 1905; † 1983)

Reprinted from *NMR in Biomedicine*, vol. 29, pp. 952–960 (2016); Stephan Düwel*, Markus Durst*, Concetta V. Gringeri, Yvonne Kosanke, Claudia Gross, Martin A. Janich, Axel Haase, Steffen J. Glaser, Markus Schwaiger, Rolf F. Schulte, Rickmer Braren, and Marion I. Menzel. “Multiparametric human hepatocellular carcinoma characterization and therapy response evaluation by hyperpolarized ^{13}C MRSI”. With permissions from John Wiley & Sons, Ltd. Modifications: replacement of Abstract by Summary, addition of Appendix A. * contributed equally.

Summary

Individual tumor characterization and treatment response monitoring based on current medical imaging methods remain challenging. This work investigates hyperpolarized ^{13}C compounds in an orthotopic rat hepatocellular carcinoma (HCC) model system before and after transcatheter arterial embolization (TAE). HCC ranks amongst the top six most common cancer types in humans and accounts for

one-third of cancer-related deaths worldwide. Early therapy response monitoring could aid in the development of personalized therapy approaches and novel therapeutic concepts. Measurements with selectively ^{13}C -labeled and hyperpolarized urea, pyruvate and fumarate were performed in tumor-bearing rats before and after TAE. Two-dimensional, slice-selective MRSI was used to obtain spatially resolved maps of tumor perfusion, cell energy metabolic conversion rates and necrosis, which were additionally correlated with immunohistochemistry. All three injected compounds, taken together with their respective metabolites, exhibited similar signal distributions. TAE induced a decrease in blood flow into the tumor and thus a decrease in tumor to muscle and tumor to liver ratios of urea, pyruvate and its metabolites, alanine and lactate, whereas conversion rates remained stable or increased on TAE in tumor, muscle and liver tissue. Conversion from fumarate to malate successfully indicated individual levels of necrosis, and global malate signals after TAE suggested the washout of fumarase or malate itself on necrosis. This study presents a combination of three ^{13}C compounds as novel candidate biomarkers for a comprehensive characterization of genetically and molecularly diverse HCC using hyperpolarized MRSI, enabling the simultaneous detection of differences in tumor perfusion, metabolism and necrosis. If bolus dynamics are not required and if qualitative perfusion information is sufficient, the desired information could be extracted from hyperpolarized fumarate and pyruvate alone, acquired at higher fields with better spectral separation.

3.1 Introduction

Hepatocellular carcinoma (HCC) ranks amongst the top six most common cancer types in humans and accounts for one-third of cancer-related deaths worldwide [46]. A minority of patients with HCC are eligible for curative treatment options (i.e. liver transplantation, surgical resection and tumor ablation) [94–96]. In the case of unresectable HCC, transcatheter arterial chemoembolization (TACE) [104, 161], molecularly targeted therapies, such as the multikinase inhibitor sorafenib [96, 171], and combinations thereof, are employed. With selected therapies targeting specific molecular alterations that determine individual tumor progression, personalized approaches are increasingly being introduced into routine clinical cancer care. In particular, genetically and molecularly diverse HCC would benefit from such individual pre-therapeutic tumor assessment for the identification of patients with the best-predicted responses to specific treatments. Likewise, early response monitoring would help the development of novel therapeutic concepts.

Aimed at comprehensive tumor characterization for therapy response prediction and monitoring, several new imaging techniques have been introduced into HCC management over recent years, including structural and functional analyses by MR-based diffusion [19, 24, 118, 124, 170] and perfusion [12, 170] imaging, as well as positron emission tomography (PET)-based metabolic imaging [90, 158]. With the advent of dissolution dynamic nuclear polarization (DNP), the MR-based detection of endogenous ^{13}C -labeled substances holds promise for a far more advanced *in vivo*

analysis of several physiological and biochemical processes [11, 48]. First clinical studies in cancer patients using hyperpolarized biomarkers are currently being conducted and have already produced promising results [120].

Preclinically, $[1-^{13}\text{C}]$ pyruvate and downstream metabolites ($[1-^{13}\text{C}]$ lactate, $[1-^{13}\text{C}]$ -alanine or $[1-^{13}\text{C}]$ bicarbonate) are amongst the most researched compounds employed to analyse *in vivo* glucose metabolism of untreated [6, 20, 58] and treated [34, 35, 127] tumor tissue. Furthermore, $[1,4-^{13}\text{C}_2]$ fumarate with its metabolite, $[1,4-^{13}\text{C}_2]$ malate, has been tested for the early detection of tissue necrosis [16, 17, 51, 109, 167]. When the cell membrane integrity breaks down as a result of a necrotic event, the fumarase enzyme can be accessed by the injected fumarate and is rapidly converted to malate, which therefore can be used to quantify the amount of tissue damage.

Hyperpolarized ^{13}C -urea has been demonstrated to be a feasible perfusion agent [116, 117], as it is an endogenous, metabolically inactive molecule and can be measured simultaneously with pyruvate after copolarized injection. Together with metabolic information, it can provide valuable insights into the relationship between metabolism and perfusion. In addition, as tumor perfusion is reduced after certain types of treatment, it could be an important parameter for the evaluation of the success of tumor therapy.

To date, few studies have explored $[1-^{13}\text{C}]$ pyruvate in HCC for tissue characterization [33, 174] or therapy response evaluation [32], or in Myc-driven liver cancer with features of HCC and hepatoblastoma [67]. To test the potential of hyperpolarized ^{13}C -labeled substrates in HCC management, we performed MR measurements with $[1-^{13}\text{C}]$ pyruvate, $[1,4-^{13}\text{C}_2]$ fumarate and $[^{13}\text{C}, ^{15}\text{N}_2]$ urea in orthotopic rat HCC before and after transcatheter arterial embolization (TAE).

3.2 Materials and methods

During imaging, animals were maintained under isoflurane anesthesia (3% isoflurane, 1.5% oxygen; Abbott GmbH, Wiesbaden, Germany). Temperature and breathing were monitored continuously (SA Instruments Inc., New York, NY, USA).

Unifocal orthotopic tumor transplants were generated by the injection of 4×10^6 syngeneic McA-RH7777 rat HCC cells (American Type Culture Collection, Manassas, VA, USA) into the right lateral liver lobe of five 14-week-old female Buffalo rats (Harlan, Horst, the Netherlands). TAE was performed by the administration of 1 mL of 50% EmboCept[®] S (PharmaCept, Berlin, Germany) through the gastroduodenal artery, so that the embolizing agent penetrates into the small tumor vessels and produces a transient vessel occlusion. EmboCept[®] S is a sterile suspension of degradable starch microspheres with an average diameter of 50 μm (range, 20–200 μm). Instillation into the hepatic artery results in a transient reduction in blood flow, followed by α -amylase-mediated degradation with a plasma

half-life of 35–50 min. For histology, rats were killed according to animal care standards. Immediately after death, livers were fixed in 4% paraformaldehyde (PFA) in phosphate-buffered saline (PBS) solution for 24–48 h at 4 °C. Proton imaging data were reviewed, tumor nodules were identified in whole fixed livers, resected with adjacent liver tissue and paraffin embedded for histopathological processing according to the axial imaging plane. Serial 4 μm thick sections were collected every 500 μm and subjected to hematoxylin and eosin (H&E) staining for histological analysis (Mirax Viewer, Carl Zeiss MicroImaging GmbH, Göttingen, Germany). The percentage necrosis was quantified semi-automatically from a central tumor slice using Tissue Studio[®] software (Definiens Developer XD 64, Definiens, Munich, Germany) [19].

Animals were examined 12–13 days after cell implantation with the same protocol, 1 day before and 1 day after TAE. Injections of hyperpolarized $[1,4\text{-}^{13}\text{C}_2]\text{fumarate}$ and the copolarized $[^{13}\text{C},^{15}\text{N}_2]\text{urea}/[1\text{-}^{13}\text{C}]\text{pyruvate}$ solution were given within 1 h. The animal study, involving 28 animals in total, was approved by the local governmental committee for animal protection and welfare (Tierschutzbehörde, Regierung von Oberbayern). A number of animals ($n = 13$) were needed to establish the complex setup of the experiment; several animals had to be excluded because of peri-procedural complications, such as no tumor growth, low breathing and heart rate during the measurement, or because they did not survive the embolization procedure ($n = 10$), resulting in $n = 5$ animals included in the urea and pyruvate analysis, for which no sham experiments were conducted. As a result of the longer time needed for the hyperpolarization process and in order to keep the animals under anesthesia for as short a period as possible, the fumarate injection was always performed before the co-injection of pyruvate and urea.

$[1,4\text{-}^{13}\text{C}_2]\text{Fumaric acid}$ was hyperpolarized as follows. A solution of 25 μL of 4 M $[1,4\text{-}^{13}\text{C}_2]\text{fumaric acid}$ (Eurisotop, Saint-Aubin, France) in dry dimethyl sulfoxide (DMSO), 27 mM of the free radical OX063 (Oxford Instruments, Abingdon, Oxfordshire, UK) and 2.5 mM of the gadolinium chelate Dotarem (Guerbet, Villepinte, France) were added to a standard DNP sample cup, hyperpolarized using a HyperSense DNP polarizer (Oxford Instruments) at a microwave frequency of ≈ 94.1 GHz and dissolved in 40 mM phosphate buffer in deuterium oxide (D_2O), 0.5 M NaCl, 0.1 g L^{-1} ethylenediaminetetraacetic acid (EDTA) and NaOH for physiological pH and temperature, producing 20 mM hyperpolarized $[1,4\text{-}^{13}\text{C}_2]\text{fumarate}$. $[1\text{-}^{13}\text{C}]\text{Pyruvic acid}$ and $[^{13}\text{C},^{15}\text{N}_2]\text{urea}$ were hyperpolarized as follows. An aliquot of 23 μL of 14 M $[1\text{-}^{13}\text{C}]\text{pyruvic acid}$ (Eurisotop), with 15 mM OX063 and 1 mM Dotarem, was added to a standard DNP sample cup and frozen in liquid nitrogen. A solution of 40 μL of 10 M $[^{13}\text{C},^{15}\text{N}_2]\text{urea}$ (Eurisotop) in glycerol, 30 mM OX063 and 1.5 mM Dotarem were added on top of the frozen $[1\text{-}^{13}\text{C}]\text{pyruvic acid}$ layer and also frozen in liquid nitrogen. Both substances were simultaneously hyperpolarized at a microwave frequency of ≈ 94.105 GHz and dissolved in 80 mM tris(hydroxymethyl)aminomethane (Tris) buffer in D_2O , producing 80 mM hyperpolarized $[1\text{-}^{13}\text{C}]\text{pyruvate}/100$ mM hyperpolarized $[^{13}\text{C},^{15}\text{N}_2]\text{urea}$. A dissolution agent based on D_2O was used to decrease the dipolar coupling from the hyperpolarized substance to H_2O , and thus increase T_1 , mainly during the transport from the po-

larizer to the scanner. D₂O is fairly nontoxic for mammals if not given regularly at very high levels [88, 163], and has been used before to prolong T_1 , e.g. of pyruvate for *in vitro* experiments [142] and of bicarbonate for *in vivo* experiments [144]. Both solutions were injected with a dose of 5 mL kg⁻¹ at a rate of 0.2 mL s⁻¹ into the tail vein of the rats, separated by a time interval of 1 h. For anatomical reference, T_2 -weighted, breathing-triggered fast recovery fast spin echo (FRFSE) ¹H images were acquired with the centers of the carbon and proton slices at the same axial position (field of view, 8 cm; slice thickness, 3 mm; matrix, 256 × 256; echo train length, 13; number of signal averages (NEX) = 4; TR = 3740 ms; TE = 87 ms). All experiments were performed on a Signa HDxt 3.0 T clinical scanner (GE Healthcare, Milwaukee, WI, USA). A dual-tuned ¹³C-¹H birdcage volume coil with a diameter of 8 cm was used for radiofrequency (RF) transmission and reception [39].

For the [1-¹³C]pyruvate/[¹³C,¹⁵N₂]urea injection, a ¹³C iterative decomposition with echo asymmetry and least-squares estimation (IDEAL) spiral chemical shift imaging (CSI) sequence was used as described previously [165], with a field of view of 8 cm, slice thickness of 1 cm, nominal resolution of 32 × 32, flip angle α of 10°, $TR \approx 750$ ms, breathing triggered, and number of echoes of 7. The TE shift was set to 1.12 ms, adapting to the frequency offsets of [¹³C,¹⁵N₂]urea, [1-¹³C]pyruvate, [1-¹³C]alanine and [1-¹³C]lactate, and resulting in one complete ¹³C metabolite image set approximately every 6 s after the start of a 5 s injection. In the reconstruction implementation, an IDEAL fitting was used for the separation of the metabolites [137] and a non-uniform fast Fourier transform (NUFFT) algorithm for interpolation of the data onto a Cartesian grid [43]. The complete code for reconstruction of the IDEAL spiral CSI data can be found online [40]. Regions of interest (ROIs) were manually drawn by hand around the tumor, skeletal muscle and liver based on the anatomical ¹H images. Apparent rate constants describing forward label exchange from [1-¹³C]pyruvate to [1-¹³C]alanine ($k_{\text{pyr} \rightarrow \text{ala}}$) and from [1-¹³C]pyruvate to [1-¹³C]lactate ($k_{\text{pyr} \rightarrow \text{lac}}$) were calculated [83] by scaling the ratio of the time-integrated metabolite signals $\sum a_{\text{met},j}$ and time-integrated pyruvate signals $\sum a_{\text{pyr},j}$ according to

$$\frac{\sum a_{\text{met},j}}{\sum a_{\text{pyr},j}} = \frac{k_{\text{pyr} \rightarrow \text{met}}}{R_{\text{eff,met}}}, \quad R_{\text{eff,met}} = \frac{1}{T_{1,\text{met}}} + \frac{1 - \cos \alpha}{TR} + k_{\text{met} \rightarrow \text{pyr}} \quad (3.1)$$

where $a_{\text{met},j}$ is the metabolite signal amplitude at time j , $a_{\text{pyr},j}$ is the pyruvate signal amplitude at time j and $R_{\text{eff,met}}$ is the effective decay rate of the metabolite accounting for signal decay effects caused by T_1 relaxation, $T_{1,\text{met}} \approx 20$ s, repetitive excitation with flip angle α at a repetition rate TR and ignoring the reverse ¹³C label exchange [20] from the metabolites to pyruvate $k_{\text{met} \rightarrow \text{pyr}} = 0$. $T_{1,\text{met}}$ was estimated from previous studies and a constant relaxation rate was assumed [83]. Standard deviations for mean signal ratios (Fig. 3.4, see later) and apparent rate constants (Fig. 3.5, see later) were estimated from the ratio of the respective signals \pm noise, with the noise evaluated from the last time step of each acquisition time series.

For the [1,4-¹³C₂]fumarate injection, a spectral-spatial multiband pulse [89] with a slice thickness of 10 mm was designed and tailored to the spectrum of [1,4-¹³C₂]fumarate and [1,4-¹³C₂]malate (Fig. 3.4, see later). The ratio of [1,4-¹³C₂]fumarate

to $[1,4-^{13}\text{C}_2]$ malate excitation was chosen to be 1:5 to preserve $[1,4-^{13}\text{C}_2]$ fumarate polarization for further conversion. The pulse was designed with a flyback gradient modulation with nine sublobes and a total duration of 21 ms. Acquisition was started 20 s after injection at the estimated maximum $[1,4-^{13}\text{C}_2]$ malate concentration. First, a breathing-triggered IDEAL spiral [165] image was acquired using five echoes with single-shot spiral readout (field of view, 8 cm; nominal resolution, 32×32) and an echo shift of 1.05 ms. The flip angle was chosen between 35° and 90° for $[1,4-^{13}\text{C}_2]$ malate in different animals to find the optimal settings. Subsequently, a spectrum was acquired to quantify the overall $[1,4-^{13}\text{C}_2]$ malate increase and the metabolic dynamics. In the image reconstruction, the double resonance of the non-symmetric $[1,4-^{13}\text{C}_2]$ malate molecule was accounted for by including the condition of equal spin density for both isomers in the least-squares CSI separation approach, thereby increasing the signal-to-noise ratio (SNR) by a factor of $\sqrt{2}$. For spectral reconstruction, a blind matching pursuit algorithm [102, 165] was used to quantify the signal levels of $[1,4-^{13}\text{C}_2]$ fumarate and $[1,4-^{13}\text{C}_2]$ malate. Then, the signals were corrected for flip angle, and the ratio of $[1,4-^{13}\text{C}_2]$ malate to $[1,4-^{13}\text{C}_2]$ fumarate was calculated. Despite the low signal level of malate, this design allowed the acquisition of a single image for localization and a single spectrum for quantification within the same fumarate injection. Even though the malate signal appears later in untreated tumors (≈ 20 s) compared with tumors treated with the vascular disrupting agent combretastatin-A4-phosphate (≈ 13 s), it has been suggested that the ratio of malate to fumarate acquired ≈ 20 s after injection can be used as an equivalent marker of response compared with the forward label exchange rate constant from fumarate to malate [17]. Statistical analyses were performed using Student's paired-sample two-sided t-test or Student's two-sample t-test with unequal variances (MATLAB and Statistics Toolbox Release 2013b, MathWorks, Natick, MA, USA), where appropriate.

T_1 measurements were performed on a 1 T Minispec mq40 NMR analyzer (Bruker, Karlsruhe, Germany) acquiring free induction decays (FIDs) using $\alpha = 3^\circ\text{C}$, $TR = 10$ s and 20 scans. The hyperpolarized T_1 decay curves were flip angle corrected and fitted to a mono-exponential decay curve. To determine the solution polarization level, the hyperpolarized signal intensity was extrapolated to the time of dissolution using the previously fitted T_1 . The thermal signal was measured with a Carr-Purcell-Meiboom-Gill (CPMG) sequence with $TE = 2$ ms, acquisition time of 0.25 ms, $TR = 300$ s, 600 echoes and 10 scans.

3.3 Results

$[1,4-^{13}\text{C}_2]$ Fumarate was hyperpolarized to a liquid-state polarization level of approximately 25 % with $T_1(\text{D}_2\text{O}) \approx 70$ s at 1 T and 37°C . $[1-^{13}\text{C}]$ Pyruvate and $[^{13}\text{C},^{15}\text{N}_2]$ -urea were hyperpolarized to liquid-state polarization levels of approximately 31 % and 30 % with $T_1(\text{D}_2\text{O}) \approx 123$ s and 116 s, respectively, at 1 T and 37°C .

A representative dataset of $[1,4-^{13}\text{C}_2]$ fumarate and malate spectra before (pre) and

after (post) TAE is shown in Fig. 3.1a. The two $[1,4-^{13}\text{C}_2]$ malate peaks were detected at offsets of +6.4 and +5.2 ppm with respect to $[1,4-^{13}\text{C}_2]$ fumarate at 177.2 ppm. $[1,4-^{13}\text{C}_2]$ Malate to $[1,4-^{13}\text{C}_2]$ fumarate ratios (mean \pm standard error of the mean) increased significantly (pre: 0.003 ± 0.004 , $n = 15$; post: 0.149 ± 0.074 , $n = 8$, $p < 0.001$; post sham: 0.013 ± 0.015 , $n = 4$, $p = 0.28$) on histologically confirmed necrosis formation (Fig. 3.1b). However, the higher $[1,4-^{13}\text{C}_2]$ malate to fumarate ratio was not restricted to the tumor slice but, after TAE, also evident in neighboring slices (0.096 ± 0.055 , $n = 9$, $p < 0.001$). Nevertheless, $[1,4-^{13}\text{C}_2]$ malate to $[1,4-^{13}\text{C}_2]$ -fumarate ratios correlated well with the histologically quantified amount of tumor necrosis (Fig. 3.1c, $R^2 = 0.86$). Imaging experiments confirmed these findings with very low initial SNR of $[1,4-^{13}\text{C}_2]$ malate (Fig. 3.2) and a post-interventional $[1,4-^{13}\text{C}_2]$ malate signal distribution pattern beyond the tumor region, similar to the $[1,4-^{13}\text{C}_2]$ fumarate signal.

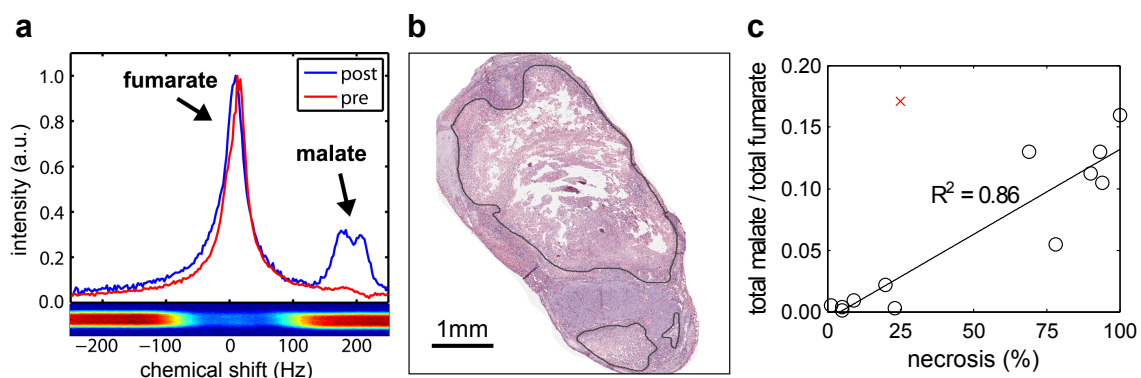


Figure 3.1: Correlation of detected $[1,4-^{13}\text{C}_2]$ malate and amount of tumor necrosis. (a) Representative spectra of $[1,4-^{13}\text{C}_2]$ fumarate and $[1,4-^{13}\text{C}_2]$ malate before and after transcatheter arterial embolization of an axial slice through the tumor. For comparison, spectra were normalized to the maximum fumarate signal within each spectrum. The excitation pulse profile is shown below with colors indicating the spectral and spatial variation of the applied flip angle. (b) A representative micrograph of a hematoxylin and eosin (H&E)-stained central histological section showing the amount of tumor necrosis. (c) The ratio of total malate to total fumarate correlates with the amount of necrosis detected by histology.

$[^{13}\text{C}, ^{15}\text{N}_2]$ urea, $[1-^{13}\text{C}]$ pyruvate and $[1-^{13}\text{C}]$ lactate were detected at offsets of -12.8 , -5.5 and $+6.7$ ppm with respect to $[1-^{13}\text{C}]$ alanine at 178.5 ppm. By visual inspection, $[^{13}\text{C}, ^{15}\text{N}_2]$ urea and $[1-^{13}\text{C}]$ pyruvate exhibited a similar signal distribution pattern, predominantly localized to major blood vessels (i.e. vena cava, aorta) and kidneys, independent of the embolization state (Fig. 3.3). In contrast, the signals of the $[1-^{13}\text{C}]$ pyruvate metabolites, $[1-^{13}\text{C}]$ alanine and $[1-^{13}\text{C}]$ lactate, were localized to the tumor region (Fig. 3.3, top row), indicating tumor-specific $[1-^{13}\text{C}]$ pyruvate conversion. On TAE intervention (Fig. 3.3, bottom row), this signal was diminished or abolished depending on the amount of tumor necrosis and, in addition, the $[1-^{13}\text{C}]$ lactate signal was commonly identified in the kidneys. Quantitative analysis of local mean signal intensities before and after TAE revealed a decrease in $[^{13}\text{C}, ^{15}\text{N}_2]$ -urea, $[1-^{13}\text{C}]$ pyruvate, $[1-^{13}\text{C}]$ alanine and $[1-^{13}\text{C}]$ lactate tumor to muscle (Fig. 3.4a;

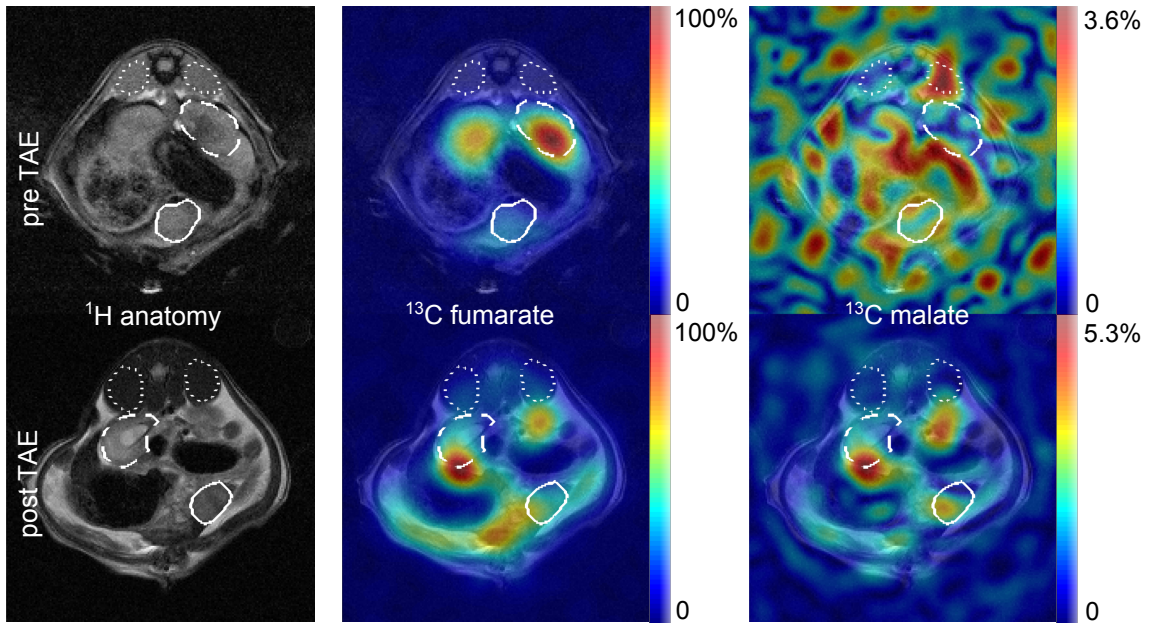


Figure 3.2: Representative images for a $[1,4-^{13}\text{C}_2]$ fumarate injection of an axial slice through the kidney and tumor before (first row) and after (second row) transcatheter arterial embolization (TAE). The ^1H anatomy images in the first column show the muscle (dotted line), kidney (dashed line) and tumor (solid line) within each slice. The remaining columns show false-color ^{13}C images of $[1,4-^{13}\text{C}_2]$ fumarate and $[1,4-^{13}\text{C}_2]$ malate superimposed on the anatomical image and scaled to the maximum signal intensity of $[1,4-^{13}\text{C}_2]$ fumarate within each injection, taking into account the different flip angles applied to fumarate and malate due to the spectral-spatial multiband pulse.

urea: $n = 4$, $p = 0.08$; pyruvate: $n = 5$, $p = 0.06$; alanine: $n = 5$, $p = 0.10$; lactate: $n = 5$, $p = 0.06$) and tumor to liver (Fig. 3.4b; urea: $n = 4$, $p = 0.17$; pyruvate: $n = 4$, $p = 0.44$; alanine: $n = 4$, $p = 0.12$; lactate: $n = 4$, $p = 0.06$) ratios on TAE. In addition, tissue-specific apparent rate constants before and after TAE, describing forward label exchange from $[1-^{13}\text{C}]$ pyruvate to alanine ($k_{\text{pyr} \rightarrow \text{ala}}$) or to lactate ($k_{\text{pyr} \rightarrow \text{lac}}$), were calculated (Fig. 3.5). In tumor (Fig. 3.5a) and muscle tissue (Fig. 3.5b), $k_{\text{pyr} \rightarrow \text{ala}}$ showed no significant change (tumor: $n = 5$, $p = 0.15$; muscle: $n = 5$, $p = 0.99$). In contrast, $k_{\text{pyr} \rightarrow \text{lac}}$ significantly increased in both tissues (both tissues $n = 5$, $p < 0.01$). In liver tissue (Fig. 3.5c), both $k_{\text{pyr} \rightarrow \text{ala}}$ and $k_{\text{pyr} \rightarrow \text{lac}}$ (both metabolites $n = 4$, $p < 0.05$) significantly increased after TAE intervention. We further observed a notable variability of ^{13}C substrate and metabolite signals (Fig. 3.4), as well as apparent rate constants (Fig. 3.5) of untreated (overall mean coefficient of variation pre TAE of 44 % for mean signals and 36 % for apparent rate constants) and treated (overall mean coefficient of variation post TAE of 31 % for mean signals and 27 % for apparent rate constants) tumors.

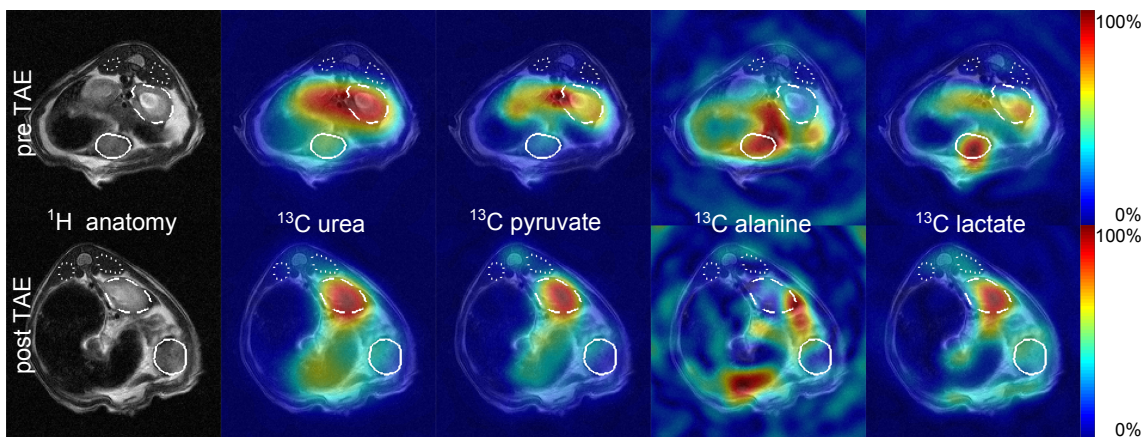


Figure 3.3: Representative images for a copolarized $[^{13}\text{C}, ^{15}\text{N}_2]$ urea and $[1-^{13}\text{C}]$ pyruvate injection of an axial slice through the kidney and tumor before (first row) and after (second row) transcatheter arterial embolization (TAE). The ^1H anatomy images in the first column show the muscle (dotted line), kidney (dashed line) and tumor (solid line) within each slice. The tumor position changed considerably during the embolization procedure. The remaining columns show false-color ^{13}C images of the sum over all time steps of $[^{13}\text{C}, ^{15}\text{N}_2]$ urea, $[1-^{13}\text{C}]$ pyruvate, $[1-^{13}\text{C}]$ alanine and $[1-^{13}\text{C}]$ -lactate superimposed on the anatomical image and scaled to the maximum signal intensity within each image.

3.4 Discussion

This study presents the first combined implementation of hyperpolarized $[^{13}\text{C}, ^{15}\text{N}_2]$ -urea, $[1-^{13}\text{C}]$ pyruvate and $[1,4-^{13}\text{C}_2]$ fumarate MRSI for the simultaneous investigation of tumor perfusion, metabolism and necrosis formation in an orthotopic rat HCC model system.

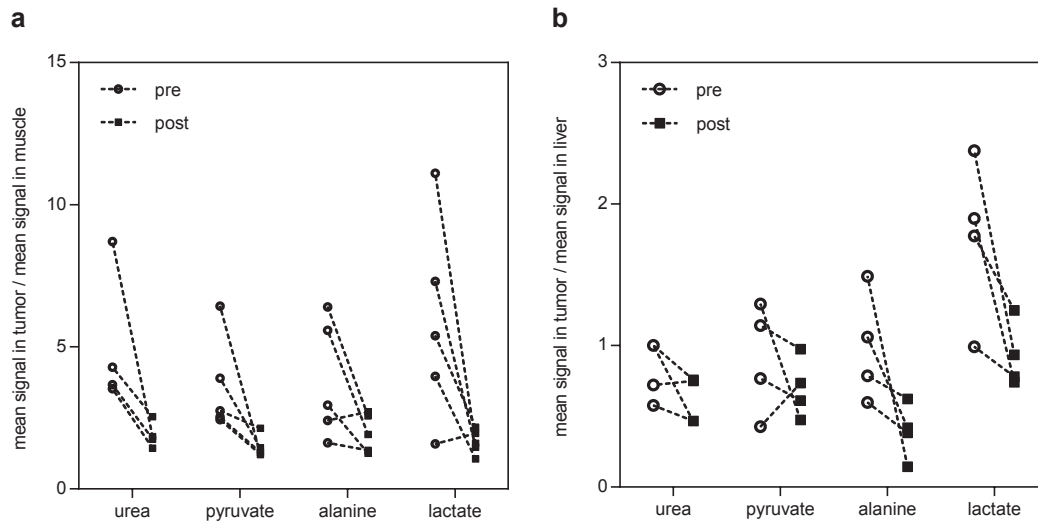


Figure 3.4: Mean signal in the tumor normalized to the mean signal in the muscle and the mean signal in the liver. $[^{13}\text{C},^{15}\text{N}_2]$ urea, $[1-^{13}\text{C}]$ pyruvate, $[1-^{13}\text{C}]$ -alanine and $[1-^{13}\text{C}]$ lactate are shown before (circles) and after (squares) transcatheter arterial embolization. Typical standard deviations (not shown) are on the order of 5% of the displayed ratios. Regions of interest for the tumor, muscle and liver were drawn by hand based on the anatomical ^1H images. (a) Mean signal in the tumor normalized to the mean signal in the muscle. (b) Mean signal in the tumor normalized to the mean signal in the liver.

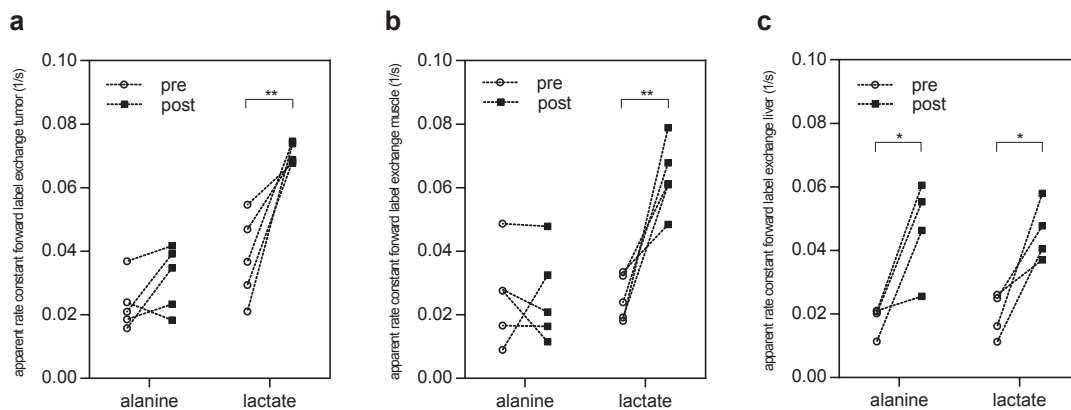


Figure 3.5: Apparent rate constants describing forward label exchange from $[1-^{13}\text{C}]$ pyruvate to $[1-^{13}\text{C}]$ alanine and from $[1-^{13}\text{C}]$ pyruvate to $[1-^{13}\text{C}]$ lactate. Apparent rate constants in (a) the tumor ($n = 5$), (b) muscle ($n = 5$) and (c) liver ($n = 4$), both before (circles) and after (squares) transcatheter arterial embolization. Typical standard deviations (not shown) are on the order of 5% of the displayed apparent rate constants. * $p < 0.05$; ** $p < 0.01$.

[1,4-¹³C₂]Fumarate and malate MRSI was identified as a robust marker of TAE-induced necrosis in orthotopic rat HCC, showing a significant increase in the [1,4-¹³C₂]malate signal after embolization, whereas the [1,4-¹³C₂]malate level of the sham-operated control group remained very low. Interestingly, although not localized within the tumor, the total [1,4-¹³C₂]malate signal correlated with histologically confirmed tumor necrosis. An elevated metabolite (i.e. malate) signal indicates an increased access of the substrate (i.e. fumarate) to the enzyme, caused by cell membrane permeabilization, during the course of necrosis. The malate signal detected outside the necrotic tissue was either caused by malate produced inside the necrotic tissue, and then washed out between the injection of fumarate and the signal acquisition of malate, or by the enzyme washed out before the injection and malate produced from fumarate coming into contact with the enzyme wherever the enzyme was deposited. Washout of fumarase from necrotic areas was previously tentatively identified after bevacizumab treatment in a xenograft colon cancer mouse model [16]. In contrast, previous results on [1,4-¹³C₂]fumarate MRSI of etoposide treatment in a syngeneic lymphoma mouse model showed an increase in local [1,4-¹³C₂]malate signal only; however, a signal spill beyond the tumor borders was also noted in this experimental setup [51]. As it was unknown how much malate was formed and how fast the conversion would be in the necrotic tumors, different flip angles were used in order to obtain an optimal SNR. Initially, the imaging experiments were performed with a flip angle of 90° for malate, but this was finally reduced to 35° for malate. This flip angle results in an image with sufficient SNR, and sufficient magnetization remains to produce a subsequent spectrum with sufficient SNR. As different animals exhibited different levels of necrosis, the reproducibility among the malate/fumarate experiments can be judged by the good correlation with the necrosis level determined from histology (Fig. 3.1c, $R^2 = 0.86$). Further experiments with varying time delay after TAE are necessary to identify the most suitable time point for response to therapy evaluation.

Furthermore, a local decrease in the [¹³C, ¹⁵N₂]urea and [1-¹³C]pyruvate signals and an increase in the apparent conversion rate $k_{\text{pyr} \rightarrow \text{lac}}$ were noted. These data indicate reduced perfusion and increased hypoxic glycolysis, as expected on TAE treatment. It has been demonstrated previously that perfusion fitting can be performed using hyperpolarized urea [116, 117]. For this reason, in this work, pyruvate was copolarized with urea, and both substances were co-injected and both signals were acquired. A decrease in the urea signal in the tumor from before to after embolization, when normalized by either the muscle or liver signal, shows the reduced perfusion of the embolized tumor. We also noted an increase in $k_{\text{pyr} \rightarrow \text{lac}}$ of muscle and liver tissue, probably caused by collateral systemic effects of hepatic artery TAE. Elevated $k_{\text{pyr} \rightarrow \text{lac}}$ in muscle tissue could result from starch microspheres transported to the periphery as a result of shunting in the liver, which would result in peripheral organ (e.g. muscle tissue) damage. A further possibility is that lactate is washed out from the tumor and systemically distributed, leading to an apparent increase in $k_{\text{pyr} \rightarrow \text{lac}}$ in muscle tissue post-TAE. For an evaluation of the signal level in the tumor independent of the hyperpolarization level and the systemic effects mentioned above, tumor signals in Fig. 3.4 were displayed normalized by the signal level in the muscle and liver. Previous studies with a switchable transgenic mouse

model of Myc-driven liver cancer with features of HCC and hepatoblastoma showed a decreased pyruvate to lactate flux after 3 days of doxycycline treatment as an indicator of early regression [67]. The increase in the apparent conversion rate 24 h after TAE treatment could thus indicate a different behavior of HCC towards TAE and doxycycline treatment. Again, further experiments with varying time delay after TAE are necessary to exclude the possibility that the observed difference is only caused by the different imaging time points (1 day for TAE versus 3 days for doxycycline) after treatment.

Interestingly, untreated tumors exhibited a notable amount of interindividual variability of normalized (i.e. tumor to muscle and tumor to liver ratios) $[1-^{13}\text{C}]$ pyruvate and $[1-^{13}\text{C}]$ metabolite signals, as well as conversion rates (Figs 4, 5, Supporting information Figs S1 and S2). Similar to these observations, $[^{18}\text{F}]$ -fluorodeoxyglucose ($[^{18}\text{F}]$ -FDG) PET imaging has shown notable variability [19]. Previous studies have suggested spontaneous tumor necrosis [7, 19] and perfusion [154] as sources of variability. However, in addition, differences in glucose metabolism are likely, providing an interesting target not only for tumor detection, but also therapy [128]. The calculation of $[1-^{13}\text{C}]$ pyruvate apparent conversion rates provides the opportunity to further dissect glucose metabolism, i.e. anaerobic lactic acid production versus mitochondrial oxidization, in HCC and other tumors, without confounding differences in perfusion status. With tumor heterogeneity as a major source of treatment failure, our finding further underlines the potential of ^{13}C -MRSI for a more detailed tumor characterization.

The hyperpolarized signal distribution shows consistency of $[^{13}\text{C},^{15}\text{N}_2]$ urea, $[1-^{13}\text{C}]$ pyruvate and $[1,4-^{13}\text{C}_2]$ fumarate. This finding suggests that qualitative perfusion information could be based solely on $[1-^{13}\text{C}]$ pyruvate or $[1,4-^{13}\text{C}_2]$ fumarate injections without the need for copolarization with $[^{13}\text{C},^{15}\text{N}_2]$ urea. Future work with higher spectral resolution could combine $[1,4-^{13}\text{C}_2]$ fumarate and $[1-^{13}\text{C}]$ pyruvate into one copolarization [166] without having to add $[^{13}\text{C},^{15}\text{N}_2]$ urea as a third component. Whilst reducing the complexity of the copolarization process, this could still provide simultaneous information on tumor perfusion. Furthermore, a bolus tracking approach [41] could be used to dynamically adapt the acquisition to the tumor perfusion.

There are limitations to this study. As a result of the low SNR, the spatial resolution of ^{13}C -MRSI is still limited, causing partial volume effects. The nominal resolution of 2.5 mm in-plane corresponds to the highest sampled k -space frequency, i.e. the radius of the spiral trajectory in k -space. As a result of T_2^* decay, additional blurring broadens the point spread function (PSF) to a physical resolution of about 5 mm [40]. Furthermore, the ^{15}N label of $[^{13}\text{C},^{15}\text{N}_2]$ urea causes the ^{13}C peak of urea to split by 19–20 Hz [28, 136] because of J coupling, resulting in an additional peak broadening and reduction in resolution. Simulations of the IDEAL spiral acquisition scheme performed as described in ref. [40] show that an off-resonance of 20 Hz will lead to a broadening of the full width at half-maximum (FWHM) of the PSF by a factor of ≈ 1.5 , resulting in a resolution of about 7.5 mm for $[^{13}\text{C},^{15}\text{N}_2]$ urea, as opposed to about 5 mm without off-resonance. These technical hurdles currently

prevent the detection of intratumoral heterogeneity. When judging the significance of the results from the fumarate analysis compared with the urea and pyruvate analysis, the larger number of animals involved in the fumarate analysis and the fact that no sham experiments were performed for the urea and pyruvate analysis should be kept in mind. Furthermore, the employed orthotopic HCC implantation model, by nature, presents a high level of metabolic homogeneity and uniform response to TAE intervention. Future studies will need to make use of more realistic model systems to further explore the potential of ^{13}C -MRSI for the detection of differences in tumor metabolism.

3.5 Conclusions

The multiparametric approach used in this study provides valuable information on tumor perfusion, glucose metabolism and TAE-induced tumor necrosis. Although the perfusion information provided by $[^{13}\text{C}, ^{15}\text{N}_2]$ urea and $[1-^{13}\text{C}]$ pyruvate and the increase in the $[1,4-^{13}\text{C}_2]$ malate to fumarate ratio indicating necrosis showed clear trends, the metabolic activity of $[1-^{13}\text{C}]$ pyruvate is less conclusive. The comparatively small number of animals that could be included in the urea and pyruvate analysis should be taken into consideration, but this observation suggests that, in the given treatment scenario, $[1-^{13}\text{C}]$ pyruvate alone might not provide a sufficient indicator of treatment response, as it depends on a multitude of influencing conditions, such as the degree of necrosis, local perfusion of the tumor or current tumor activity. As tumor metabolism and viability, as well as the general health status of human cancer patients, can also vary dramatically, our study underlines the importance of multiparametric examinations for future clinical trials.

3.6 Acknowledgements

We would like to express our gratitude to Iryna Skuratovska for excellent technical assistance.

This work was supported by the German Research Foundation (DFG) within the SFB collaborative research center 824 ‘Imaging for Selection, Monitoring and Individualization of Cancer Therapies’ to R.B. (SFB 824, project C6) and to S.D., M.S., A.H., M.I.M. (SFB 824, project A5), and the German Bundesministerium für Bildung und Forschung (BMBF), grant number FKZ 13EZ1114, to S.D., M.D., C.V.G., A.H., S.J.G., R.F.S. and M.I.M.

M.A.J., R.F.S. and M.I.M. are employed by GE Global Research.

3.7 Appendix A: Supplementary Material

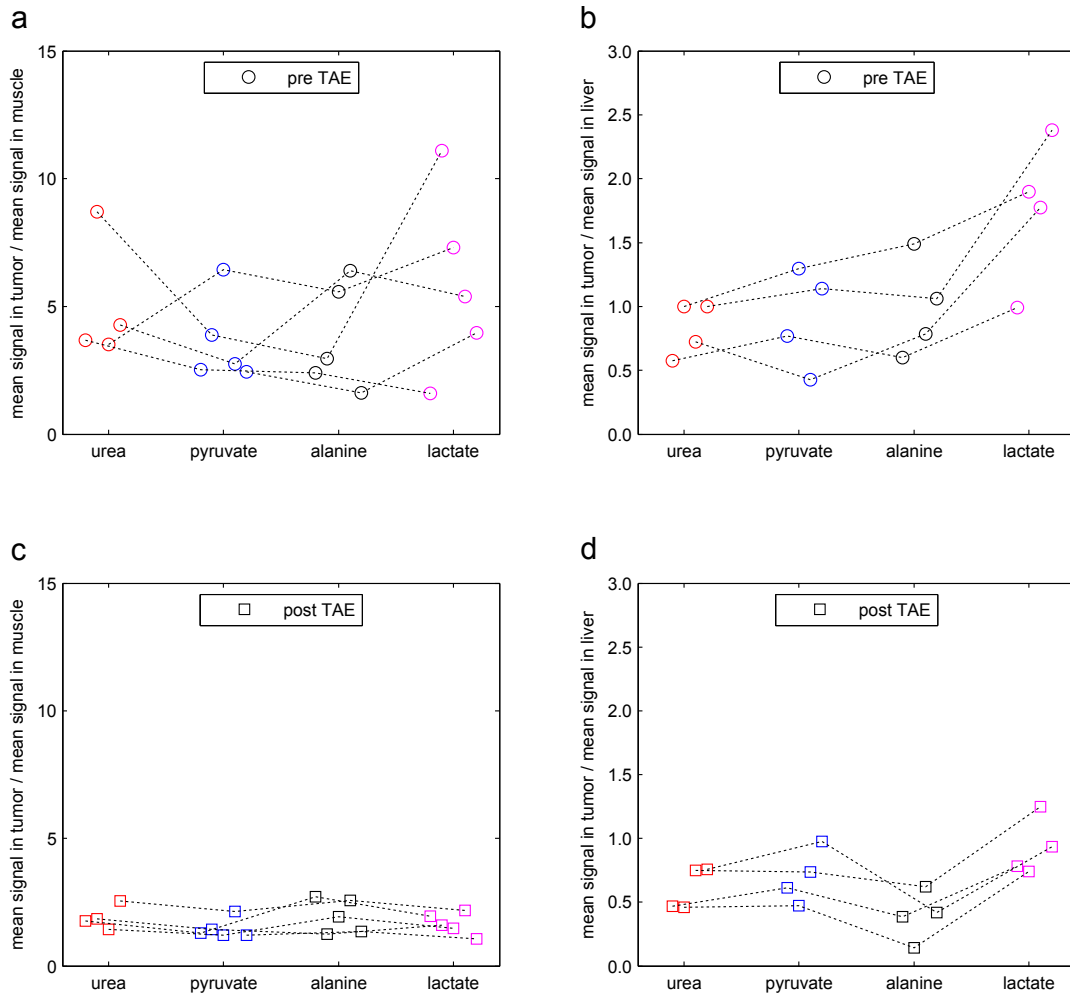


Figure 3.6: Mean signal in the tumor normalized to the mean signal in the muscle and the mean signal in the liver. $[^{13}\text{C}, ^{15}\text{N}_2]$ urea, $[1-^{13}\text{C}]$ pyruvate, $[1-^{13}\text{C}]$ alanine and $[1-^{13}\text{C}]$ lactate are shown before transcatheter arterial embolization for the mean signal in the tumor normalized by (a) the mean signal in the muscle and (b) the mean signal in the liver and after transcatheter arterial embolization for the mean signal in the tumor normalized by (c) the mean signal in the muscle and (d) the mean signal in the liver. Urea, pyruvate, alanine and lactate data collected simultaneously from the same animals are connected by a dotted line. This is the same data as shown in Fig. 3.4 of the manuscript this time stressing the visualization of data belonging to the same animal.

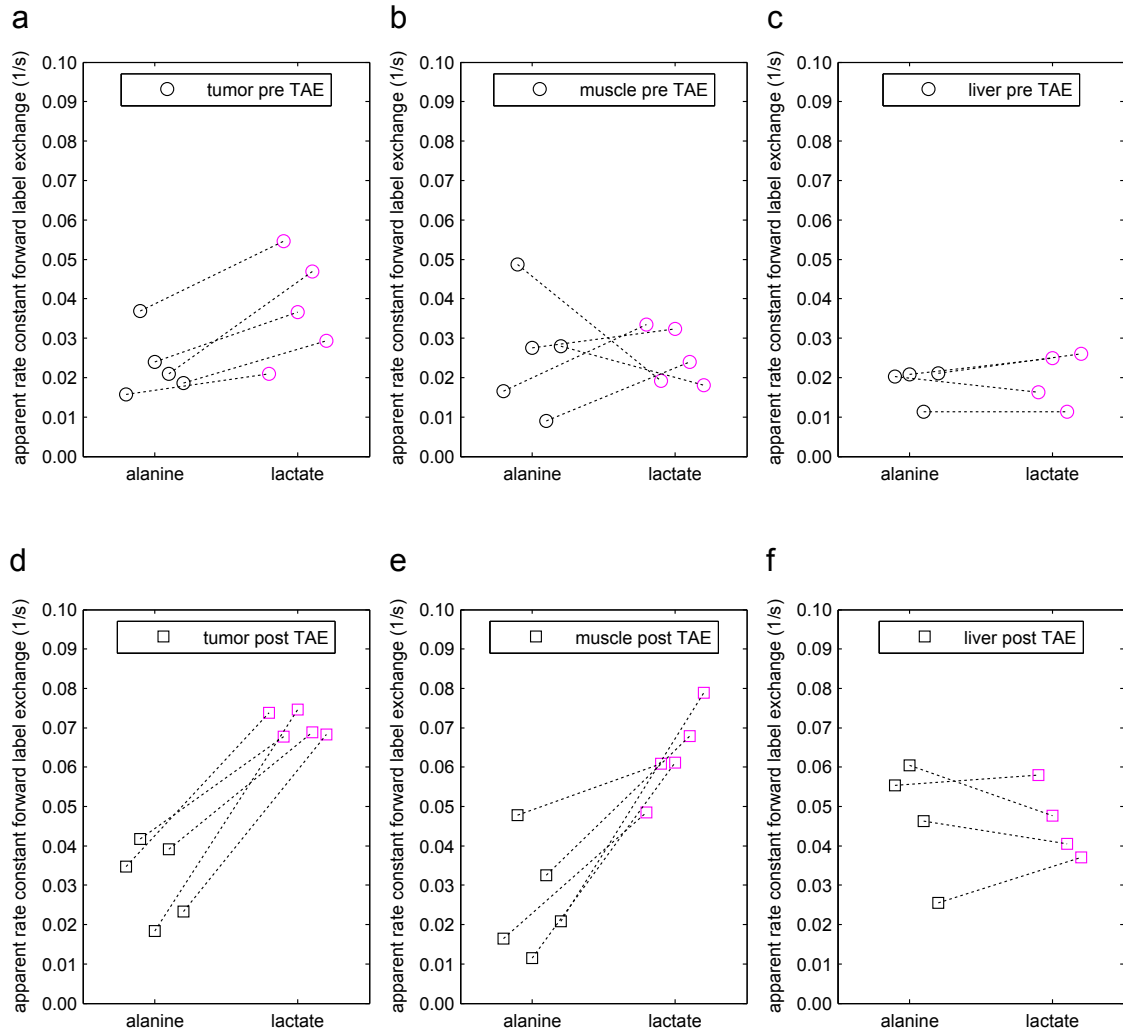


Figure 3.7: Apparent rate constant describing forward label exchange from $[1-^{13}\text{C}]$ pyruvate to $[1-^{13}\text{C}]$ alanine and from $[1-^{13}\text{C}]$ pyruvate to $[1-^{13}\text{C}]$ lactate. Apparent rate constant before transcatheter arterial embolization in (a) the tumor ($n = 5$), (b) the muscle ($n = 5$) and (c) the liver ($n = 4$) as well as after transcatheter arterial embolization in (d) the tumor ($n = 5$), (e) the muscle ($n = 5$) and (f) the liver ($n = 4$). Alanine and lactate data collected simultaneously from the same animals are connected by a dotted line. This is the same data as shown in Fig. 3.5 of the manuscript this time stressing the visualization of data belonging to the same animal.

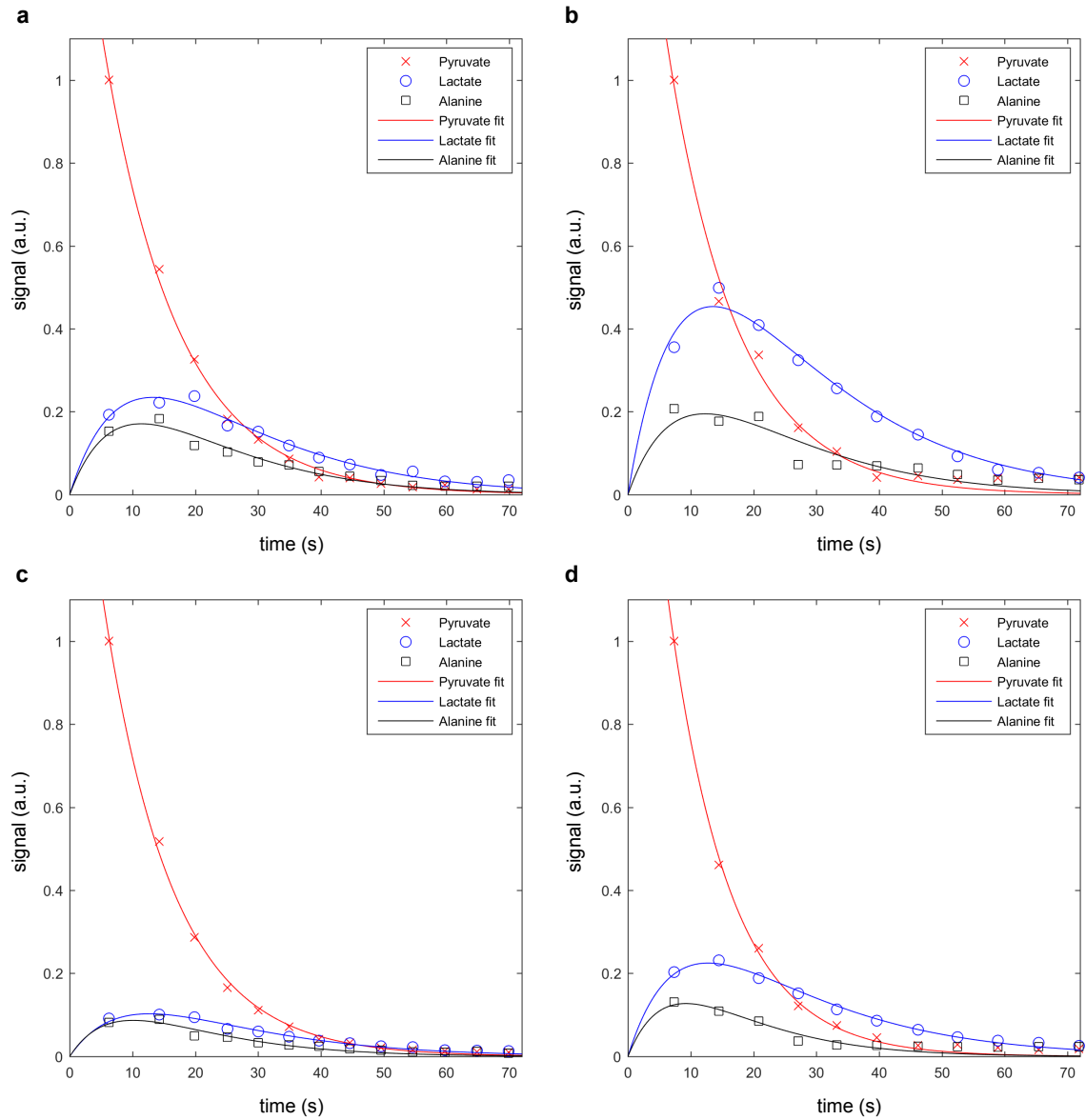


Figure 3.8: A typical time course of the flip angle corrected and normalized signal for a hyperpolarized $[1-^{13}\text{C}]$ pyruvate injection of the same animal pre and post TAE. Experimental data from $[1-^{13}\text{C}]$ pyruvate, $[1-^{13}\text{C}]$ lactate, $[1-^{13}\text{C}]$ alanine and their respective fitted models as a function of time within (a) a tumor ROI pre TAE, (b) a tumor ROI post TAE, (c) a liver ROI pre TAE and (d) a liver ROI post TAE from the same animal. The statistically significant increase in the apparent rate constant quantified in Fig. 3.5a is reflected in the notably higher $[1-^{13}\text{C}]$ lactate signal post TAE compared to pre TAE in the tumor ROI. The increase in the apparent rate constant quantified in Fig. 3.5c is reflected in the higher $[1-^{13}\text{C}]$ alanine and $[1-^{13}\text{C}]$ lactate signal post TAE compared to pre TAE in the liver ROI. For the muscle ROI, building the signal ratios as described in the manuscript is more robust than fitting apparent rate constants and relaxation parameters simultaneously. The data was fitted to a two-site exchange kinetic model with $k_{\text{met} \rightarrow \text{pyr}}$ set to zero as described before [142].

4 Imaging of pH *in vivo* using hyperpolarized ^{13}C -labeled zymonic acid

“But not only for physicists is nuclear magnetic resonance of great fascination. More and more chemists, biologists, and medical doctors discover NMR, not so much for its conceptual beauty but for its extraordinary usefulness.”

— Richard R. Ernst (* 1933)

Reprinted from *Nature Communications*, vol. 8, p. 15126 (2017); Stephan Düwel, Christian Hundhammer, Malte Gersch, Benedikt Feuerecker, Katja Steiger, Achim Buck, Axel Walch, Axel Haase, Steffen J. Glaser, Markus Schwaiger, and Franz Schilling. “Imaging of pH *in vivo* using hyperpolarized ^{13}C -labeled zymonic acid”. Modifications: replacement of Abstract by Summary, addition of Appendix A.

Summary

Natural pH regulatory mechanisms can be overruled during several pathologies such as cancer, inflammation, and ischemia, leading to local pH changes in the human body. Here we demonstrate that ^{13}C -labeled zymonic acid (ZA) can be used as hyperpolarized magnetic resonance pH imaging sensor. ZA is synthesized from [1- ^{13}C]pyruvic acid and its ^{13}C resonance frequencies shift up to 3.0 ppm per pH unit in the physiological pH range. The long lifetime of the hyperpolarized signal enhancement enables monitoring of pH, independent of concentration, temperature, ionic strength and protein concentration. We show *in vivo* pH maps within rat kidneys and subcutaneously inoculated tumors derived from a mammary adenocarcinoma cell line and characterize ZA as non-toxic compound predominantly present in the

extracellular space. We suggest that ZA represents a reliable and non-invasive extracellular imaging sensor to localize and quantify pH, with the potential to improve understanding, diagnosis and therapy of diseases characterized by aberrant acid-base balance.

4.1 Introduction

Maintaining acid-base balance is critical for the survival of living species since cellular processes are highly sensitive to changes in proton concentrations. In humans, pH is mainly regulated by the $\text{CO}_2/\text{HCO}_3^-$ buffer within a narrow pH range, in the blood between pH 7.35 and 7.45. Locally, deviations from the systemic pH are often caused by pathologies, such as cancer, inflammation, infection, ischemia, renal failure or pulmonary disease [56]. Tumors can acidify their extracellular environment during aerobic glycolysis and increased export of lactic acid, an effect that can even be further enhanced by the reduced buffer capacity of tumor interstitial fluid and poor tumor perfusion [79]. Because of its potentially broad impact, non-invasive imaging of local pH changes has been a major goal in biomedical research, even though so far no technique to measure extracellular pH has been applicable in the clinic.

The majority of approaches for non-invasive pH imaging focused on magnetic resonance imaging (MRI) because of its high spatial resolution and excellent soft-tissue contrast. In addition, optical methods [66] and radioactive tracers [141] for positron-emission-tomography (PET) have been developed. Magnetic resonance spectroscopy (MRS)-based pH sensor molecules exploit pH-induced changes in nuclear magnetic resonance (NMR) parameters, such as chemical shifts of individual atomic nuclei, which are sensitive to the protonation state of the molecule and therefore the surrounding pH [56]. To increase sensitivity, gadolinium and lanthanide complexes as well as iodinated contrast agents with pH-dependent chemical exchange or relaxation properties were developed [26, 37, 107]. Endogenous amide proton transfer (APT) chemical exchange saturation transfer (CEST) experiments [180] utilizing the pH-dependent proton exchange from predominantly intracellular proteins are currently used to study pH in the brain *in human*.

Dissolution dynamic nuclear polarization (DNP) revolutionized MRS by lifting nuclear spin polarization to a so-called hyperpolarized state leading to a sensitivity gain by more than four orders of magnitude [11]. Most prominently, hyperpolarized $[1-^{13}\text{C}]$ pyruvic acid is currently being used in clinical studies to examine its use for metabolic imaging of prostate carcinoma [121]. Hyperpolarized ^{13}C -labeled bicarbonate has been proposed as a probe for clinical pH imaging based on the determination of the ratio of $\text{CO}_2/\text{HCO}_3^-$ and recently, spectroscopic pH imaging methods have been revived and demonstrated *in vitro* including hyperpolarized ^{15}N -pyridine derivatives [74] and hyperpolarized ^{13}C -labeled Good's buffers [44]. Still, a non-invasive clinical method for pH imaging is lacking so far.

In this work, we introduce hyperpolarized [1,5- $^{13}\text{C}_2$]zymonic acid (ZA) as a novel probe for MRI of pH. We demonstrate that using ZA we can non-invasively image extracellular pH both *in vitro* and *in vivo* in the bladder, the kidneys and a tumor model. ZA's non-toxicity, its long lifetime of the hyperpolarization enhancement and its strong sensitivity to pH changes render this new technique valuable for further preclinical and clinical studies using extracellular pH as an imaging biomarker to characterize pathologies with aberrant acid-base balance.

4.2 Results

4.2.1 Synthesis and hyperpolarization of ZA

While studying metabolism in tumor cell spheroids using hyperpolarized pyruvate for ^{13}C -NMR spectroscopy [142], we noticed two additional unassigned peaks, whose changes in chemical shift correlated with the extracellular pH in the cell medium (Fig. 4.6). We found unassigned peaks with similar chemical shifts in the literature [61, 78, 173]. NMR spectra with unlabeled and fully ^{13}C -labeled, highly concentrated pyruvic acid revealed the presence of three chemical impurities of pyruvic acid, and we identified the pH-sensitive molecule as ZA, based on its ^1H and ^{13}C chemical shifts and coupling constants (Fig. 4.7 and Fig. 4.8) [105].

When synthesized [76] (see Methods for details) from selectively ^{13}C -labeled [1- ^{13}C]pyruvic acid, ZA bears two ^{13}C -NMR-active spin $1/2$ nuclei and is suitable for long-term storage. In aqueous solution, ZA slowly hydrolyses to parapyruvate (PP) with a half-life of ~ 2.5 h (Fig. 4.9). ZA thus stays chemically intact long enough for experimentation. To increase sensitivity in ^{13}C experiments, we developed a hyperpolarization protocol for ZA, and used simultaneously polarized, metabolically inactive ^{13}C -urea [166] as a chemical shift reference, although a pH determination based solely on the difference in chemical shift of the two ^{13}C nuclei of ZA is possible as well, but with a lower dynamical range (Fig. 4.10). This resulted in a solution polarization level for ZA of $22 \pm 2\%$ ($n = 3$, see Methods section) with relatively long longitudinal relaxation times (T_1) at 3 T for both ZA_1 ($T_1 = 43 \pm 3$ s, $n = 3$) and ZA_5 ($T_1 = 51 \pm 4$ s, $n = 3$) in 80 mM Tris buffer in H_2O (Fig. 4.11). For back-calculation of pH from changes in chemical shift of ZA, we determined a calibration curve by measuring the hyperpolarized chemical shifts of both ZA_1 , ZA_5 and urea for pH values covering the physiologically and pathologically relevant pH range (Fig. 4.1). The determined $\text{p}K_{\text{a}2} = 6.90$ from the hyperpolarized ^{13}C -NMR data agrees well with data from literature [112].

4.2.2 *In vitro* pH measurement

We then performed *in vitro* pH imaging measurements in buffer and blood phantoms. Due to its robustness towards gradient errors, motion and flow artefacts, as

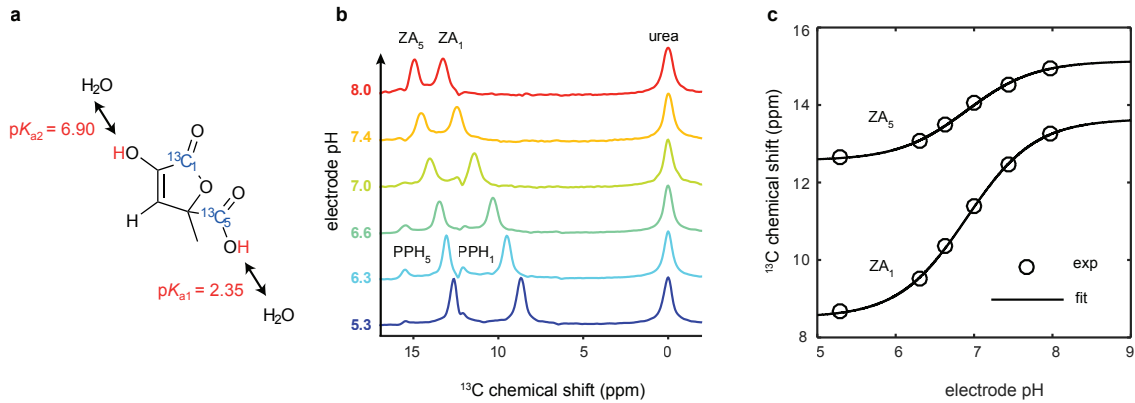


Figure 4.1: Mechanism and calibration of the pH dependency of ZA at 7 T.

(a) ZA bears two exchangeable protons, one in a carboxy group with an acid dissociation constant $\text{p}K_{\text{a}1} = 2.35$ and a second one in an enolic hydroxy group with $\text{p}K_{\text{a}2} = 6.90$. (b) Spectra of hyperpolarized ZA and urea in buffer phantoms at different pH values. The pH sensitivity in the physiological range is due to $\text{p}K_{\text{a}2}$ and results in a change of the chemical shifts of the two ^{13}C -labeled carbon positions with respect to the pH-insensitive ^{13}C -urea peak as a function of pH. Additional peaks of a decay product of ZA, parapyruvate hydrate (PPH), can be identified. (c) The fit of a scaled logistic function to the data from **b** results in a calibration curve with a direct dependence between chemical shift and pH.

well as off-resonance effects, we used a free induction decay chemical shift imaging (FIDCSI) sequence leading to a full spectrum for each voxel [40]. Back-calculation of pH on a voxel-by-voxel basis from the acquired spectra results in a spatially localized pH map for a buffer (Fig. 4.2a) and a blood phantom (Fig. 4.2b) of compartments pre-adjusted to different pH values. Experiments with varying buffer compositions and conditions demonstrated the sensor's robustness. A linear fit shows excellent correlation ($R^2 = 0.99$) between the ^{13}C biosensor pH values determined from hyperpolarized buffer and blood phantom experiments and subsequent electrode pH measurements (Fig. 4.2c). Notably, ZA's pH sensor ability is not influenced by the addition of calcium ions.

4.2.3 *In vivo* probe characterization

The toxicity of injected probe molecules often limits their use *in vivo*. HeLa cells showed no reduction in cell viability when exposed to ZA concentrations relevant during an *in vivo* experiment. Non-toxicity was further substantiated by dose escalation experiments in three rats (Fig. 4.12 and Fig. 4.13) and a toxicopathological study (Methods section, Table 4.1, Fig. 4.14 and Fig. 4.15).

Since concentration of ZA and local temperature could vary substantially *in vivo* upon injection, the influence of these two parameters on a pH determination needs

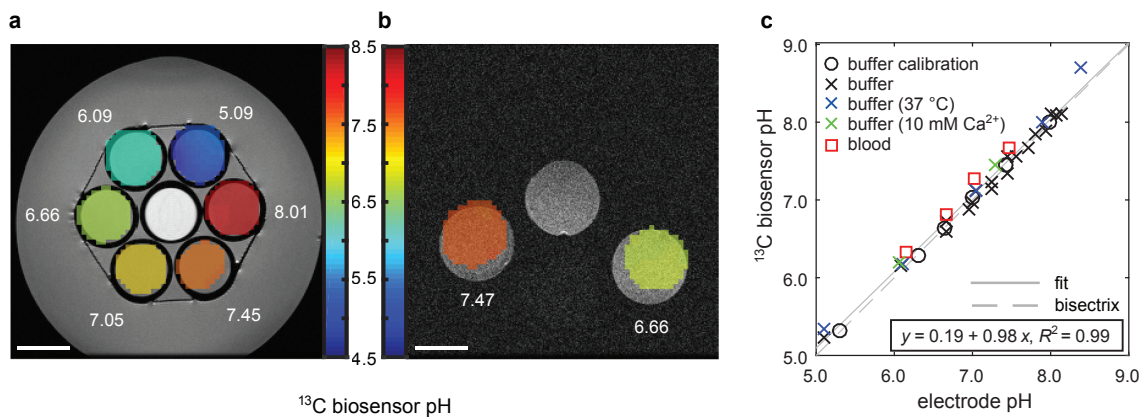


Figure 4.2: Validation of ZA as a pH sensor in hyperpolarized *in vitro* measurements in buffer and blood at 7 T. (a,b) Hyperpolarized ^{13}C biosensor pH maps (colored) in an axial slice overlaid on proton images (grayscale). The electrode pH values are shown in white. ZA and urea were simultaneously hyperpolarized and injected into (a) six buffer phantoms and (b) two blood phantoms prepared at different pH values. In both a,b, a calibration phantom (see Methods section) was present. ^{13}C biosensor pH map windows are based on a signal-level threshold. (c) ^{13}C biosensor pH and electrode pH correlate well for experiments in different buffers (black circles and crosses), at elevated temperature (37 °C, blue crosses), at a 10 mM Ca^{2+} concentration (green crosses) and in blood (red squares). We determined a root mean square error of the fitting residuals (RMSE) of 0.10 pH units from the set of all *in vitro* experiments shown in c. Scale bars, 1 cm.

to be known for a robust measurement. We thus recorded ^{13}C chemical shifts of ZA and urea as a function of pH at three different concentrations of ZA. No differences between the three series of measurements could be detected, making ZA a concentration-independent pH sensor within the experimentally relevant concentration range (Fig. 4.16a). We then tested for a temperature dependence of the relevant $\text{p}K_{\text{a}2}$ by regular acid-base titration of ZA solutions at different temperatures. Diprotic acid titration curves revealed a very weak temperature dependence of $\Delta\text{p}K_{\text{a}2}/\Delta\vartheta = -0.015 \pm 0.005 \text{ pH}/^\circ\text{C}$ (Fig. 4.16b). Hence, ZA's pH sensitivity is a concentration and temperature independent effect within biologically relevant conditions. Furthermore, we showed that variations in ionic strength (Fig. 4.17) and protein concentration (Fig. 4.18) are not substantially influencing ZA's pH determination accuracy.

The acquisition of spatially localized pH maps *in vivo* requires a sufficiently long signal lifetime. Longitudinal relaxation times were determined *in vivo* by performing slice selective time-resolved spectroscopy, resulting in an apparent T_1 of $17 \pm 2 \text{ s}$ (mean \pm s.d.; $n = 6$, three independent slices per two animals) for ZA_1 and $16 \pm 1 \text{ s}$ (mean \pm s.d.; $n = 6$) for ZA_5 at 7 T (Fig. 4.19). Notably, the apparent T_1 of ZA is slightly longer than the apparent T_1 of urea ($13 \pm 2 \text{ s}$, mean \pm s.d., $n = 6$, $B_0 = 7 \text{ T}$), placing ZA on the same level with a well-established hyperpolarized compound.

4.2.4 *In vivo* pH measurement in rat bladder

First, we tested whether a pH measurement using ZA gives reliable results *in vivo* where an independent validation of the pH is possible. To this end, we injected simultaneously hyperpolarized ZA and urea via a catheter directly into the filled rat bladder. The source of the hyperpolarized signal of both ZA and urea (Fig. 4.3a, b) clearly stemmed from the bladder. From the localized spectroscopic imaging data (Fig. 4.3d), a pH map (Fig. 4.3c) was calculated, resulting in a ^{13}C biosensor pH of 6.48 ± 0.02 ($n = 9$ pixels, mean \pm s.d.), in good agreement with the pH of 6.55 ± 0.01 determined via pH electrode in the urine, sampled from the bladder directly after the MR measurement. All ^{13}C images in animals were acquired with a nominal spatial resolution of $3.75 \times 3.75 \times 5 \text{ mm}^3$.

4.2.5 *In vivo* pH measurement in rat kidneys

Next, a tail vein injection of hyperpolarized ZA and urea into four healthy rats was performed, subsequently imaging a slice containing the kidneys. Starting the imaging sequence 10 s after completion of the injection, the strongest signal from hyperpolarized ZA and urea originated from the kidneys with a noticeable amount detected in the blood pool (Fig. 4.4a, b). We discovered up to three pairs of ZA peaks within the same voxel (Fig. 4.4e) forming three pH clusters with a pH of 7.40 ± 0.01 , 6.94 ± 0.05 and 6.55 ± 0.03 (Fig. 4.4d,f, $n = 4$ rats, mean \pm s.d., representative fitting residuals shown in Fig. 4.20). Based on their consistent pH values with data

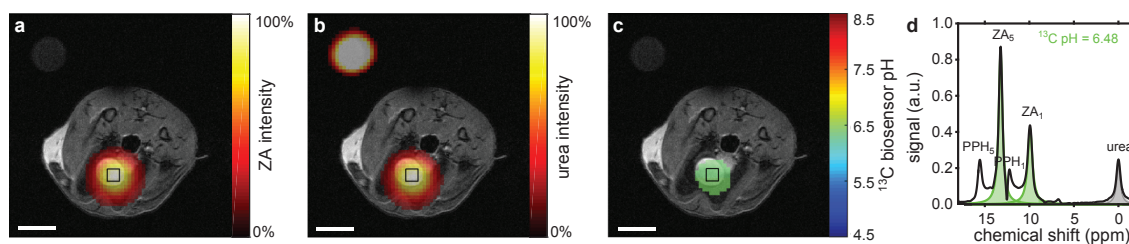


Figure 4.3: Hyperpolarized ZA *in vivo* pH measurement in the rat bladder at 7 T. (a–c) Hyperpolarized ^{13}C measurements (colored) in an axial slice overlaid on anatomical proton images (grayscale). A calibration phantom containing ^{13}C -urea is visible in the upper left corner of the image. The signal stemming from the two simultaneously hyperpolarized and injected substances (a) ZA and (b) urea is well localized to the bladder. (c) The pH map calculated from changes in chemical shift of the ^{13}C pH biosensor shows an acidic pH in the bladder of 6.48 ± 0.02 ($n = 9$ pixels, mean \pm s.d.). (d) The spectrum from a voxel at nominal resolution (black box) in the bladder shows ZA (fitted, green), urea (fitted, grey) and a noticeable amount of a decay product of ZA, PPH (not fitted, white). Scale bars, 1 cm.

from literature [133], these pH clusters were tentatively attributed to the cortex, medulla and calyx/ureter, respectively, reflecting the transition effects of the blood pH before, during and after processing, filtering and renal metabolism. Weighing the pH from the three compartments by their respective amplitudes, a mean pH map was calculated (Fig. 4.4c). The extravasation of ZA and its accumulation in renal tissue in both cortex and medulla was confirmed by matrix-assisted laser desorption/ionization mass spectrometry imaging (MALDI-MSI, Fig. 4.21).

4.2.6 *In vivo* pH measurement in rat tumors

Finally, we imaged the pH within MAT B III adenocarcinoma in five rats. Starting the measurement 10 s after the end of the intravenous injection of the hyperpolarized compounds, the strong ZA and urea signals showed a well-perfused subcutaneous tumor (Fig. 4.5a,b, additional proton images shown in Fig. 4.22). We detected an acidic tumor compartment of $\text{pH } 6.94 \pm 0.12$ ($n = 5$ rats, mean \pm s.d.) tentatively assigned to the extravascular (interstitial/extracellular) compartment of the tumor. The signal stemming from the other tumor compartment of $\text{pH } 7.40 \pm 0.05$ ($n = 5$ rats, mean \pm s.d.) was tentatively assigned to the vasculature of the tumor. Furthermore, we observed a $\text{pH } 7.39 \pm 0.05$ ($n = 5$ rats, mean \pm s.d.) in blood near the vena cava (Fig. 4.5c–e). These measured tumor pH values were compared to three other independent interstitial/extracellular pH measurement methods in MAT B III tumor bearing rats ($n = 4$ rats, mean \pm s.d.): First, the extracellular ^{31}P pH-probe 3-aminopropylphosphonate (3-APP) [54, 126] showed an extracellular pH of 7.11 ± 0.04 *in vivo*; second, the pH determined using a needle-type optical sensor was 6.84 ± 0.13 *in vivo*; third, *ex vivo* measurement of tumor tissue using a standard pH microelectrode gave a pH of 6.82 ± 0.12 (Fig. 4.5e). These three pH values agree

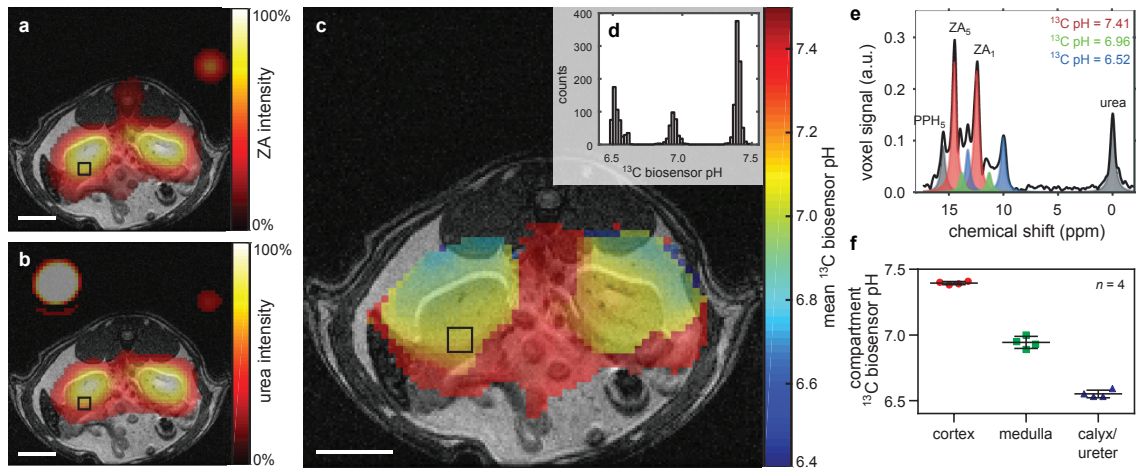


Figure 4.4: Hyperpolarized ZA *in vivo* pH measurements show three pH compartments in rat kidneys at 7 T. Representative kidney data from a hyperpolarized ^{13}C measurement (colored) in an axial slice overlaid on anatomical proton images (grayscale). A calibration phantom containing ^{13}C -urea and the catheter used for injection are visible. The two simultaneously hyperpolarized and injected substances (a) ZA and (b) urea show high signal intensities in both kidneys of a healthy rat. (c) The mean pH map shows lower pH values in the kidneys compared to the surrounding tissue. (e) A voxel can contain up to three pairs of ZA peaks (red, green, blue) and a noticeable amount of PPH. The pH values group into three clusters (d, shown for one representative animal), consistently demonstrated in four animals (f, individual datapoints and mean \pm s.d.). For all ^{13}C images, intensity windows are based on sufficiently high signal levels for either (intensity images) or both (pH images) ZA and urea. Scale bars, 1 cm.

well with the value determined for the extravascular (extracellular/interstitial) pH compartment using ZA (no significant difference, $p > 0.05$, Mann-Whitney-Wilcoxon test) suggesting that ZA measures and distinguishes extravascular (interstitial/extracellular) pH and intravascular pH.

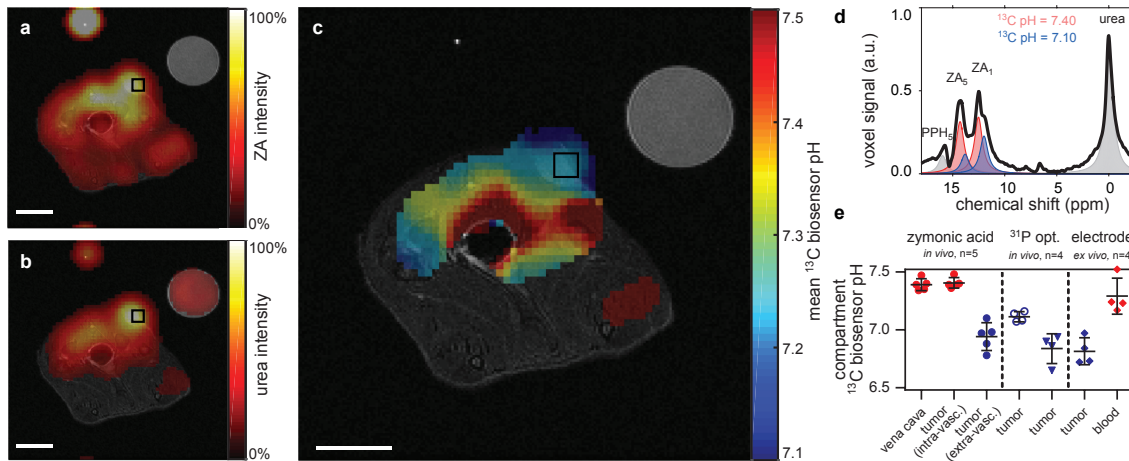


Figure 4.5: Hyperpolarized ZA *in vivo* pH measurements show an acidic tumor pH at 7 T. Representative tumor data from a hyperpolarized ^{13}C measurement (colored) in an axial slice overlaid on anatomical proton images (grayscale). A calibration phantom containing ^{13}C -urea and the catheter used for injection are visible. Both (a) ZA and (b) urea accumulate in the MAT B III tumor. (c) The mean pH map shows a lower pH value in the tumor compared to the surrounding tissue. For all ^{13}C images, intensity windows are based on sufficiently high signal levels for either (intensity images) or both (pH images) ZA and urea. Spectra from tumor voxels (d, shown for one representative animal) are best fitted with two pairs of ZA peaks (red, blue) and consistently show different pH values in the tumor in comparison to the vena cava, demonstrated in five animals (e, individual datapoints and mean \pm s.d.) and compared with three other interstitial/extracellular pH measurements in four animals, namely ^{31}P MRS *in vivo* using 3-APP, a needle-type optical sensor *in vivo* and an *ex vivo* tissue electrode pH measurement. Scale bars, 1 cm.

4.3 Discussion

Despite the relevance of extracellular pH for the characterization of human pathologies, there is currently no method to non-invasively map the spatial distribution of pH by clinical imaging methods, creating a pressing need for the development of pH imaging probes with potential for clinical translation. Here, we present a novel pH imaging approach using hyperpolarized ZA as an MRI pH sensor. Our results showed that this pH imaging method is independent of concentration, temperature, ionic strength and protein concentration. Importantly, ZA's pH sensitivity arises from protonation and deprotonation in proximity to its ^{13}C -labeled sites, which is fast on the NMR timescale (10^3 – 10^4 Hz under physiological conditions [92]) and

allows an assessment of pH whenever the agent reaches its target. We demonstrated that *in vivo* pH maps within rat kidneys and adenocarcinomas can reliably be determined, and in both cases two to three pH compartments within one imaging voxel can be separated, which is a unique feature of ZA. Important criteria for the evaluation of a novel pH probe are the achievable spatial and temporal resolution, its sensitivity, accuracy to determine pH, toxicity, its potential to disturb the acid-base balance during the measurement, and knowledge about its presence in the vascular, extravascular or intracellular compartments or a combination of the aforementioned.

In comparison to hyperpolarized ^{13}C -labeled bicarbonate [50], which has been proposed as a probe for clinical pH imaging and which currently is the most prominent among the hyperpolarized pH probes, ZA-based pH imaging offers several advantages: First, ZA has a relatively long signal lifetime with an apparent T_1 of $\sim 17\text{ s}$ at 7 T *in vivo*, whereas bicarbonate has a shorter apparent T_1 , which is $\sim 10\text{ s}$ *in vivo* at both 3 T and 9.4 T [50, 143]; second, ZA is highly soluble and does not need enzymatic conversion to become an active pH probe, whereas bicarbonate exhibits a relatively small equilibrium CO_2 signal ($\sim 6\%$ of HCO_3^- at pH 7.4) and limited solubility at physiological pH; third, ZA is localized in the extracellular space and slowly excreted through the kidneys and decomposes into endogenous substrates, whereas CO_2 through respiration and diffusion across cell membranes is not clearly restricted to the extracellular space; fourth, ZA relies on the determination of pH through the measurement of chemical shift displacements, whereas for bicarbonate pH mapping, there is a need for ratiometric analysis of signal amplitudes which is difficult at a low signal-to-noise-ratio (SNR); fifth, pH measurements using ZA does not involve any enzymes in contrast to bicarbonate pH imaging, where the enzyme concentration (that is, carbonic anhydrase) influences the speed at which pH can be measured.

The pH determination accuracy of ZA was found to be high enough to detect relevant pathological pH changes *in vivo*. The pH dispersion of the ^{13}C chemical shift of ZA_1 in the physiological pH range is $\sim 3.0\text{ ppm per pH}$. This corresponds to a frequency shift of 96 Hz per pH at a clinical field strength of 3 T. Assuming that peaks can be distinguished at 20 % of their linewidth apart, which we measured to be on the order of 30–50 Hz *in vivo*, this results in a pH resolution of $\sim 0.1\text{ pH units}$. Similar accuracies have been reported for other chemical shift-based hyperpolarized probes like $[^{13}\text{C},^{15}\text{N}]\text{ACES}$, although this probe has so far only been proven to work *in vitro* [44]. A larger pH dispersion of the ^{13}C chemical shifts of a probe would theoretically allow for a higher accuracy of the pH measurement but comes with the drawback that RF excitation pulses then need to cover a larger bandwidth, which is challenging for the RF pulse design. At the same time, chemical shift displacement artifacts impede accurate slice selective excitation of all pH-sensitive resonances if resonances are spread out further. In addition, the chemical shift imaging (CSI) readout would need to cover a larger frequency bandwidth resulting in increased noise from the receiver. These limitations could pose a challenge for the recently introduced hyperpolarized ^{15}N -labeled probes based on pyridine and histidine derivatives that have been reported to show pH-dependent chemical shifts of more than 80 ppm [74, 148]. Also, the applicability of these probes still has to be proven under *in vivo* conditions.

Although our fitting residuals shown in Fig. 4.20 indicate that fitting ZA in multiple tissue compartments in kidney and tumor is reasonable, complete separation and fitting of extravascular and intravascular pH compartments remains challenging for the case of small pH differences between individual compartments.

A limitation for most hyperpolarized ^{13}C imaging methods is the low spatial resolution compared to other imaging methods. Spectral bleeding artefacts, where high-intensity spectral peaks are reproduced in neighboring voxels, can lead to a further reduction in the resolution. Chemical exchange saturation transfer (CEST) imaging methods have a better spatial resolution in the μm – mm range with good specificity but poor sensitivity [26]. The FIDCSI sequence used in this work (see Methods section) has a slice thickness of 5 mm and a nominal in-plane resolution of 3.75 mm. Zero filling by a factor of four results in an apparent in-plane resolution of 0.94 mm. Taking into account the shape of the point spread function of the circular sampling scheme, the in-plane resolution is affected by a factor of ~ 1.40 resulting in a real in-plane resolution of 5.25 mm and an apparent in-plane resolution of 1.31 mm. The spatial resolution of hyperpolarized ^{13}C pH imaging could be further improved by implementing alternative acquisition schemes such as echo planar spectroscopic imaging (EPSI) or using cryogenically cooled receive coils such that sub-millimeter resolution for pH imaging seems possible. EPSI increases the gradient hardware and magnetic field homogeneity requirements but reduces the time needed to acquire an image, thereby improving SNR and real resolution [40].

We have established non-toxicity of our agent in a toxicopathological study and with dose escalation experiments at doses up to five times of the injected dose for the *in vivo* pH measurement. This might facilitate clinical translation compared to other pH imaging agents, where toxic effects can arise from Gd^{3+} -chelates in patients with renal insufficiency [106] or from preparations of hyperpolarized cesium bicarbonate, where toxic cesium [108] is used to increase the bicarbonate concentration.

The injected substances ZA and urea could potentially act as buffering agents and influence the pH value they are measuring. With a $\text{p}K_{\text{a}} \approx 0.18$ of its conjugated acid in water, urea cannot act as a buffer in the physiological pH range and thus does not influence the measured pH. For all pH probes for which the pH determination is based on a protonation/deprotonation mechanism within the pH range of interest, the pH measurement is effectively based on the buffering functionality of the pH probe. ZA with a $\text{p}K_{\text{a}}$ of 6.90 is injected at a concentration of 50 mM and is diluted to a concentration of about 5 mM if evenly distributed in the blood. The actual bicarbonate concentration in the blood at full oxygen saturation and 37°C is 21–26 mM, with the $\text{CO}_2/\text{HCO}_3^-$ equilibrium acting as the main natural buffer component *in human*. When, as in the current study, the injection of ZA results in low mM concentrations of ZA in the blood, one should not expect a significant alteration in pH even if much larger relative doses [49] are injected *in vivo*.

Evidence suggests that ZA extravasates and predominantly stays in the extracellular/interstitial space, thus measuring extracellular pH. Extravasation of ZA to renal tissue is confirmed by MALDI-MSI in kidney slices (Fig. 4.21). Compari-

son of the pH measured using ZA in MAT B III tumor bearing rats with the pH values determined by three other interstitial/extracellular pH measurements (^{31}P MRS, needle-type optical sensor, electrode) showed good agreement between these methods, suggesting that ZA can measure and distinguish both extravascular (interstitial/extracellular) and intravascular pH (Fig. 4.5e). Furthermore, the fact that ZA, instead of using a ratiometric method, uses differences in chemical shifts to determine the pH, allows for the detection of several pH compartments within the same voxel (Fig. 4.4e). If an intracellular pH compartment with a pH predominantly around 7.4 would provide a significant contribution to the overall signal, an additional pair of ZA peaks should be observed. Fig. 4.6 shows a cell experiment with just one pair of ZA peaks belonging to a compartment with a ^{13}C biosensor pH that correlates well with the pH measured using a conventional pH electrode measuring the extracellular pH. Since no second pair of ZA peaks is visible in this experiment, no significant amount of ZA has entered the cell suggesting that ZA stays mainly extracellular.

ZA can be used for pH imaging either with simultaneously hyperpolarized urea as a pH-independent chemical shift reference as demonstrated in this work or without urea in order to decrease the number of substances required to be injected *in vivo*. When ZA is used as a pH imaging sensor without urea, the difference in chemical shift as a function of pH between the two ^{13}C positions within ZA can be used to back calculate the pH (Fig. 4.10). Within the range of pH 6–8, both methods give nearly identical results, but the dynamic range of potential pH values to be measured is larger when the urea peak is included in the pH evaluation, since the pH determination precision is higher at the limit of the sensor’s sensitivity when using urea as a reference (RMSE \approx 0.09 pH units compared to RMSE \approx 0.019 pH units between the ^{13}C biosensor pH measurement and the electrode pH measurement).

As for other currently known ^{13}C -labeled probes, a major limitation of using hyperpolarized ZA for *in vivo* applications is its polarization lifetime. This could be prolonged by performing the pH measurements at a reduced clinical field strength and by deuteration. For hyperpolarized ^{13}C experiments, higher magnetic fields result in a larger chemical shift separation between the peaks of interest, allowing for easier discrimination. However, higher magnetic fields lead to shorter T_1 relaxation times, reducing the time available for hyperpolarized measurements, and in contrast to conventional experiments, higher magnetic fields do not result in larger signals. Thus, it would be best to perform the measurements at an intermediate and well-shimmed magnetic field, for example at clinically widely available 3 T scanners, to balance the chemical shift separation and T_1 relaxation times. In addition, dipolar effects between the four protons and the two ^{13}C -labeled carbons reduce the T_1 relaxation time. Replacing both the single proton and the three protons in the methyl group of ZA with deuterium would lengthen the T_1 s of ZA_1 and ZA_5 . Sensitivity could be improved further by increasing the polarization level.

ZA represents a pH imaging candidate for clinical translation. The demonstrated robustness of using ZA for extracellular pH imaging, its non-toxicity, and the diagnostic value of imaging pH in a broad pathological context, such as in ischemia, infection, inflammation and cancer, render this new pH imaging technique valuable. Changes in metabolism and extracellular pH have been shown to be an indicator of early treatment response in tumors preceding morphologic transformations [35], suggesting that ZA could be used to detect pH changes as an early biomarker of successful therapy.

4.4 Methods

Chemicals

^{13}C and ^2H enriched chemicals were either purchased from Sigma-Aldrich (USA) or Euriso-Top (France). Unless stated differently, all other chemicals were purchased from Sigma-Aldrich (USA).

4.4.1 Synthesis of selectively ^{13}C -labeled ZA

Equal amounts (v/v) of $[1-^{13}\text{C}]$ pyruvic acid and 37% hydrochloric acid were incubated for 20–30 days [76]. Optionally, 1 eq. $[1-^{13}\text{C}]$ pyruvic acid was incubated with 0.5 eq. aqueous zinc acetate solution for 1 h yielding insoluble $[1,5-^{13}\text{C}_2]$ zinc PP, which was dissolved with 37% hydrochloric acid. After the removal of volatiles using a rotatory evaporator, the residual yellow viscous solution was dissolved in a small amount of water containing 0.1% trifluoroacetic acid. The reaction product was purified by a reversed phase high pressure liquid chromatography using a Waters XBridge Prep C18 column (linear gradient of 2–20% acetonitrile, buffer A: 0.1% TFA in water, buffer B: 0.1% TFA in acetonitrile) and freeze-dried *in vacuo* (alpha 2–4 LD plus, Christ, UK). The experimental yield of ZA was $\sim 40\%$. ZA can be stored lyophilized and is stable in dimethylsulphoxide.

4.4.2 Cell experiments

MCF-7 cells used in this study were originally provided by Guy Leclercq at the Institut Jules Bordet, Centre des Tumeurs de l'Université Libre de Bruxelles, Belgium, to Angela M. Otto, in whose lab they have since then been cultured and tested as free of mycoplasma. The identity of the cells was confirmed by the Leibniz-Institut Deutsche Sammlung von Mikroorganismen und Zellkulturen (DSMZ), Germany in 2015. MCF-7 tumor cells were maintained as a monolayer culture in Dulbecco's modified Eagle's medium (DMEM) supplemented with 5% fetal calf serum (FCS). For spheroid preparation, cells were gently stirred in spinner flasks for up to 6 days

in a CO₂ incubator at 37 °C and transferred to DMEM with 5 % FCS containing NaHCO₃ (0.37 g L⁻¹) and 20 mM 2-[4-(2-hydroxyethyl)piperazin-1-yl]ethanesulfonic acid (HEPES) at pH 7.4. After gradually inducing cell membrane permeabilization, and thus cell death and medium acidification by incubation with 0.015 % Triton X-100, 0.2 mL of a 10 mM hyperpolarized [1-¹³C]pyruvic acid solution containing traces of hyperpolarized ZA were added to 0.8 mL of a cell spheroid suspension containing 40 × 10⁶ MCF-7 cells in assay medium. ¹³C-NMR spectra were acquired at 14.1 T (Avance III, Bruker BioSpin, Germany). The ¹³C biosensor pH was calculated from the difference in chemical shift of the two peaks assigned to the ¹³C-labeled positions (ZA₅ and ZA₁) in ZA using the model shown in Fig. 4.1c and compared to the pH determined after the NMR experiment with a standard pH electrode (pH meter: ProLab 4000, SI Analytics, pH electrode: N6000A, temperature sensor Pt 1000: W5790NN). The fraction of dead cells [142] was determined by centrifugation of the spheroid suspension at 150 g before washing the pellet twice with phosphate buffered saline (PBS) and incubating an aliquot of spheroids at room temperature for 30 min with a solution containing 2 μM membrane-permeant ethidium bromide. After another centrifugation, spheroids were fixed in 3.7 % formaldehyde-PBS solution, analyzed by fluorescence microscopy (Axiovert 200, Zeiss, Germany) using fluorescein isothiocyanate and rhodamine filters to discriminate between general green autofluorescence and red staining of dead cells. MTT assays to assess cellular metabolic activity were performed by incubating 5 × 10³ HeLa cells, each suspended in 100 μL cell culture medium at pH 8.0, for 24 h with ZA at concentrations between 0.4 and 12.5 mM.

4.4.3 Characterization of ZA

The mass of the synthesized substance was determined by an HR-MS-spectrum using a Thermo Finnigan LTQ-FT. A MS/MS-spectrum was recorded by CID-fragmentation on a Thermo Finnigan LCQ-Fleet (Fig. 4.7). ¹H and ¹³C chemical shifts and coupling networks were extracted from NMR spectra of unlabeled and ¹³C fully labeled ZA and its decay products in H₂O at 14.1 T (Fig. 4.6). ZA concentration-dependent ¹³C-NMR acid-base titrations were performed with ZA at 37 °C in 1 M phosphate buffer at 14.1 T, adjusting the pH in random order using 1 M HCl and 1 M NaOH. Electrode pH was reported as the mean of two measurements determined directly before and after the NMR experiment with a standard pH electrode. Regular acid-base titrations of 25 mM ZA in 1 M KCl in H₂O were performed using 1 M KOH at different temperatures. Each full titration was performed within 22 ± 1 min and a model titration curve for a diprotic acid was fitted to each titration experiment separately to extract the relevant acid dissociation constant pK_{a2} as a function of temperature. The temperature dependence of the acid dissociation constant ΔpK_{a2}/Δθ was then determined from a linear fit to the extracted data points. Hyperpolarized ¹³C-NMR acid-base titrations were performed with a solution of 25 mM ZA in presence of 10 mM Ca²⁺ at 1 T and 27 °C. The detected pH-dependent hyperpolarized ¹³C chemical shifts were compared to regular ¹³C-NMR acid-base titrations at 37 °C in 1 M phosphate buffer at 14 T. Stability

measurements were performed by acquiring ^1H spectra at 1 T and 27°C over 20 h, each spectrum averaged over 60 scans with a repetition time of 10 s.

4.4.4 Hyperpolarization with dissolution DNP

A solution of 50 μL of dry dimethyl sulphoxide (DMSO) with 4 M ZA, 15 mM of free radical (OX063, Oxford Instruments) and 5 mM of gadolinium chelate (Dotarem, Guerbet) was added to a standard DNP sample cup and frozen in liquid nitrogen. An aliquot of 30 μL 10 M ^{13}C -urea containing 30 mM of free radical and 1.5 mM of gadolinium chelate was added on top of the frozen ZA layer and frozen in liquid nitrogen as well. The sample cup was placed in a DNP polarizer (Hypersense, Oxford Instruments, UK) and polarization was carried out using a microwave source at 94.155 GHz for 1.5 h. The sample was dissolved in a pressurized (10 bar) and heated (180°C) solution of 4 mL D_2O containing 0.1 g L^{-1} sodium diaminoethanetetraacetic acid (Na_2EDTA), which was neutralized with NaOH to a final pH of ~ 7.4 . The final concentrations of ZA and ^{13}C -urea were ~ 50 mM and 75 mM. The final temperature of the solution was 37°C . T_1 measurements of natural abundance ZA in 80 mM Tris buffer in H_2O were performed on a clinical Biograph mMR MR-PET (Siemens, Germany, $B_0 = 3\text{ T}$) using a pulse length of 0.2 ms, a flip angle of 15° , a spectral bandwidth of 2500 Hz and a repetition time of 5 s. Carbon center frequency and flip angle were determined using an 8 M ^{13}C -urea phantom with 5 mM Dotarem (Guerbet, France) and 0.1 % sodium azide. T_1 decay curves were flip angle corrected and fitted by a three parameter mono-exponential decay curve. The solution polarization level was determined using a Bruker Minispec mq40 NMR analyzer (Bruker, Germany, $B_0 = 1\text{ T}$). First, a hyperpolarized T_1 decay curve was acquired, flip angle corrected and the signal intensity was extrapolated to the time of dissolution. The thermal signal was measured with a Carr-Purcell-Meiboom-Gill sequence (echo time: 2 ms, acquisition time: 0.25 ms, repetition time: 300 s, number of echoes: 600, number of scans: 10).

4.4.5 Buffer and blood phantom preparation for imaging experiments

Buffer phantoms were either prepared using a 200 mM disodium phosphate/sodium phosphate buffer, a 80 mM Tris buffer or a 100 mM citric acid/200 mM disodium phosphate buffer. They were placed into a water bath for improved shimming and reduced susceptibility artefacts. For experiments at 37°C , an air heating unit with feedback control (SA Instruments, USA) was used to stabilize the phantoms' temperature. An aliquot of 0.2 mL of hyperpolarized ZA and urea solution was added to each 2.0 mL buffer phantom using a multistep pipette. Phantoms were closed and inverted three times for thorough mixing before placing them into the MR scanner. Blood phantoms were prepared with human blood withdrawn into collection tubes containing EDTA as anticoagulant (S-Monovette, EDTA KE, Sarstedt, Germany)

to maintain blood in its fluid state and the blood pH was adjusted using 1 M HCl. Phantoms were placed inside the MR scanner with catheters inserted for injection of 0.2 mL of hyperpolarized ZA and urea solution. Direct and rapid injection into each 1.8 mL blood phantom prevented fast T_1 relaxation of ZA in blood at Earth's magnetic field [103]. A thorough mixing of the solution was achieved by shaking the entire phantom set-up. For both buffer and blood phantom experiments, an additional ^{13}C -urea phantom doped with a gadolinium chelate (Dotarem, Guerbet, France) was placed inside the field of view for ^{13}C flip angle and frequency calibration. The pH of each phantom was measured by a standard pH electrode after the MR experiment.

4.4.6 Spectroscopy and imaging procedure

All phantom and ^{13}C *in vivo* imaging experiments were performed on a 7 T small animal MR scanner (GE/Agilent), which was migrated to a Bruker BioSpec console before ^{31}P experiments were performed. A 72 mm dual tuned $^1\text{H}/^{13}\text{C}$ birdcage coil was used for signal transmission in combination with a two channel flexible coil ^{13}C receive array (Rapid Biomedical, Germany). Proton images were recorded with a fast spin echo (FSE) sequence, slice thickness 1 mm, field of view 6 cm, image matrix 256×256 , repetition time 2.6 s, effective echo time 20 ms, number of averages 2. *In vivo* T_1 relaxation was measured using slice selective excitation with 10 mm slice thickness, 6 cm field of view, 10° flip angle, 3 s repetition time, 64 excitations and total scan time 192 s. The acquired free induction decays (FIDs) were zero filled, line-broadened by an exponential filter of 20 Hz and Fourier transformed using Mnova (Mestrelab Research, Spain). A three-parameter mono-exponential decay curve was fitted in Matlab (MathWorks, USA). Imaging experiments were performed using a free induction decay chemical shift imaging (FIDCSI) sequence and reconstruction in Matlab (MathWorks, USA) described elsewhere [40], with k-space being sampled in centric order from the center on outwards. Imaging parameters were: $141 \text{ T m}^{-1} \text{ s}^{-1}$ maximum slew rate, 38 mT m^{-1} maximum gradient amplitude, 5 kHz spectral bandwidth, 512 points sampled, 9.8 Hz spectral resolution, 16×16 nominal matrix size, 5 mm slice thickness, 6 cm field of view, 4° flip angle, 118 ms repetition time, 208 excitations, total scan time 25 s. A 10 Hz Gaussian filter was applied along the readout dimension and the data were zero-filled by a factor of four in the two spatial as well as in the spectral dimension before fast Fourier transforms (FFTs) were applied along all three dimensions. For all ^{13}C images, intensity windows are based on sufficiently high signal levels for either (intensity images) or both (pH images) ZA and urea.

4.4.7 Animal handling and tumor implantation

Animal experiments were approved by the local governmental committee for animal protection and welfare (Tierschutzbehörde, Regierung von Oberbayern) and performed in accordance with the institutional guidelines of the Technische Universität

München for the care and use of animals. Animals were anesthetized with 3–5% isoflurane inhalation gas. Catheters were placed before the animals were put into the MR scanner and tail vein injections were performed at a dose of 5 mL kg^{-1} and a rate of 0.17 mL s^{-1} . MR exams were started 10 s after the end of the injection. To maintain constant body temperature, animals were placed on an electric heating pad during the dose escalation study, and on a water heated pad during MR exams. In the dose escalation study, heart rate and breathing rate (ECG Trigger Unit, Rapid Biomedical, Germany), as well as blood oxygenation (PalmSAT 2500A VET Pulsoximeter, Nonin, USA) were monitored. The dose escalation study was carried out with three male rats (~ 12 weeks, Lewis, Charles River, average weight $319 \pm 1 \text{ g}$), the *in vivo* T_1 experiments with two male rats (~ 8 weeks, Lewis, Charles River, average weight $217 \pm 1 \text{ g}$), the bladder experiment was carried out with a female rat (~ 8 weeks, Lewis, Charles River, weight 230 g), the kidney experiment with four male rats (~ 14 weeks, Buffalo, Charles River, average weight $375 \pm 38 \text{ g}$), the tumor experiment with five female rats (~ 6 weeks, Lewis, Charles River, weight $132 \pm 10 \text{ g}$), the MALDI experiment was carried out with a male rat (~ 8 weeks, Wistar, Charles River, weight 300 g), the phosphor and optical pH measurements with four female rats (~ 9 weeks, Fischer 344, Charles River, weight $155 \pm 2 \text{ g}$) and the electrode pH measurements with four female rats (~ 8 weeks, Fischer 344, Charles River, weight $153 \pm 2 \text{ g}$). For the bladder experiment, saline (0.90% w/v of NaCl) was injected subcutaneously 30 min before start of the experiment to guarantee accumulation of urine in the bladder. A catheter for injection of the hyperpolarized substances and for sampling the urine was inserted into the bladder before placing the animal in the MR scanner. Urine pH was measured using a standard pH electrode. Tumor imaging experiments were performed on day 6 after injecting $200 \mu\text{L}$ PBS containing 1×10^6 13762 MAT B III (ATCC, USA) tumor cells subcutaneously into the right flank. Cells were tested for mycoplasma with negative result. Animal MRI experiments were not randomized and not blinded.

4.4.8 Toxicopathological study

To examine potential acute and/or subacute toxicological effects of ZA, we performed a toxicopathological study in Fischer 344 rats obtained from Charles River with 6 weeks of age (average weight $150 \pm 8 \text{ g}$). In total, 14 animals (7 female/7 male) were used. Ten of them received a tail vein injection of 5 mL kg^{-1} with a concentration of 250 mM ZA (five times the dosage used for the imaging experiments), four animals served as controls with a tail vein injection of saline (0.09% w/v of NaCl). Six animals were killed 24 h after injection (acute toxicity), eight animals after 4 weeks (subacute toxicity). The animals were monitored daily, blood collection for hematology and clinical chemistry was performed before and 24 h (acute), 7, 21 and 30 days (subacute) after injection of ZA. The following parameters were measured: hematocrit, hemoglobin, erythrocyte and total leucocyte counts and differentials, urea, creatinine, total protein, aspartate aminotransferase, alkaline phosphatase, creatine kinase, gamma glutamyl transferase, glutamate dehydrogenase, fructosamines, calcium, potassium, magnesium, sodium, inorganic phosphate and

bile salts. After killing, a necropsy was performed, organs (liver, kidneys, spleen, pancreas, intestines, lymph nodes, injection sites, genital tract, lung, heart, skin, skeletal muscle and brain) were fixed in 10 % neutral buffered formalin overnight, dehydrated according to standard protocols, embedded in paraffin, cut in 2 μm thick sections and routinely stained with hematoxylin-eosin (H&E). H&E stainings of all organs were analyzed blinded by an experienced animal pathologist (K.S.) and findings were reported according to the INHAND criteria of the Society of Toxicologic Pathology with respect to the most recent recommendations. Sample size estimates were not performed since both mean and s.d. had to be determined in the experiment for each group.

4.4.9 Back-calculation of pH values and maps

Data analysis was carried out using Matlab (MathWorks, USA) on a voxel-by-voxel basis. Magnitude signals of the two coils were combined assuming equal coil sensitivities [140]. Peaks were detected and fitted to a sum of Lorentzian functions based on their chemical shift with respect to urea (165.5 ppm), which was used as a chemical shift reference set to 0 ppm. During the fitting procedure, peak positions and amplitudes were varied while the peaks' linewidth was determined by the urea peak linewidth (50 ± 13 Hz (mean \pm s.d. from all imaging experiments shown)). PP hydrate peaks were identified according to their expected chemical shifts. For each pair of ZA peaks, a pH value was calculated by a nonlinear least squares algorithm minimizing the residual between the experimental and modeled chemical shift differences of ZA_5 and ZA_1 simultaneously with respect to urea. In case of fast chemical exchange, both chemical shifts ZA_5 and ZA_1 can be described as a function of pH by a scaled logistic function $\text{ZA}_i(\text{pH}) = \text{ZA}_{i,\text{min}} + \delta_i / (1 + 10^{(\text{p}K_a - \text{pH})})$ with the same acid dissociation constant $\text{p}K_a$ for both curves, resulting in five parameters derived simultaneously from the two calibration curves, $\text{ZA}_{5,\text{min}} = 12.57$ ppm, $\text{ZA}_{1,\text{min}} = 8.52$ ppm, $\delta_5 = 2.57$ ppm, $\delta_1 = 5.13$ ppm, and $\text{p}K_a = 6.90$. In case that several pairs of ZA peaks were found within the same voxel, a mean pH map was calculated weighted by the amplitudes of the respective pair of ZA peaks (as seen in the kidneys), in case where ZA_1 overlapped with PPH_1 , so that a discrimination of the two was made impossible, only the shift difference of ZA_5 with respect to urea was used to calculate the mean pH map (as seen in the tumor). pH values were only calculated when required ZA peaks and urea were detected at an SNR of at least 10.

4.4.10 MALDI mass spectrometry imaging

Frozen tissue samples were cryosectioned into 12 μm thick slices and thaw-mounted to pre-cooled (-20°C) conductive indium tin oxide-coated glass slides (Bruker Daltonics, Germany), pre-coated with a 1:1 mixture of poly-L-lysine and 0.1 % Nonidet P-40. Tissue sections were coated with 10 mg mL^{-1} 9-aminoacridine matrix in 70 % methanol using a SunCollect sprayer (Sunchrom, Germany). MALDI-MSI data were

obtained using a Solarix 7 T FT-ICR MS (Bruker Daltonics). Mass spectra were acquired in negative mode for each position using 200 laser shots at a frequency of 500 Hz utilizing continuous accumulation of selected ions to increase signal intensities at m/z 157 with a window of 20 Da. After MALDI-MSI completion, the matrix was removed from slides by 70% ethanol, and tissue sections were stained using H&E.

4.4.11 Phosphor pH reference measurements

3-APP was injected intra-peritoneal (3 mL of 64 mg mL⁻¹ in normal saline, pH adjusted to 7.4 using 10 M NaOH) 40 min before the acquisition of ³¹P spectra (3 s repetition time; 12 kHz spectral width; 4096 acquisition points; 200 averages; 60° flip angle; 10 min acquisition time) using a 2 cm outer diameter double resonance ¹H/³¹P loop coil (Bruker, Germany) placed on the subcutaneous tumors. 3-APP chemical shifts δ in ³¹P spectra were referenced to phosphocreatine (PCr) and the pH was calculated from the Henderson-Hasselbalch equation $\text{pH} = \text{p}K_a - \log_{10}[(\delta - \delta_{\min})/(\delta_{\max} - \delta)]$ with $\text{p}K_a = 6.85$, $\delta_{\max} = 27.01$ ppm, $\delta_{\min} = 23.53$ ppm. [126]

4.4.12 Optical and electrode pH reference measurements

In vivo electrode pH measurements in tumors were performed using needle-type optical pH microsensors (NTH-HP5, PreSens, Germany) with a fiber optic meter (pH-1 micro, PreSens, Germany) and a manual micromanipulator (MM33, PreSens, Germany). Optical fiber electrodes were calibrated using a three-point calibration in blood with pH adjusted using HCl. Optical pH measurements were averaged over three different locations of the tumor performed during a stable signal reading for at least 3 min. For *ex vivo* electrode pH measurements in tumor and blood, blood was withdrawn from the tail vein into collection tubes containing EDTA while tumors were measured directly after extraction from the killed animal.

Data availability

The data supporting the findings of this study are available within the article and its Supplementary Information or from the corresponding author on reasonable request.

4.5 Acknowledgments

We appreciated discussions with Wolfgang Eisenreich, Angela Otto, Raimund Marx and Simone Köcher. We thank Stephan Sieber for access to the preparative HPLC and mass spectrometers, Bernd Reif and his group for access to the lyophilizer and Wolfgang Heydenreuter and Franziska Mandl for their assistance in HPLC usage. Geoffrey Topping, Markus Durst and Ulrich Köllisch helped with regard to the imaging and spectroscopy sequences. Michael Michalik, Miriam Braeuer, Anna Bartels and Concetta Gringeri supported the animal MRI experiments. Olga Seelbach, Marion Mielke and Hilde Kalvelage assisted the histopathological measurements. We are grateful to Bernd Pichler for lending us his $^{31}\text{P}/^1\text{H}$ surface coil. We thank GE Global Research Europe for granting access to the hyperpolarizer. We acknowledge support from EU Grant No. 294582 (MUMI), BMBF (FKZ 13EZ1114), and DFG (SFB 824).

4.6 Author contributions

S.D. and F.S. identified ZA; S.D. and C.H. operated the polarizer and devised the recipe for hyperpolarization of ZA; S.D., C.H. and F.S. conducted the NMR and MRI experiments; C.H. and M.G. synthesized the compounds; M.G. performed the cytotoxicity assay; B.F. prepared the cells and animals; K.S., A.B. and A.W. performed pathological analyses; S.D. evaluated and analyzed the data; S.D., C.H. and F.S. wrote the paper and all authors reviewed the manuscript; A.H., S.J.G., M.S. and F.S. designed the research; and F.S. devised the study.

4.7 Competing interests

S.D., M.G., S.J.G., and F.S. are named as inventors on a patent application concerning the use of ZA as a pH sensor molecule and declare competing financial interests. The remaining authors declare no competing financial interests.

4.8 Appendix A: Supplementary Information

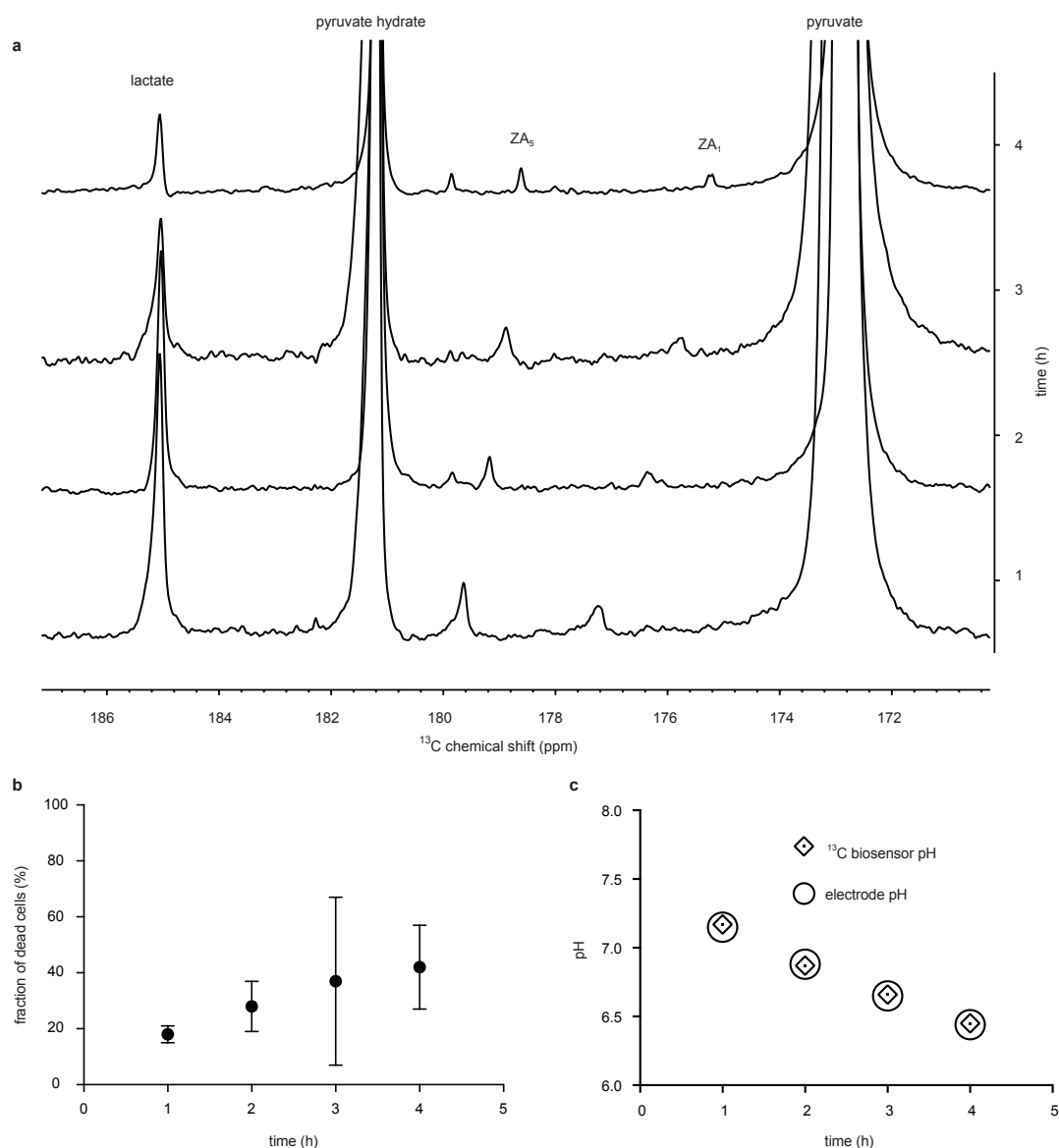
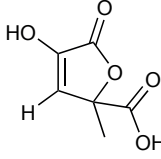
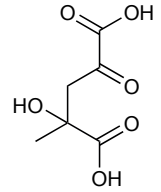


Figure 4.6: pH values determined by the hyperpolarized ^{13}C biosensor correlate with the extracellular pH in a tumor cell suspension at 14.1 T. Measurements in four samples (each at a different time $t = 1, 2, 3, 4$ h) of 2 mM hyperpolarized [$1\text{-}^{13}\text{C}$]pyruvate and 40×10^6 MCF-7 tumor cells being treated with Triton-X100 (at $t = 0$ h). **(a)** Pyruvate in aqueous solution is in equilibrium with pyruvate hydrate and exchanges its ^{13}C label with the lactate pool which in turn is enlarged within tumors by LDH activity. The presence of pyruvate led to trace amounts of detectable hyperpolarized ZA. **(b)** A treatment with Triton X-100 caused the fraction of dead cells to increase over time, determined by cell staining and fluorescence microscopy (see Methods section). **(c)** The progressively increasing number of dead cells and anaerobic conditions over time led to a gradual acidification, with the ^{13}C biosensor pH correlating with the extracellular pH in the medium measured with a standard pH electrode after the NMR experiment.

a	Atom	δ (^1H) (ppm)	δ (^{13}C) (ppm)	J (^1H , ^1H) (Hz)	J (^1H , ^{13}C) (Hz)	J (^{13}C , ^{13}C) (Hz)
 zymonic acid	1		178.1		$^3J_{\text{C1-H3}}=11.0$	$^1J_{\text{C1-C2}}=75$, $^2J_{\text{C1-C3}}=12$
	2		149.7			$^1J_{\text{C2-C1}}=75$, $^1J_{\text{C2-C3}}=81$
	3	6.29 (s)	122.1		$^3J_{\text{C3-H3}}=179.0$, $^3J_{\text{C3-H6}}=4.0$	$^1J_{\text{C3-C2}}=81$, $^1J_{\text{C3-C4}}=41$, $^2J_{\text{C3-C1}}=12$
	4		88.2		$^2J_{\text{C4-H3}}=8.5$, $^2J_{\text{C4-H6}}=4.6$	$^1J_{\text{C4-C3}}=41$, $^1J_{\text{C4-C5}}=63$, $^2J_{\text{C4-C6}}=40$
	5		180.2		$^3J_{\text{C5-H6}}=3.9$	$^1J_{\text{C5-C4}}=63$
	6	1.60 (s)	23.2		$^1J_{\text{C6-H6}}=130.3$	$^1J_{\text{C6-C4}}=40$

b	Atom	δ (^1H) (ppm)	δ (^{13}C) (ppm)	J (^1H , ^1H) (Hz)	J (^1H , ^{13}C) (Hz)	J (^{13}C , ^{13}C) (Hz)
 parapyruvic acid	1		176.5			$^1J_{\text{C1-C2}}=62$, $^2J_{\text{C1-C3}}=13$
	2		205.8			$^1J_{\text{C2-C1}}=62$, $^1J_{\text{C2-C3}}=40$
	3	3.03 (d), 3.16 (d)	51.5	$^2J_{\text{H3-H3}}=17.9$		$^1J_{\text{C3-C2}}=40$, $^1J_{\text{C3-C4}}=40$, $^2J_{\text{C3-C1}}=13$
	4		76.3			$^1J_{\text{C4-C3}}=40$, $^1J_{\text{C4-C5}}=55$, $^2J_{\text{C4-C6}}=38$
	5		185			$^1J_{\text{C5-C4}}=55$
	6	1.30 (s)	29			$^1J_{\text{C6-C4}}=38$

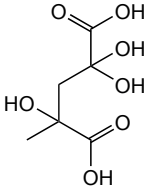
c	Atom	δ (^1H) (ppm)	δ (^{13}C) (ppm)	J (^1H , ^1H) (Hz)	J (^1H , ^{13}C) (Hz)	J (^{13}C , ^{13}C) (Hz)
 parapyruvic acid hydrate	1		177.9			$^1J_{\text{C1-C2}}=65$, $^2J_{\text{C1-C3}}=6$
	2		96.7			$^1J_{\text{C2-C1}}=65$, $^1J_{\text{C2-C3}}=44$
	3	2.30 (d), 2.70 (d)	48.9	$^2J_{\text{H3-H3}}=13.6$		$^1J_{\text{C3-C2}}=44$, $^1J_{\text{C3-C4}}=34$, $^2J_{\text{C3-C1}}=6$
	4		87			$^1J_{\text{C4-C3}}=34$, $^1J_{\text{C4-C5}}=58$, $^2J_{\text{C4-C6}}=39$
	5		181.2			$^1J_{\text{C5-C4}}=58$
	6	1.10 (s)	27			$^1J_{\text{C6-C4}}=39$

Figure 4.7: Chemical shifts and J -coupling constants extracted from NMR data acquired at 14.1 T. Fully ^{13}C -labeled ZA and its decay products dissolved in water reveal the chemical structures of all molecules observed during hyperpolarized experiments. Chemical shifts are unambiguously assigned to each molecule through their J -coupling networks. Shown are proton and carbon chemical shifts, as well as proton to carbon and carbon to carbon coupling constants of (a) zymonic acid, (b) parapyruvic acid and (c) parapyruvic acid hydrate in aqueous solution. (s), singlet. (d), doublet.

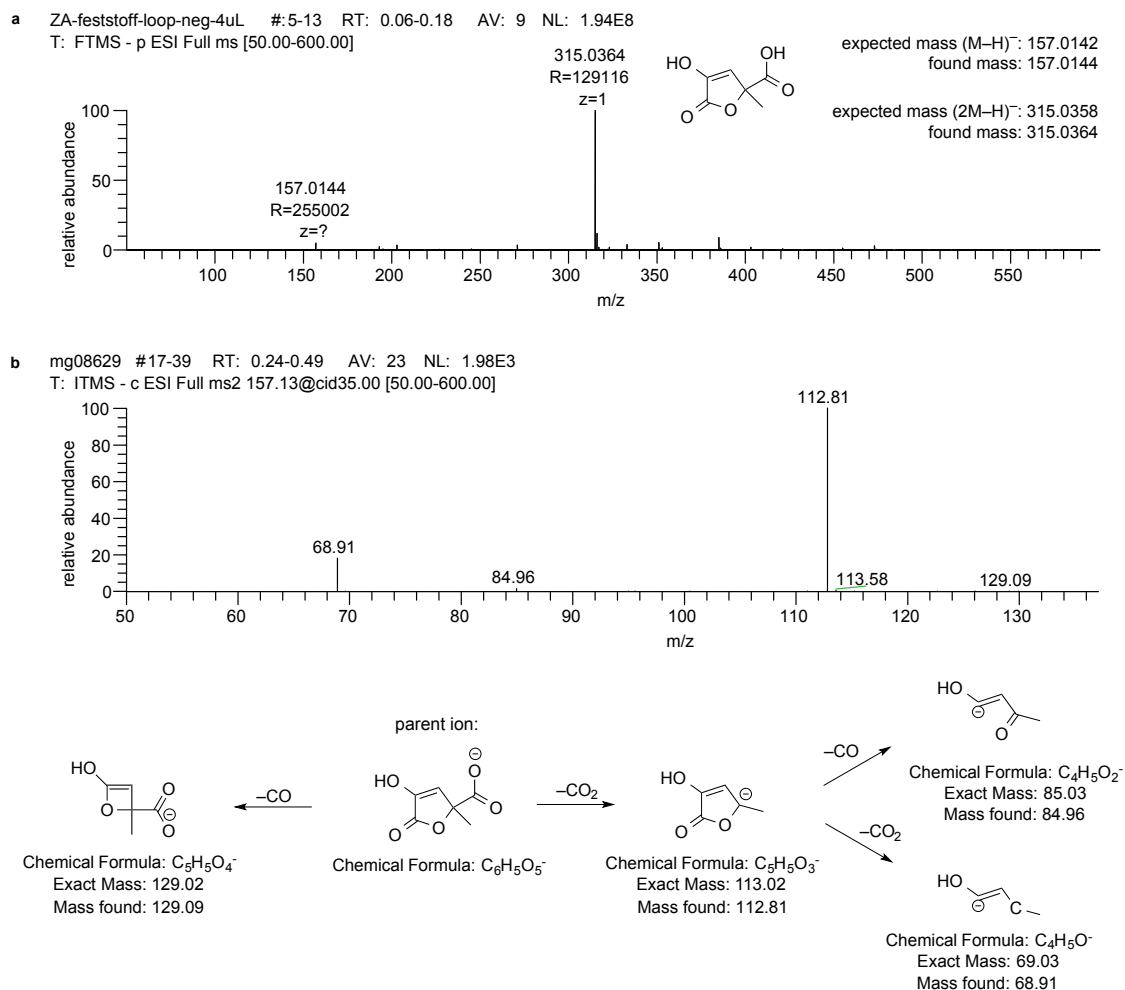


Figure 4.8: Confirmation of the structure of ZA using mass spectrometry. (a) The HR-MS-spectrum of the synthesized substance recorded with a Thermo Finnigan LTQ-FT confirms the total mass of the compound. (b) The MS/MS-spectrum of the synthesized substance recorded after CID-fragmentation on a Thermo Finnigan LCQ-Fleet and the putative assignment of the observed fragments is consistent with the structure. Within the accuracy of the ion trap ($\pm 0.3 m/z$), all peaks can be explained by elimination of carbon monoxide and carbon dioxide.

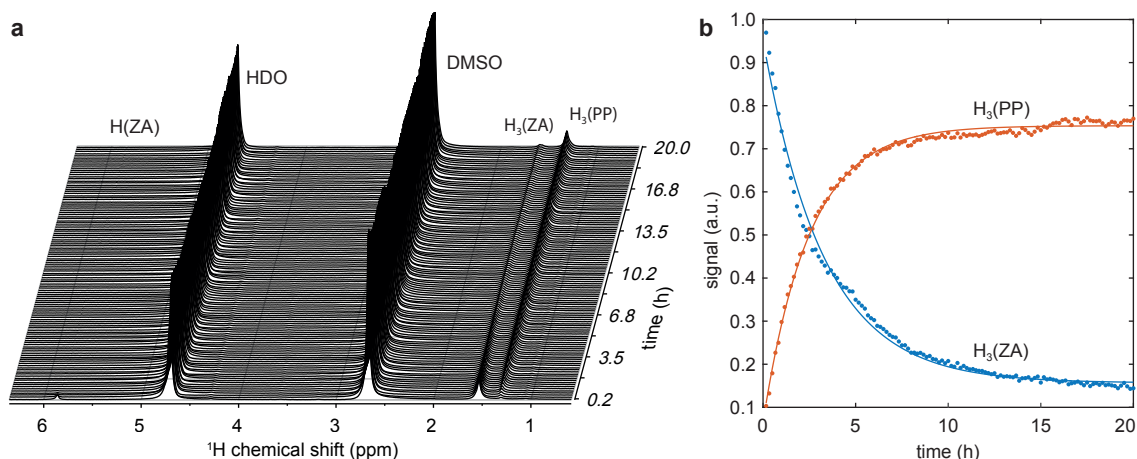


Figure 4.9: Stability of ZA in D_2O as a function of time. Slow chemical decay of ZA into parapyruvic acid (PP) in D_2O at $\text{pH} = 7.54 \pm 0.01$. ^1H spectra were acquired at 1 T and 27°C over 20 h, each spectrum averaged over 60 scans within 10 min. (a) The single proton H(ZA) attached to carbon ZA_3 can be seen at ~ 5.9 ppm, HDO at 4.7 ppm, DMSO at 2.7 ppm, the methyl group $\text{H}_3(\text{ZA})$ attached to carbon ZA_5 at 1.55 ppm and the methyl group $\text{H}_3(\text{PP})$ of parapyruvate hydrate at 1.35 ppm. The single proton attached to carbon ZA_3 is quickly exchanged for a deuteron by keto-enol-tautomerism and can thus only be observed in the first few spectra. (b) Peak amplitudes and exponentially fitted curves of the methyl groups of ZA and parapyruvic acid (PP) from a showing that ZA decays into PP with a half-life of $t_{1/2} = 2.27 \pm 0.04$ h.

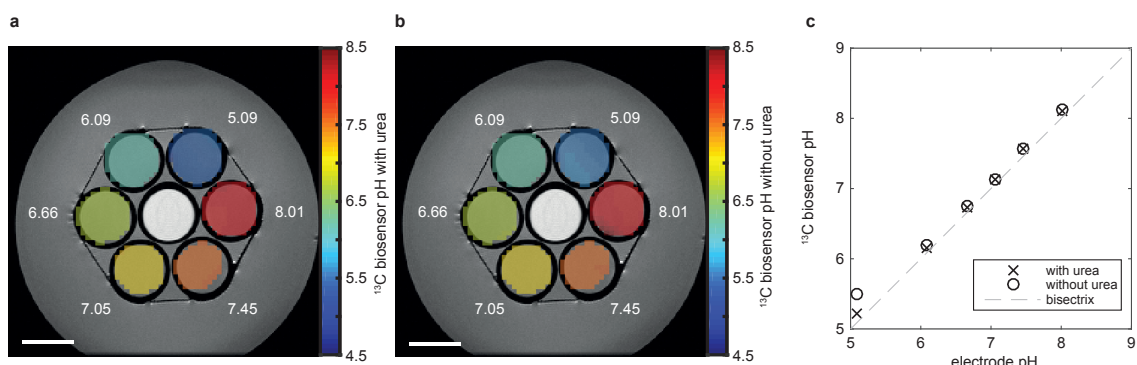


Figure 4.10: ^{13}C biosensor pH of the same buffer phantom measurement evaluated from ZA with and without considering the additional urea peak used as chemical shift reference at 7 T. The ^{13}C biosensor pH was back-calculated based on (a) the chemical shift difference of both ^{13}C -labeled ZA positions with respect to the pH-insensitive ^{13}C -urea and (b) the chemical shift difference between the two ^{13}C -labeled ZA positions only. (c) The pH values extracted from the two ^{13}C pH maps correlate well with the electrode pH (in white in a and b). At the limit of its sensitivity (at $\text{pH} \approx 5$), the back-calculation of the ^{13}C biosensor pH is improved by taking the urea peak into account as pH-insensitive chemical shift reference. Scale bars, 1 cm.

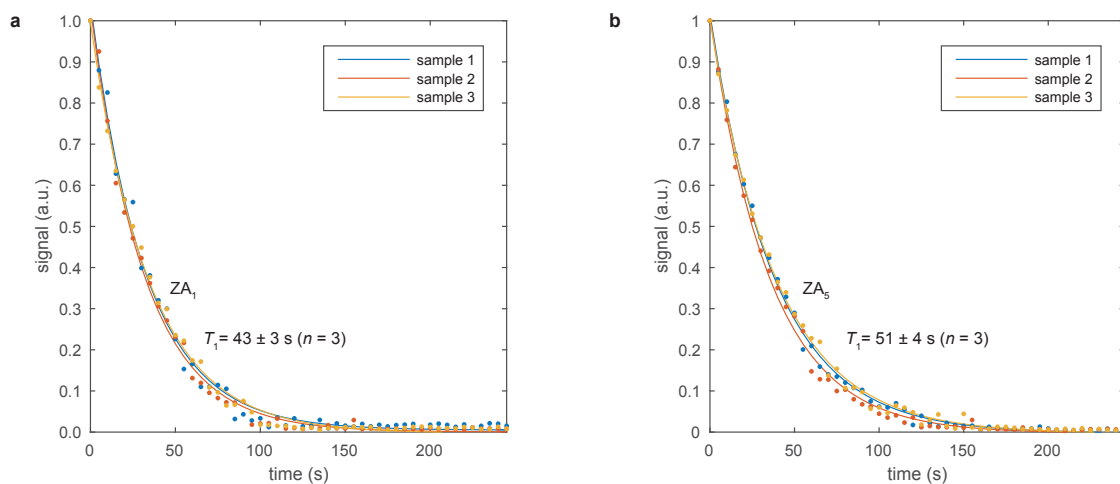


Figure 4.11: Longitudinal relaxation time T_1 of hyperpolarized natural abundance ZA *in vitro* at 3 T. A three-parameter monoexponential curve was fitted to each dataset and the mean and standard deviation was calculated from the resulting decay constants of 50 mM ZA in 80 mM Tris buffer in H_2O adjusted with 1 M NaOH to an average pH of 6.53 ± 0.03 at 27°C . The close proximity of the frequently and fast exchanging proton of the hydroxy group attached to carbon number two of ZA most likely causes the shorter T_1 of (a) carbon number one (ZA_1) compared to (b) carbon number five (ZA_5) of ZA *in vitro*.

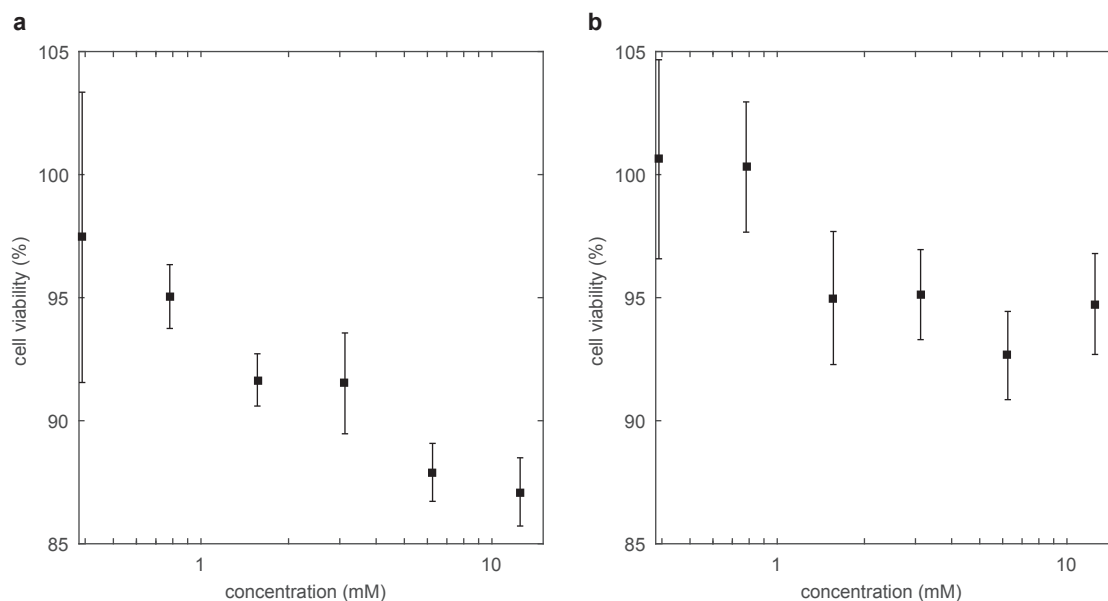


Figure 4.12: Cytotoxicity tests show that ZA is non-toxic within experimentally relevant concentration ranges. Typical concentrations of hyperpolarized substances injected into animals are on the order of 60–100 mM at a dose of $\sim 5 \text{ mL kg}^{-1}$, resulting in an end concentration of the substance in the blood of 6–10 mM assuming a ratio of injected volume to blood volume in the order of 1:10. Therefore, 5000 HeLa cells each in 100 μL cell culture medium were incubated with ZA for 24 h at concentrations 0.4–12.5 mM (a) without and (b) with a Zn catalyst being used in the synthesis of ZA before being purified using reversed phase HPLC. No marked reduction in cell viability was observed ($n = 3$, mean \pm s.d.).

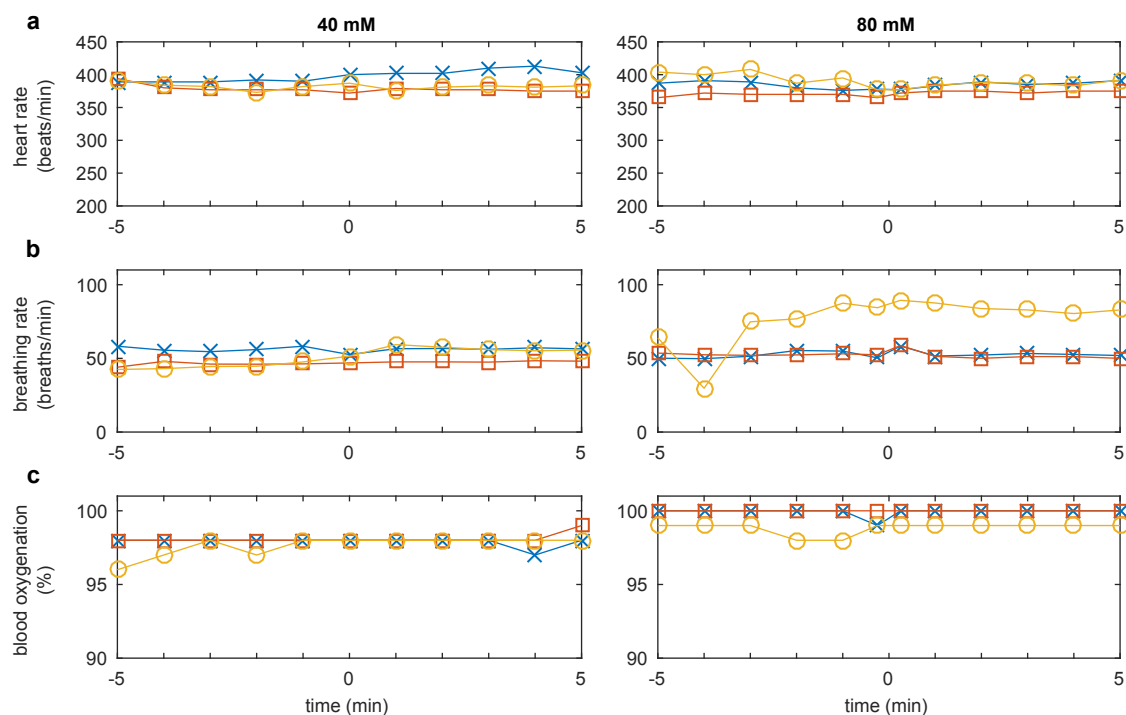


Figure 4.13: Dose escalation study testing for *in vivo* toxicity of ZA in three rats. ZA was dissolved in 80 mM Tris buffer solution, neutralized to normal blood pH ≈ 7.4 using NaOH, sterile filtered and injected into the tail vein at $t = 0$ min at a final injected concentration of 40 mM and 80 mM, at a dose of 5 mL kg^{-1} and a rate of 0.17 mL s^{-1} . For all three rats (Lewis, male, Charles River, average weight 319 ± 1 g), (a) heart rate, (b) breathing rate and (c) blood oxygenation were monitored for 5 minutes before and after injection. No abnormalities with respect to the injection of ZA were detected.

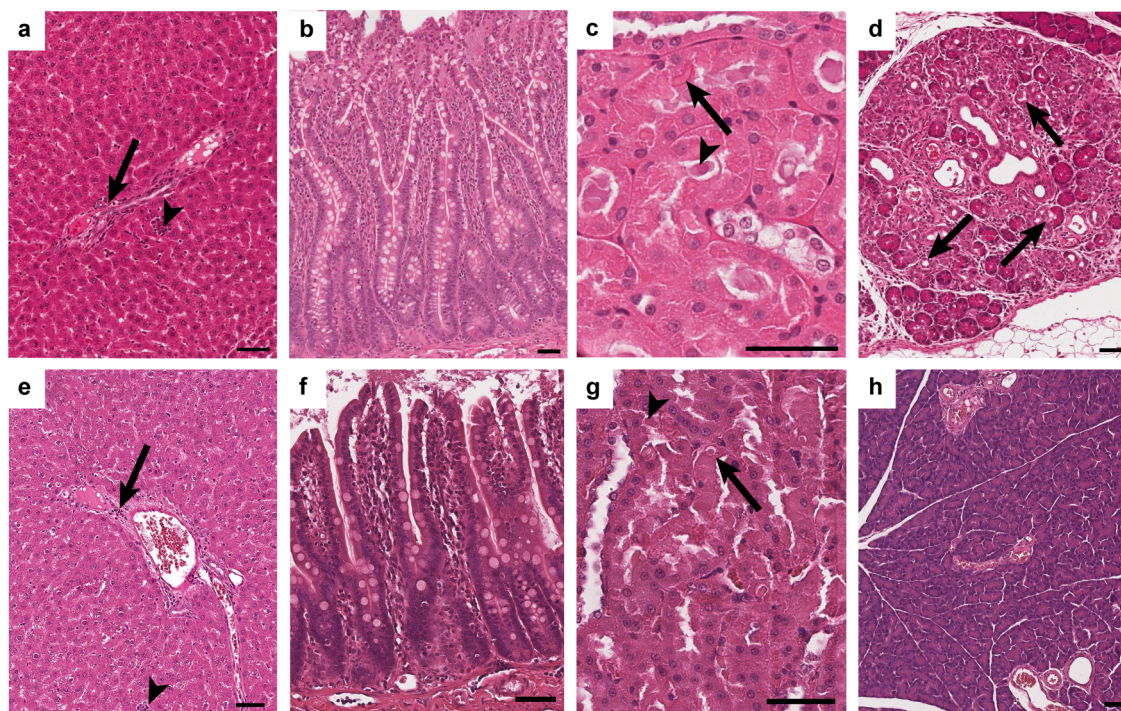


Figure 4.14: A toxicopathological study shows non-ZA-associated alterations both within exposed and unexposed animals. Representative images of background alterations observed histopathologically in (a, e) liver, (b, f) intestines, (c, g) kidney and (d, h) pancreas in animals after NaCl administration (upper row) and after fivefold overdose of ZA (lower row). (a, e) In the liver, slight periportal infiltration predominantly with lymphocytes was observed in the periportal region (arrows) and intralobular (arrowheads). (b, f) Slight mixed infiltration and fibrosis of the villi occurred in all parts of the intestines. (c, g) In the kidney, intraepithelial (arrows) and intraluminal (arrowheads) hyaline droplets within the proximal tubuli were observed only in male rats regardless of the injected compound. (d) One of the control animals showed a focal acinar-to-ductular metaplasia within the pancreas. The arrows indicate metaplastic ductular formations. (h) Normal pancreatic tissue in an animal after fivefold overdose of ZA. H&E staining. Scale bars, 50 μm .

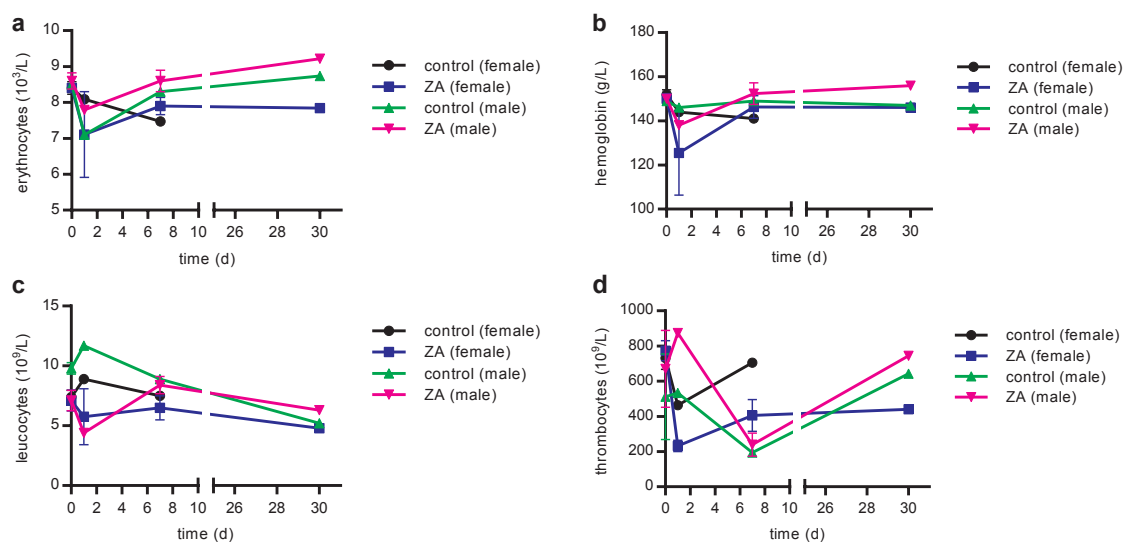


Figure 4.15: Non-toxicity of ZA was substantiated by blood collection for hematology and clinical chemistry before and 24 h (acute), 7, 21 and 30 days (sub-acute) after injection of ZA. Here, four representative mean values of the blood analysis are shown: (a) erythrocytes, (b) hemoglobin, (c) leucocytes, and (d) thrombocytes. All levels are close to the reference levels (erythrocytes: $5.5\text{--}9.3 \times 10^3 \text{ L}^{-1}$, hemoglobin: $106\text{--}156 \text{ g L}^{-1}$, leucocytes: $3.3\text{--}8.7 \times 10^9 \text{ L}^{-1}$, thrombocytes: $500\text{--}1300 \times 10^9 \text{ L}^{-1}$) provided by the supplier (Charles River) and no significant difference between ZA and NaCl injected animals can be detected. 14 animals (7 female / 7 male) were used, 10 of them received a tail vein injection of 5 mL kg^{-1} with a concentration of 250 mM ZA (5 times the dosage used for the imaging experiments), 4 animals served as controls with a tail vein injection of saline (0.09% w/v of NaCl) (see also Methods section).

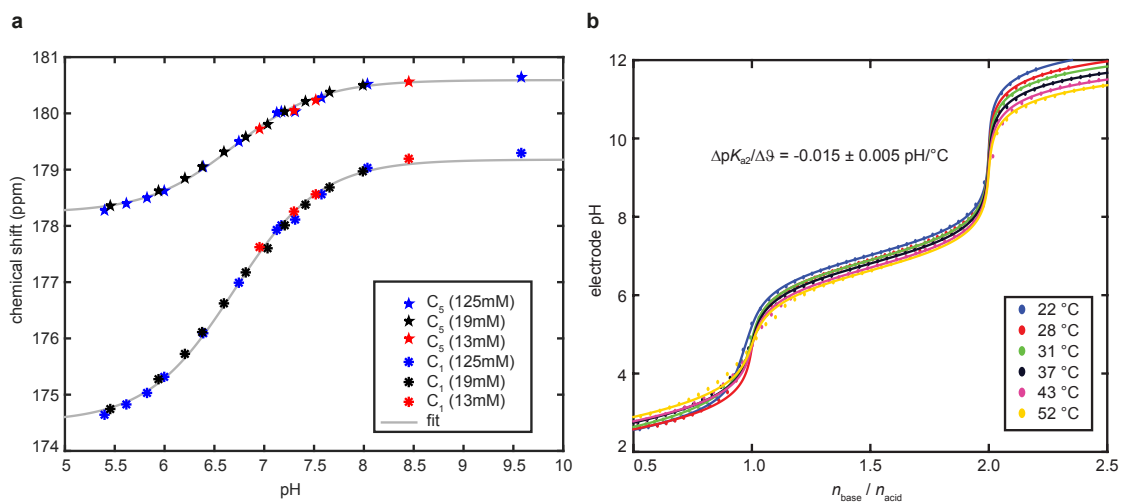


Figure 4.16: Concentration and temperature dependence of the pH detection using ZA. (a) Chemical shifts as a function of pH are independent of the concentration of ZA within experimentally relevant concentration ranges. ^{13}C chemical shifts of ZA_5 and ZA_1 at starting concentrations of 125, 19 and 13 mM ZA at 14.1 T and 37 °C in 1 M phosphate buffer, titrated in random order to different pH values using 1 M HCl and 1 M NaOH. The fast proton exchange mechanism leading to changes in chemical shift as a function of pH is independent of the concentration of ZA itself. (b) ZA shows a weak temperature dependence of the relevant acid dissociation constant pK_{a2} . A 25 mM solution of ZA in 5 mL 1 M KCl in H_2O was titrated with 1 M KOH at different temperatures. Each full titration was performed within 22 ± 1 min and a theoretical titration curve for a diprotic acid was fitted to each titration experiment. Evaluating the relevant extracted acid dissociation constant pK_{a2} as a function of temperature results in a weak temperature dependence of $\Delta pK_{a2}/\Delta\vartheta = -0.015 \pm 0.005 \text{ pH}/^\circ\text{C}$, making ZA a temperature independent pH reporter within biologically relevant temperatures.

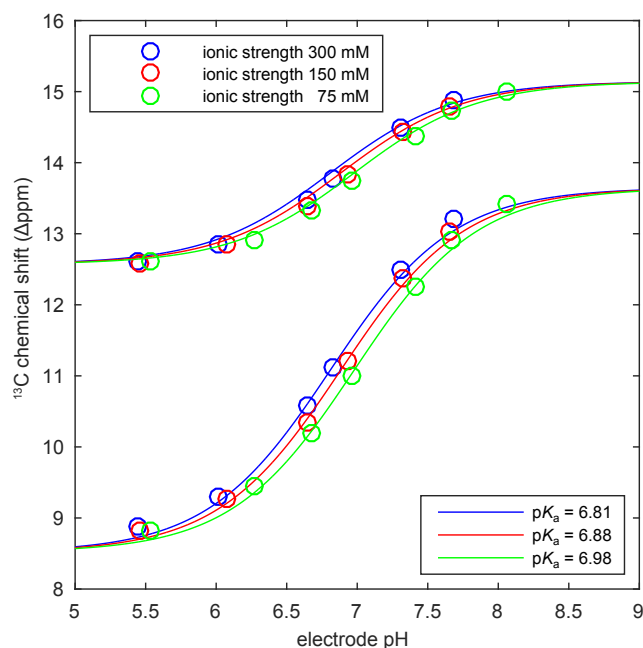


Figure 4.17: Thermal ^{13}C chemical shift as a function of electrode pH at three different ionic strengths at 5.9 T. 20 mM $[1,5-^{13}\text{C}_2]\text{ZA}$ and 20 mM ^{13}C -urea in KCl solution of varying ionic strength containing 10% D_2O were titrated with 2.5 M KOH. The total given ionic strength is the sum of the ionic strength of KCl and single charged zymonic acid. The measurements were performed at 37 °C and 5.9 T. From a linear fit to the fitted acid dissociation constant pK_a as a function of ionic strength I one finds $\Delta pK_a/\Delta I = -0.7 \times 10^{-3}$ pH/mM, so that the pH uncertainty in the physiological range with an ionic strength of 135–165 mM results in ~ 0.02 pH units.

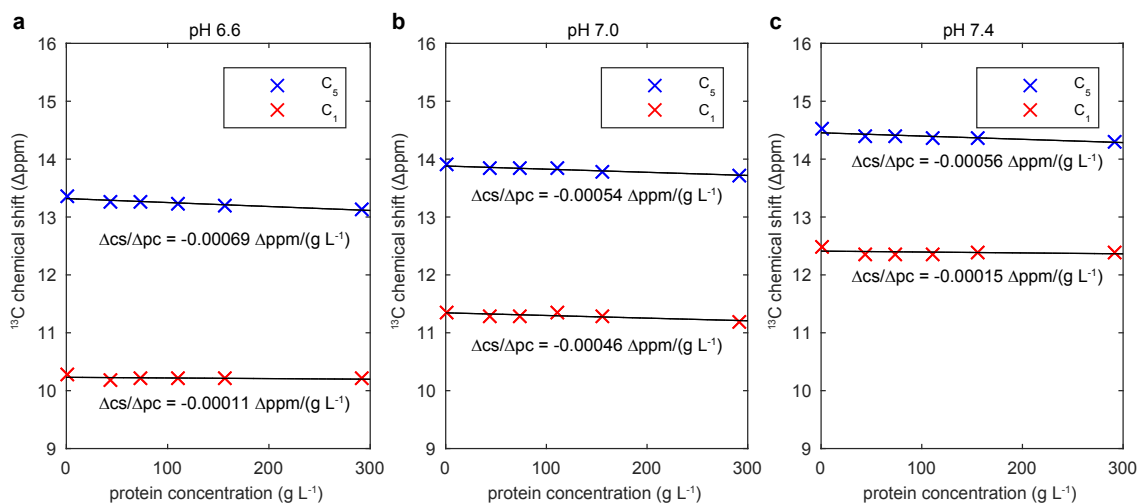


Figure 4.18: Thermal ^{13}C chemical shift of $[1,5\text{-}^{13}\text{C}_2]\text{ZA}$ at three different pH values as a function of protein concentration at 5.9 T. 20 mM $[1,5\text{-}^{13}\text{C}_2]\text{ZA}$ and 20 mM ^{13}C -urea in 130 mM KCl and 10% D_2O were set to the pH values (a) 6.6, (b) 7.0 and (c) 7.4 at 37°C . Increasing amounts of bovine serum albumin were added and the pH was readjusted before each individual measurement. From the linear fits we detected a maximum change in chemical shift cs as a function of protein concentration pc of $\Delta\text{cs}/\Delta\text{pc} = -0.7 \times 10^{-3} \text{ } \Delta\text{ppm}/(\text{g L}^{-1})$, so that the pH uncertainty in the physiological range with a protein concentration of $60\text{--}80 \text{ g L}^{-1}$ results in ~ 0.01 pH units.

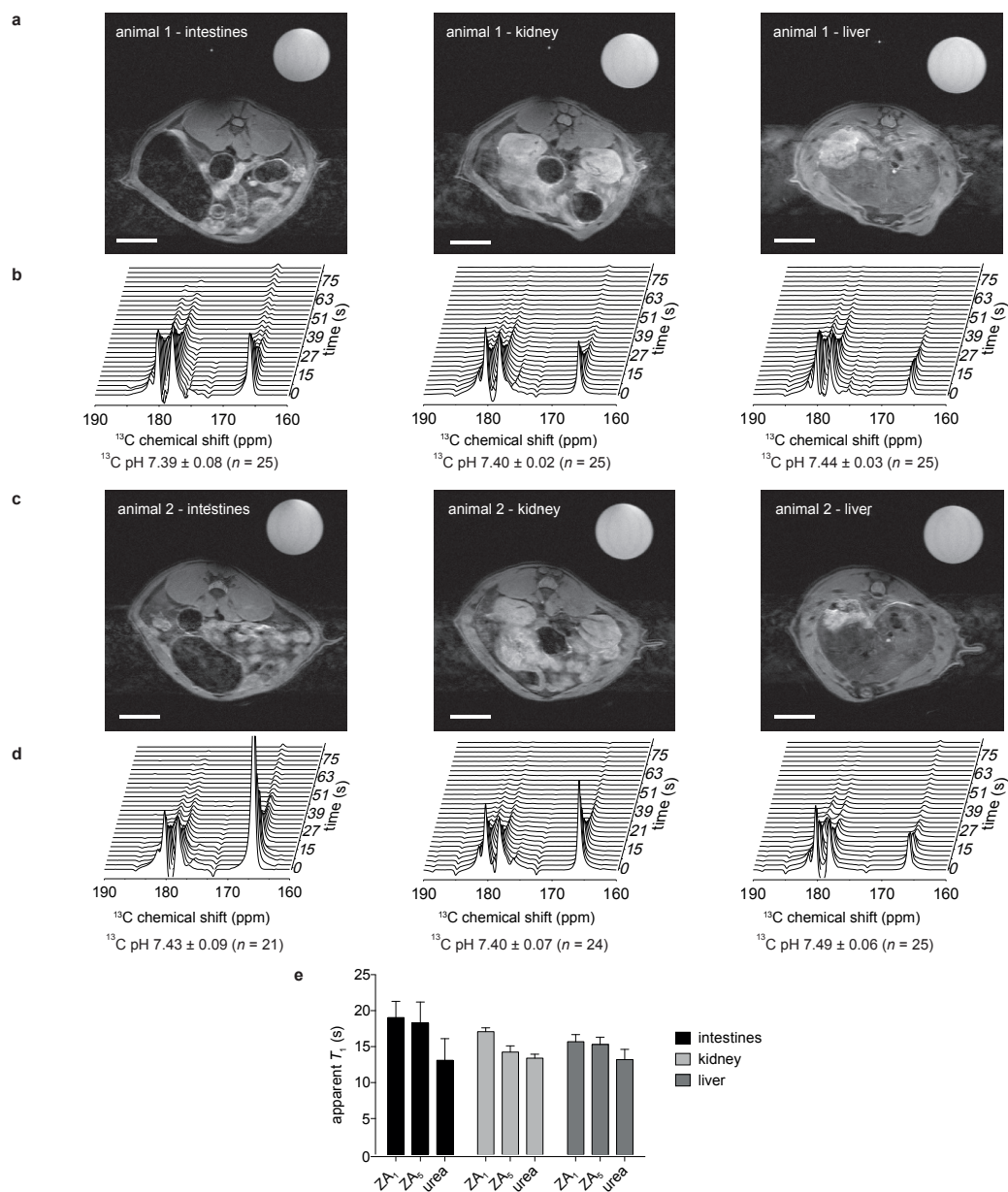


Figure 4.19: Apparent longitudinal relaxation time T_1 of hyperpolarized ZA *in vivo* at 7T. (a, c) Proton anatomical images of the three axial slices through intestines, kidney and liver where pH and T_1 measurements were performed within two animals. (b, d) Time resolved slice selective spectra of hyperpolarized ZA and ^{13}C -urea report consistent pH values within the physiologically expected pH range after tail vein injection. (e) Monoexponential decay curves fitted to the peak maxima of ZA_1 , ZA_5 and urea result in slightly longer apparent T_1 times for ZA compared to urea and no significant differences in apparent T_1 between the three slices. For each *in vivo* experiment, spectra from 64 time steps were recorded using a flip angle of 10° and a TR of 3s. The pH values were calculated from the difference of the chemical shifts of ZA_1 , ZA_5 and urea. The ^{13}C pH values are given as mean \pm standard deviation of the n spectra that could be used for the back-calculation of the pH due to sufficient SNR. Scale bars, 1 cm.

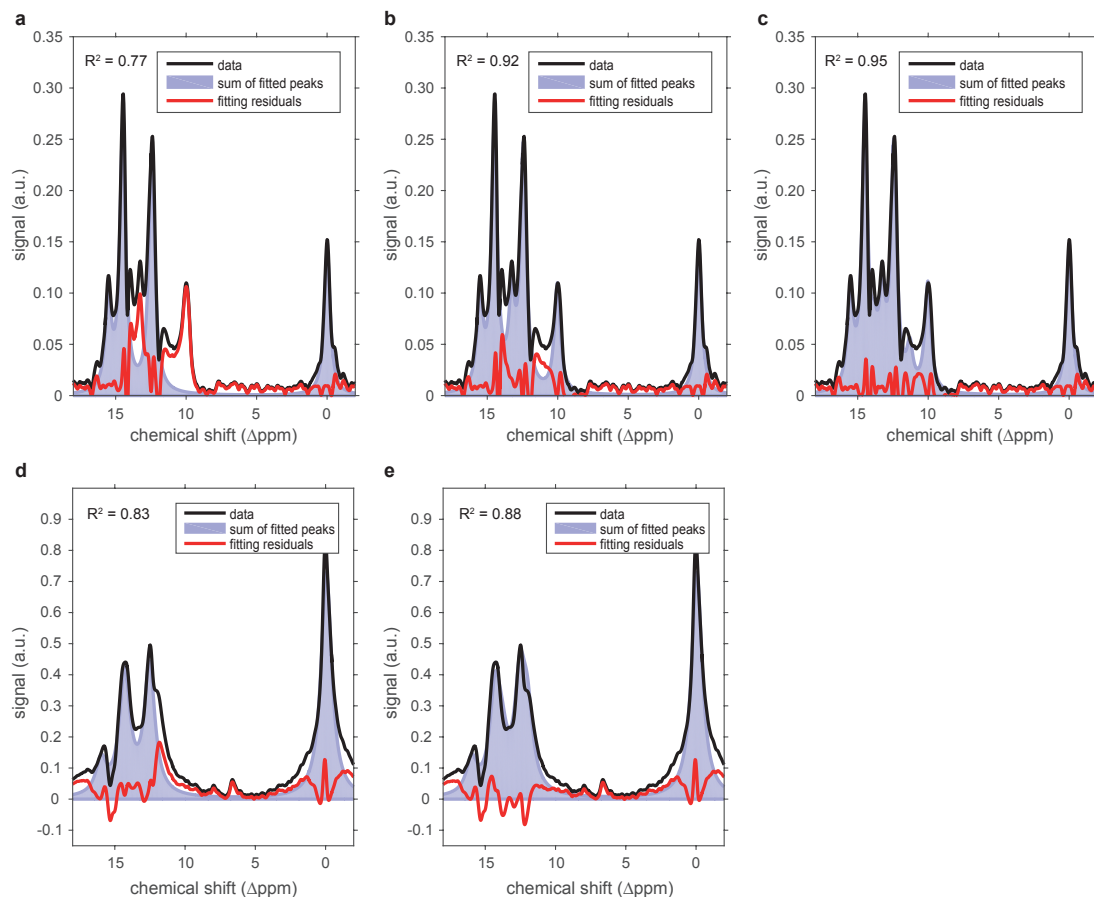


Figure 4.20: Representative fits and fitting residuals for multiple tissue compartments in the kidneys and in the tumor. (a–c) In the kidneys, increasing the number of fitted zymonic acid peak pairs from one (a, $R^2 = 0.77$) to two (b, $R^2 = 0.92$) to three (c, $R^2 = 0.95$) results in a reduction of the fitting residuals (red line) and an improved coefficient of determination R^2 . (d–e) Analogously, increasing the number of fitted zymonic acid peak pairs from one (d, $R^2 = 0.83$) to two (e, $R^2 = 0.88$) results in a reduction of the fitting residuals (red line) and an improved coefficient of determination R^2 in the tumor. Urea (0 ppm) and parapyruvate hydrate (15.7 ppm) are fitted in all spectra.

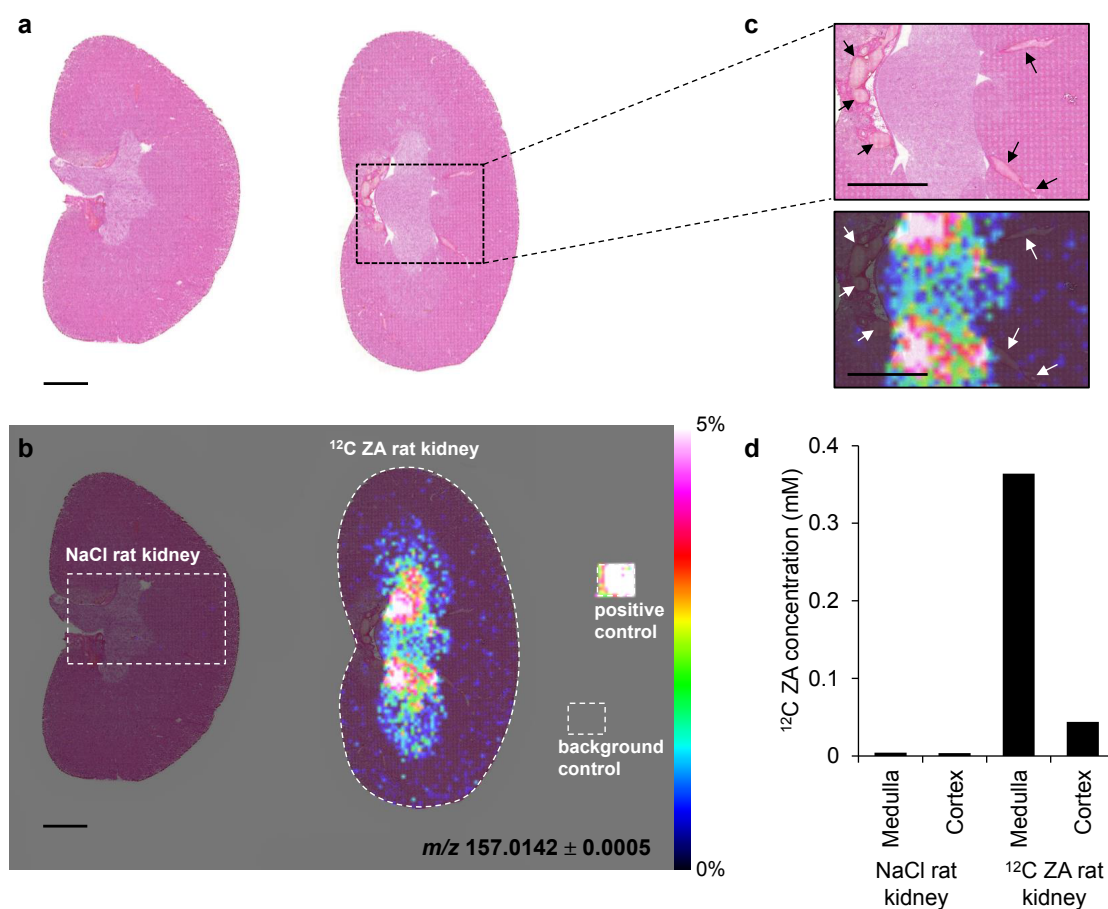


Figure 4.21: Distribution of ^{12}C ZA in rat kidney and extravasation into kidney tissue was confirmed by matrix-assisted laser desorption/ionization mass spectrometry imaging (MALDI-MSI). (a) H&E stains of analyzed tissue sections. (b) Distribution of ^{12}C ZA (m/z 157.0142) in kidney section 30 s after injection of 5 mL kg^{-1} 250 mM ^{12}C -ZA. The control rat was administered with isotonic saline. A positive control, 1 mM ^{12}C -ZA droplet on slide, and a non-tissue measurement region acting as a background control were included in the measurement. All samples were coated with 9-aminoacridine and analyzed in negative mode on a FT-ICR MS. Data was acquired at a spatial resolution of $150\text{ }\mu\text{m}$ and normalized by root mean square. Dashed lines mark the measurement regions. (c) Higher magnification image showing arterial and venous blood vessels (black and white arrows) and high abundant signals of ZA in the medulla of the kidney. (d) Mean ^{12}C ZA concentrations in renal cortex and medulla. MALDI-MSI represents the distribution of ZA within the kidney fixed 2–3 min after injection whereas hyperpolarized MRI shows the distribution of ZA within the kidney 10 s after injection. Whereas in the hyperpolarized MR image, shortly after injection, the cortex exhibits the largest contribution to the overall signal, in MALDI-MSI, much longer after injection, more ZA is already involved in the renal filtering process and thus the area containing the medulla and calyx show the largest signal contribution. Scale bars, 2 mm.

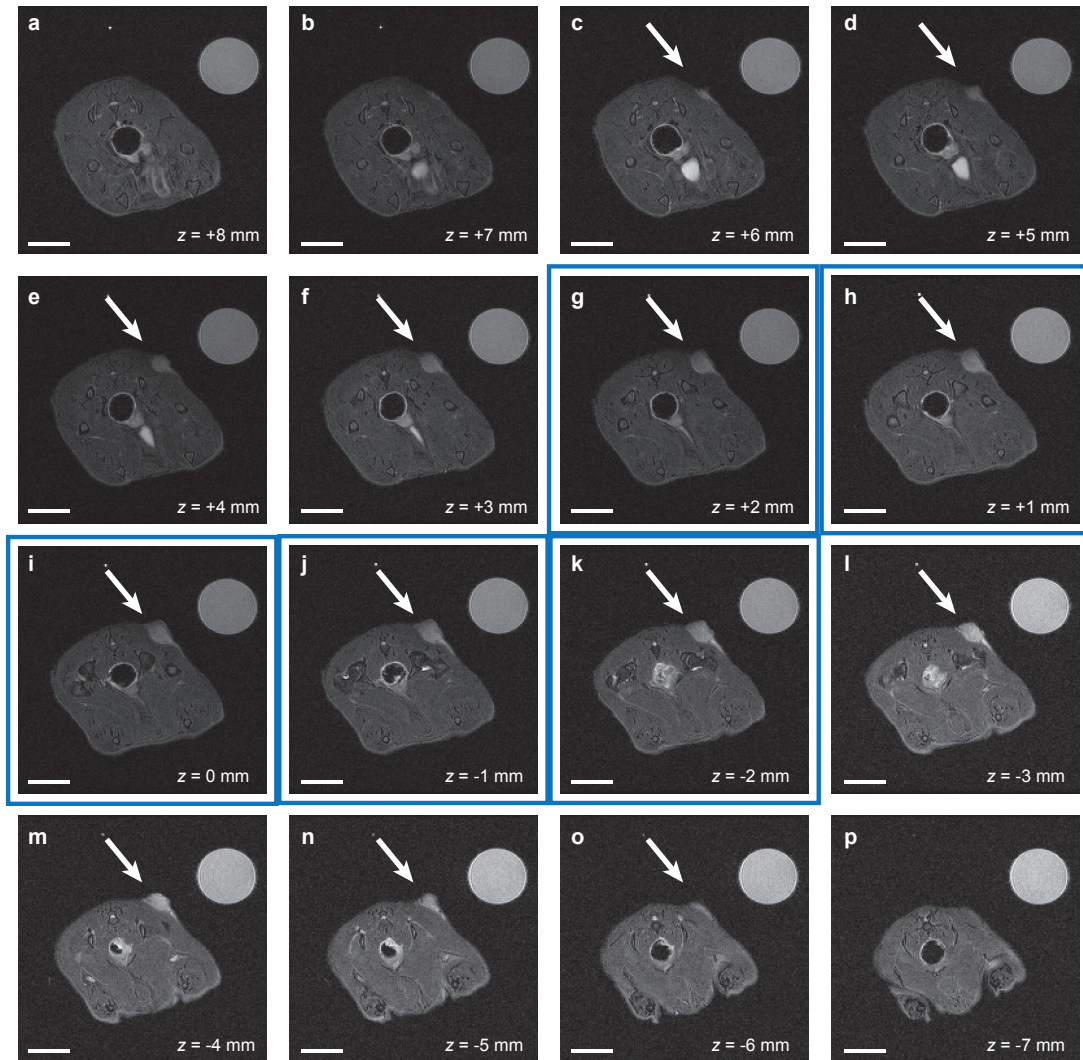


Figure 4.22: Axial slices from the animal shown in Fig. 4.5 bearing a MAT B III tumor (arrow). (a–p) Proton images with a field of view of 6 cm were acquired every 1 mm using a fast spin echo sequence (see Methods section). (g–k) The five proton images contained within the 5 mm thick hyperpolarized ^{13}C image are marked with a blue box. Image (i) represents the central tumor slice and coincides with the center of the 5 mm thick hyperpolarized ^{13}C image. Scale bars, 1 cm.

Table 4.1: Toxicopathological study. Distribution of histopathological alterations after a single administration of ZA at 5 times the dosage used for the imaging experiments, compared to NaCl administration after 24 h and 4 weeks, respectively. Overall, no significant histopathological difference between the ZA and NaCl injected animals could be detected.

	NaCl 24 h		ZA 24 h		NaCl 4 weeks		ZA 4 weeks	
	female	male	female	male	female	male	female	male
Liver								
inflammation, focal, slight	1/1	0/1	1/2	1/2	1/1	3/3	1/1	3/3
fatty change, macrovesicular, zone 3, slight	0/1	0/1	0/2	1/2	0/1	0/3	0/1	0/3
GI								
inflammation, mixed, diffuse, with fibroplasia, slight	1/1	1/1	2/2	2/2	1/1	3/3	1/1	3/3
Kidney								
accumulation, hyaline droplets, proximal tubules, slight/moderate	0/1	1/1	0/2	2/2	0/1	1/1	0/3	3/3
Pancreas								
metaplasia, ductular, focal, slight	0/1	0/1	0/2	0/2	1/1	0/1	0/3	0/3

5 Conclusion

“I was as excited by this result as a sailor would be who, after a long voyage, sees from afar, the longed-for land.”

— Max Born (* 1882; † 1970)

In this work, new imaging methods for the study of tumor metabolism *in vivo* were developed: They are on the one hand based on a combination of techniques to probe tumor perfusion, pyruvate metabolism and cell necrosis, and on the other hand based on the discovery and development of zymonic acid as a novel extracellular pH imaging sensor. Specifically, the following contributions were made to the steadily growing number of methods and applications becoming available in the field of hyperpolarized ^{13}C magnetic resonance spectroscopic imaging (^{13}C -MRSI):

- In Chapter 3, an implementation for the investigation of tumor perfusion, metabolism and necrosis using hyperpolarized ^{13}C -MRSI was presented and demonstrated in an orthotopic rat hepatocellular carcinoma (HCC) model system before and after transcatheter arterial embolization (TAE). Qualitative perfusion information was derived from $[^{13}\text{C}, ^{15}\text{N}_2]$ urea images. Spatially resolved maps of apparent rate constants describing the forward label exchange of $[1\text{-}^{13}\text{C}]$ pyruvate to $[1\text{-}^{13}\text{C}]$ alanine and $[1\text{-}^{13}\text{C}]$ lactate were acquired to quantify tumor metabolism, while spatially resolved maps calculated from the ratio of $[1,4\text{-}^{13}\text{C}_2]$ malate to $[1,4\text{-}^{13}\text{C}_2]$ fumarate were used to quantify tumor necrosis. Owing to their small molecular size, all injected compounds, taken together with their respective metabolites, exhibited similar overall signal distributions *in vivo*. TAE induced a decrease of blood flow into the tumor; metabolic conversion rates remained stable or increased in tumor, muscle and liver tissue upon TAE. Conversion from fumarate to malate correlated with individual levels of tumor necrosis independently determined by histology. Global malate signals after TAE suggested the washout of either fumarase or malate due to cell membrane permeabilization during necrosis.

This work presented the first combined implementation of hyperpolarized urea, pyruvate and fumarate ^{13}C -MRSI for the investigation of tumor perfusion, metabolism and necrosis formation in an orthotopic rat HCC model system. While the perfusion and necrosis information showed clear trends in response to the treatment, the detected changes in metabolic activity of the tumors remained less conclusive. These results underline the importance of multiparametric techniques for future research in tumor characterization and therapy response evaluation.

- Chapter 4 introduced a novel method for non-invasive imaging of extracellular pH *in vivo* using zymonic acid. In humans, local pH changes can be caused by pathologies, such as cancer, which overrule natural pH regulatory mechanisms. The pH-sensitive molecule $[1,5-^{13}\text{C}_2]$ zymonic acid was discovered and identified during metabolic studies of tumor cells. Additionally, the feasibility of its selectively ^{13}C -labeled synthesis from $[1-^{13}\text{C}]$ pyruvic acid was demonstrated. Zymonic acid's ^{13}C resonance frequencies shift up to ~ 3.0 ppm per pH in the physiologically and pathologically relevant pH range, independent of concentration, temperature, ionic strength and protein concentration, demonstrating the robustness of this pH measurement method. Zymonic acid was characterized as a non-toxic compound and found to be predominantly present in the extracellular space using matrix-assisted laser desorption/ionization-mass spectrometry imaging (MALDI-MSI). A hyperpolarization recipe of zymonic acid was developed, and the hyperpolarized signal enhancement (with a solution polarization level of $22 \pm 2\%$) of the two ^{13}C positions has a lifetime long enough for the acquisition of pH images using ^{13}C -MRSI (with longitudinal relaxation times T_1 of 43 ± 3 s and 51 ± 4 s at a clinical magnetic field strength of 3 T). The method's ability to acquire pH images within pH buffer and blood phantoms was experimentally demonstrated *in vitro*. Additionally, *in vivo* pH images from rat bladder, kidneys and subcutaneously inoculated tumors derived from a mammary adenocarcinoma cell line were shown. The detected acidity of the extravascular MAT B III tumor compartment (^{13}C pH = 6.95 ± 0.12) was independently confirmed using the extracellular ^{31}P probe 3-APP (see also Section 2.4.2) and a needle-type optical sensor *in vivo*, as well as using a standard pH microelectrode *ex vivo*.

A unique feature of pH sensors based on changes in chemical shift as a function of pH is the ability to detect several pH compartments within the same voxel, which was demonstrated for the first time with a ^{13}C -labeled and hyperpolarized compound *in vivo* using zymonic acid. This is in stark contrast to pH images based on ratiometric approaches, which are based on signal contributions from several compartments (see also Section 2.4.3.1) resulting in just a single, mean pH per voxel. Therefore, future research using zymonic acid could allow a more precise determination of the extracellular pH, making this method ideally suited to improve understanding, diagnosis and therapy of diseases characterized by aberrant acid-base balance.

Bringing these methods together will lead to a promising approach for a comprehensive metabolic characterization of tumors, as well as for selection, monitoring and individualization of cancer therapies. Urea, which is already being copolarized as a chemical shift reference for zymonic acid, could be used to simultaneously derive perfusion information and thus to concurrently characterize perfusion and pH during the same experiment. The successive performance of a copolarized zymonic acid/urea experiment, a copolarized pyruvate/urea experiment and a fumarate experiment will allow to collect information on pH, perfusion, metabolism and necrosis from the same subject.

In summary, new imaging methods for non-invasive studies of tumor metabolism were developed and applied *in vivo* within this work. A highlight is the discovery, identification, synthesis, hyperpolarization, characterization and *in vivo* application of the novel pH imaging sensor zymonic acid. In the future, these methods and their applications hopefully prove to have contributed to steadily pushing the field of hyperpolarized ^{13}C magnetic resonance spectroscopic imaging closer towards a successful clinical translation.

Bibliography

- [1] A. Abragam and M. Goldman. “Principles of dynamic nuclear polarisation”. *Reports on Progress in Physics*, vol. 41, pp. 395–467, 1978. DOI: 10.1088/0034-4885/41/3/002.
- [2] J. J. Ackerman, G. E. Soto, W. M. Spees, Z. Zhu, and J. L. Evelhoch. “The NMR chemical shift pH measurement revisited: analysis of error and modeling of a pH dependent reference”. *Magnetic Resonance in Medicine*, vol. 36, pp. 674–683, 1996. DOI: 10.1002/mrm.1910360505.
- [3] R. W. Adams, J. A. Aguilar, K. D. Atkinson, M. J. Cowley, P. I. P. Elliott, S. B. Duckett, G. G. R. Green, I. G. Khazal, J. Lopez-Serrano, and D. C. Williamson. “Reversible interactions with parahydrogen enhance NMR sensitivity by polarization transfer”. *Science*, vol. 323, pp. 1708–1711, 2009. DOI: 10.1126/science.1168877.
- [4] S. Aime, A. Barge, D. Delli Castelli, F. Fedeli, A. Mortillaro, F. U. Nielsen, and E. Terreno. “Paramagnetic lanthanide(III) complexes as pH-sensitive chemical exchange saturation transfer (CEST) contrast agents for MRI applications”. *Magnetic Resonance in Medicine*, vol. 47, pp. 639–648, 2002. DOI: 10.1002/mrm.10106.
- [5] S. Aime, L. Calabi, L. Biondi, M. De Miranda, S. Ghelli, L. Paleari, C. Rebaudengo, and E. Terreno. “Iopamidol: exploring the potential use of a well-established X-ray contrast agent for MRI”. *Magnetic Resonance in Medicine*, vol. 53, pp. 830–834, 2005. DOI: 10.1002/mrm.20441.
- [6] M. J. Albers, R. Bok, A. P. Chen, C. H. Cunningham, M. L. Zierhut, V. Y. Zhang, S. J. Kohler, J. Tropp, R. E. Hurd, Y. F. Yen, S. J. Nelson, D. B. Vigneron, and J. Kurhanewicz. “Hyperpolarized ^{13}C lactate, pyruvate, and alanine: noninvasive biomarkers for prostate cancer detection and grading”. *Cancer Research*, vol. 68, pp. 8607–8615, 2008. DOI: 10.1158/0008-5472.CAN-08-0749.
- [7] J. Altomonte, R. Braren, S. Schulz, S. Marozin, E. J. Rummeny, R. M. Schmid, and O. Ebert. “Synergistic antitumor effects of transarterial viroembolization for multifocal hepatocellular carcinoma in rats”. *Hepatology*, vol. 48, pp. 1864–1873, 2008. DOI: 10.1002/hep.22546.

- [8] M. Anderson, A. Moshnikova, D. M. Engelman, Y. K. Reshetnyak, and O. A. Andreev. “Probe for the measurement of cell surface pH in vivo and ex vivo”. *Proceedings of the National Academy of Sciences of the United States of America*, vol. 113, pp. 8177–8181, 2016. DOI: 10.1073/pnas.1608247113.
- [9] S. Appelt, A. B. Baranga, C. J. Erickson, M. V. Romalis, A. R. Young, and W. Happer. “Theory of spin-exchange optical pumping of ^3He and ^{129}Xe ”. *Physical Review A*, vol. 58, pp. 1412–1439, 1998. DOI: 10.1103/PhysRevA.58.1412.
- [10] J. H. Ardenkjaer-Larsen. “On the present and future of dissolution-DNP”. *Journal of Magnetic Resonance*, vol. 264, pp. 3–12, 2016. DOI: 10.1016/j.jmr.2016.01.015.
- [11] J. H. Ardenkjaer-Larsen, B. Fridlund, A. Gram, G. Hansson, L. Hansson, M. H. Lerche, R. Servin, M. Thaning, and K. Golman. “Increase in signal-to-noise ratio of $> 10,000$ times in liquid-state NMR”. *Proceedings of the National Academy of Sciences of the United States of America*, vol. 100, pp. 10158–10163, 2003. DOI: 10.1073/pnas.1733835100.
- [12] Y. Asayama, K. Yoshimitsu, Y. Nishihara, H. Irie, S. Aishima, A. Taketomi, and H. Honda. “Arterial blood supply of hepatocellular carcinoma and histologic grading: radiologic-pathologic correlation”. *AJR American Journal of Roentgenology*, vol. 190, W28–W34, 2008. DOI: 10.2214/AJR.07.2117.
- [13] Robert L. Augustine and Leonard P. Calbo. “Self-condensation of α -keto esters under Stobbe condensation conditions”. *The Journal of Organic Chemistry*, vol. 33, pp. 838–840, 1968. DOI: 10.1021/jo01266a078.
- [14] F. Bloch. “Nuclear induction”. *Physical Review*, vol. 70, pp. 460–474, 1946. DOI: 10.1103/PhysRev.70.460.
- [15] F. Bloch, W. W. Hansen, and M. Packard. “Nuclear induction”. *Physical Review*, vol. 69, p. 127, 1946. DOI: 10.1103/PhysRev.69.127.
- [16] S. E. Bohndiek, M. I. Kettunen, D. E. Hu, and K. M. Brindle. “Hyperpolarized ^{13}C spectroscopy detects early changes in tumor vasculature and metabolism after VEGF neutralization”. *Cancer Research*, vol. 72, pp. 854–864, 2012. DOI: 10.1158/0008-5472.CAN-11-2795.
- [17] S. E. Bohndiek, M. I. Kettunen, D. E. Hu, T. H. Witney, B. W. Kennedy, F. A. Gallagher, and K. M. Brindle. “Detection of tumor response to a vascular disrupting agent by hyperpolarized ^{13}C magnetic resonance spectroscopy”. *Molecular Cancer Therapeutics*, vol. 9, pp. 3278–3288, 2010. DOI: 10.1158/1535-7163.MCT-10-0706.
- [18] C. R. Bowers and D. P. Weitekamp. “Parahydrogen and synthesis allow dramatically enhanced nuclear alignment”. *Journal of the American Chemical Society*, vol. 109, pp. 5541–5542, 1987. DOI: 10.1021/ja00252a049.
- [19] R. Braren, J. Altomonte, M. Settles, F. Neff, I. Esposito, O. Ebert, M. Schwaiger, E. Rummeny, and A. Steingoetter. “Validation of preclinical multiparametric imaging for prediction of necrosis in hepatocellular carcinoma after embolization”. *Journal of Hepatology*, vol. 55, pp. 1034–1040, 2011. DOI: 10.1016/J.Jhep.2011.01.049.

- [20] K. M. Brindle, S. E. Bohndiek, F. A. Gallagher, and M. I. Kettunen. “Tumor imaging using hyperpolarized ^{13}C magnetic resonance spectroscopy”. *Magnetic Resonance in Medicine*, vol. 66, pp. 505–519, 2011. DOI: 10.1002/mrm.22999.
- [21] C. J. W. Brooks, G. Eglinton, and D. S. Magrill. “The constitution of an oxidation product of β -ionone”. *Journal of the Chemical Society (Resumed)*, pp. 308–310, 1961. DOI: 10.1039/JR9610000308.
- [22] D. J. Brooks, R. P. Beaney, D. G. T. Thomas, J. Marshall, and T. Jons. “Studies on regional cerebral pH in patients with cerebral tumours using continuous inhalation of $^{11}\text{CO}_2$ and positron emission tomography”. *Journal of Cerebral Blood Flow & Metabolism*, vol. 6, pp. 529–535, 1986. DOI: 10.1038/jcbfm.1986.98.
- [23] M. Chan and A. Almutairi. “Nanogels as imaging agents for modalities spanning the electromagnetic spectrum”. *Materials Horizons*, vol. 3, pp. 21–40, 2016. DOI: 10.1039/c5mh00161g.
- [24] J. Chapiro, L. D. Wood, M. Lin, R. Duran, T. Cornish, D. Lesage, V. Charu, R. Scherthaner, Z. Wang, V. Tacher, L. J. Savic, I. R. Kamel, and J. F. Geschwind. “Radiologic-pathologic analysis of contrast-enhanced and diffusion-weighted MR imaging in patients with HCC after TACE: diagnostic accuracy of 3D quantitative image analysis”. *Radiology*, vol. 273, pp. 746–758, 2014. DOI: 10.1148/radiol.14140033.
- [25] L. Q. Chen, C. M. Howison, J. J. Jeffery, I. F. Robey, P. H. Kuo, and M. D. Pagel. “Evaluations of extracellular pH within in vivo tumors using acido-CEST MRI”. *Magnetic Resonance in Medicine*, vol. 72, pp. 1408–1417, 2014. DOI: 10.1002/mrm.25053.
- [26] L. Q. Chen and M. D. Pagel. “Evaluating pH in the extracellular tumor microenvironment using CEST MRI and other imaging methods”. *Advances in Radiology*, vol. 2015, pp. 1–25, 2015. DOI: 10.1155/2015/206405.
- [27] Q. Chen, X. D. Liu, J. W. Chen, J. F. Zeng, Z. P. Cheng, and Z. Liu. “A self-assembled albumin-based nanoprobe for in vivo ratiometric photoacoustic pH imaging”. *Advanced Materials*, vol. 27, pp. 6820–6827, 2015. DOI: 10.1002/adma.201503194.
- [28] E. Chiavazza, E. Kubala, C. V. Gringeri, S. Düwel, M. Durst, R. F. Schulte, and M. I. Menzel. “Earth’s magnetic field enabled scalar coupling relaxation of ^{13}C nuclei bound to fast-relaxing quadrupolar ^{14}N in amide groups”. *Journal of Magnetic Resonance*, vol. 227, pp. 35–38, 2013. DOI: 10.1016/j.jmr.2012.11.016.
- [29] J. Chiche, Y. Le Fur, C. Vilmen, F. Frassinetti, L. Daniel, A. P. Halestrap, P. J. Cozzone, J. Pouyssegur, and N. W. Lutz. “In vivo pH in metabolic-defective ras-transformed fibroblast tumors: key role of the monocarboxylate transporter, MCT4, for inducing an alkaline intracellular pH”. *International Journal of Cancer*, vol. 130, pp. 1511–1520, 2012. DOI: 10.1002/ijc.26125.

- [30] M. R. Clatworthy, M. I. Kettunen, D. E. Hu, R. J. Mathews, T. H. Witney, B. W. C. Kennedy, S. E. Bohndiek, F. A. Gallagher, L. B. Jarvis, K. G. C. Smith, and K. M. Brindle. “Magnetic resonance imaging with hyperpolarized [1,4- $^{13}\text{C}_2$]fumarate allows detection of early renal acute tubular necrosis”. *Proceedings of the National Academy of Sciences of the United States of America*, vol. 109, pp. 13374–13379, 2012. DOI: 10.1073/pnas.1205539109.
- [31] C. H. Cunningham, J. Y. Lau, A. P. Chen, B. J. Geraghty, W. J. Perks, I. Roifman, G. A. Wright, and K. A. Connelly. “Hyperpolarized ^{13}C metabolic MRI of the human heart: Initial experience”. *Circulation Research*, vol. 119, pp. 1177–1182, 2016. DOI: 10.1161/CIRCRESAHA.116.309769.
- [32] M. M. Darpolor, D. E. Kaplan, P. L. Pedersen, and J. D. Glickson. “Human hepatocellular carcinoma metabolism: imaging by hyperpolarized ^{13}C magnetic resonance spectroscopy”. *Journal of Liver: Disease & Transplantation*, vol. 1, pp. 1–7, 2012. DOI: 10.4172/2325-9612.1000101.
- [33] M. M. Darpolor, Y. F. Yen, M. S. Chua, L. Xing, R. H. Clarke-Katzenberg, W. Shi, D. Mayer, S. Josan, R. E. Hurd, A. Pfefferbaum, L. Senadheera, S. So, L. V. Hofmann, G. M. Glazer, and D. M. Spielman. “In vivo MRSI of hyperpolarized [1- ^{13}C]pyruvate metabolism in rat hepatocellular carcinoma”. *NMR in Biomedicine*, vol. 24, pp. 506–513, 2011. DOI: 10.1002/nbm.1616.
- [34] S. E. Day, M. I. Kettunen, M. K. Cherukuri, J. B. Mitchell, M. J. Lizak, H. D. Morris, S. Matsumoto, A. P. Koretsky, and K. M. Brindle. “Detecting response of rat C6 glioma tumors to radiotherapy using hyperpolarized [1- ^{13}C]pyruvate and ^{13}C magnetic resonance spectroscopic imaging”. *Magnetic Resonance in Medicine*, vol. 65, pp. 557–563, 2011. DOI: 10.1002/mrm.22698.
- [35] S. E. Day, M. I. Kettunen, F. A. Gallagher, D. E. Hu, M. Lerche, J. Wolber, K. Golman, J. H. Ardenkjaer-Larsen, and K. M. Brindle. “Detecting tumor response to treatment using hyperpolarized ^{13}C magnetic resonance imaging and spectroscopy”. *Nature Medicine*, vol. 13, pp. 1382–1387, 2007. DOI: 10.1038/nm1650.
- [36] N. C. Deliolanis, R. Kasmieh, T. Wurdinger, B. A. Tannous, K. Shah, and V. Ntziachristos. “Performance of the red-shifted fluorescent proteins in deep-tissue molecular imaging applications”. *Journal of Biomedical Optics*, vol. 13, p. 044008, 2008. DOI: 10.1117/1.2967184.
- [37] D. Delli Castelli, G. Ferrauto, J. C. Cutrin, E. Terreno, and S. Aime. “In vivo maps of extracellular pH in murine melanoma by CEST-MRI”. *Magnetic Resonance in Medicine*, vol. 71, pp. 326–332, 2014. DOI: 10.1002/mrm.24664.
- [38] D. W. Demoin, L. C. Wyatt, K. J. Edwards, D. Abdel-Atti, M. Sarparanta, J. Pourat, V. A. Longo, S. D. Carlin, D. M. Engelman, O. A. Andreev, Y. K. Reshetnyak, N. Viola-Villegas, and J. S. Lewis. “PET imaging of extracellular pH in tumors with ^{64}Cu - and ^{18}F -labeled pHLIP peptides: a structure-activity optimization study”. *Bioconjugate Chemistry*, vol. 27, pp. 2014–2023, 2016. DOI: 10.1021/acs.bioconjchem.6b00306.

- [39] K. Derby, J. Tropp, and C. Hawryszko. “Design and evaluation of a novel dual-tuned resonator for spectroscopic imaging”. *Journal of Magnetic Resonance*, vol. 86, pp. 645–651, 1990. DOI: 10.1016/0022-2364(90)90043-9.
- [40] M. Durst, U. Koellisch, A. Frank, G. Rancan, C. V. Gringeri, V. Karas, F. Wiesinger, M. I. Menzel, M. Schwaiger, A. Haase, and R. F. Schulte. “Comparison of acquisition schemes for hyperpolarised ^{13}C imaging”. *NMR in Biomedicine*, vol. 28, pp. 715–725, 2015. DOI: 10.1002/nbm.3301.
- [41] M. Durst, U. Koellisch, C. Gringeri, M. A. Janich, G. Rancan, A. Frank, F. Wiesinger, M. I. Menzel, A. Haase, and R. F. Schulte. “Bolus tracking for improved metabolic imaging of hyperpolarised compounds”. *Journal of Magnetic Resonance*, vol. 243, pp. 40–46, 2014. DOI: 10.1016/j.jmr.2014.02.011.
- [42] T. C. Eisenschmid, R. U. Kirss, P. P. Deutsch, S. I. Hommeltoft, R. Eisenberg, J. Bargon, R. G. Lawler, and A. L. Balch. “Parahydrogen induced polarization in hydrogenation reactions”. *Journal of the American Chemical Society*, vol. 109, pp. 8089–8091, 1987. DOI: 10.1021/ja00260a026.
- [43] J. A. Fessler. “On NUFFT-based gridding for non-Cartesian MRI”. *Journal of Magnetic Resonance*, vol. 188, pp. 191–195, 2007. DOI: 10.1016/j.jmr.2007.06.012.
- [44] R. R. Flavell, C. von Morze, J. E. Blecha, D. E. Korenchan, M. van Criekinge, R. Sriram, J. W. Gordon, H. Y. Chen, S. Subramaniam, R. A. Bok, Z. J. Wang, D. B. Vigneron, P. E. Larson, J. Kurhanewicz, and D. M. Wilson. “Application of Good’s buffers to pH imaging using hyperpolarized ^{13}C MRI”. *Chemical Communications*, vol. 51, pp. 14119–14122, 2015. DOI: 10.1039/c5cc05348j.
- [45] R. R. Flavell, C. Truillet, M. K. Regan, T. Ganguly, J. E. Blecha, J. Kurhanewicz, H. F. VanBrocklin, K. R. Keshari, C. J. Chang, M. J. Evans, and D. M. Wilson. “Caged [^{18}F]FDG glycosylamines for imaging acidic tumor microenvironments using positron emission tomography”. *Bioconjugate Chemistry*, vol. 27, pp. 170–178, 2016. DOI: 10.1021/acs.bioconjchem.5b00584.
- [46] A. Forner, J. M. Llovet, and J. Bruix. “Hepatocellular carcinoma”. *Lancet*, vol. 379, pp. 1245–1255, 2012. DOI: 10.1016/S0140-6736(11)61347-0.
- [47] L. Frullano, C. Catana, T. Benner, A. D. Sherry, and P. Caravan. “Bimodal MR-PET agent for quantitative pH imaging”. *Angewandte Chemie – International Edition*, vol. 49, pp. 2382–2384, 2010. DOI: 10.1002/anie.201000075.
- [48] F. A. Gallagher, M. I. Kettunen, and K. M. Brindle. “Biomedical applications of hyperpolarized ^{13}C magnetic resonance imaging”. *Progress in Nuclear Magnetic Resonance Spectroscopy*, vol. 55, pp. 285–295, 2009. DOI: 10.1016/j.pnmrs.2009.06.001.
- [49] F. A. Gallagher, M. I. Kettunen, and K. M. Brindle. “Imaging pH with hyperpolarized ^{13}C ”. *NMR in Biomedicine*, vol. 24, pp. 1006–1015, 2011. DOI: 10.1002/nbm.1742.

- [50] F. A. Gallagher, M. I. Kettunen, S. E. Day, D. E. Hu, J. H. Ardenkjaer-Larsen, R. in 't Zandt, P. R. Jensen, M. Karlsson, K. Golman, M. H. Lerche, and K. M. Brindle. "Magnetic resonance imaging of pH in vivo using hyperpolarized ^{13}C -labelled bicarbonate". *Nature*, vol. 453, pp. 940–943, 2008. DOI: 10.1038/nature07017.
- [51] F. A. Gallagher, M. I. Kettunen, D. E. Hu, P. R. Jensen, R. in 't Zandt, M. Karlsson, A. Gisselsson, S. K. Nelson, T. H. Witney, S. E. Bohndiek, G. Hansson, T. Peitersen, M. H. Lerche, and K. M. Brindle. "Production of hyperpolarized $[1,4-^{13}\text{C}_2]$ malate from $[1,4-^{13}\text{C}_2]$ fumarate is a marker of cell necrosis and treatment response in tumors". *Proceedings of the National Academy of Sciences of the United States of America*, vol. 106, pp. 19801–19806, 2009. DOI: 10.1073/pnas.0911447106.
- [52] Walther Gerlach and Otto Stern. "Der experimentelle Nachweis der Richtungsquantelung im Magnetfeld". *Zeitschrift für Physik*, vol. 9, pp. 349–352, 1922. DOI: 10.1007/bf01326983.
- [53] R. K. Ghosh, S. J. Kadlecik, M. Pourfathi, and R. R. Rizi. "Efficient production of hyperpolarized bicarbonate by chemical reaction on a DNP precursor to measure pH". *Magnetic Resonance in Medicine*, vol. 74, pp. 1406–1413, 2015. DOI: 10.1002/mrm.25530.
- [54] R. J. Gillies, Z. Liu, and Z. Bhujwala. " ^{31}P -MRS measurements of extracellular pH of tumors using 3-aminopropylphosphonate". *American Journal of Physiology*, vol. 267, pp. C195–C203, 1994.
- [55] R. J. Gillies and D. L. Morse. "In vivo magnetic resonance spectroscopy in cancer". *Annual Review of Biomedical Engineering*, vol. 7, pp. 287–326, 2005. DOI: 10.1146/annurev.bioeng.7.060804.100411.
- [56] R. J. Gillies, N. Raghunand, M. L. Garcia-Martin, and R. A. Gatenby. "pH imaging. A review of pH measurement methods and applications in cancers". *IEEE Engineering in Medicine and Biology Magazine*, vol. 23, pp. 57–64, 2004. DOI: 10.1109/MEMB.2004.1360409.
- [57] R. J. Gillies, N. Raghunand, G. S. Karczmar, and Z. M. Bhujwala. "MRI of the tumor microenvironment". *Journal of Magnetic Resonance Imaging*, vol. 16, pp. 430–450, 2002. DOI: 10.1002/jmri.10181.
- [58] K. Golman, R. in 't Zandt, M. Lerche, R. Pehrson, and J. H. Ardenkjaer-Larsen. "Metabolic imaging by hyperpolarized ^{13}C magnetic resonance imaging for in vivo tumor diagnosis". *Cancer Research*, vol. 66, pp. 10855–10860, 2006. DOI: 10.1158/0008-5472.CAN-06-2564.
- [59] R. A. de Graaf. *In vivo NMR spectroscopy: principles and techniques*. 2nd ed. Chichester, UK: John Wiley & Sons, 2007, pp. 78–82. DOI: 10.1002/9780470512968.
- [60] R. A. Graham, A. H. Taylor, and T. R. Brown. "A method for calculating the distribution of pH in tissues and a new source of pH error from the ^{31}P -NMR spectrum". *American Journal of Physiology*, vol. 266, R638–R645, 1994.

- [61] J. L. Griffin, H. Atherton, J. Shockcor, and L. Atzori. “Metabolomics as a tool for cardiac research”. *Nature Reviews Cardiology*, vol. 8, pp. 630–643, 2011. DOI: 10.1038/nrcardio.2011.138.
- [62] J. R. Griffiths, A. N. Stevens, R. A. Iles, R. E. Gordon, and D. Shaw. “³¹P-NMR investigation of solid tumours in the living rat”. *Bioscience Reports*, vol. 1, pp. 319–325, 1981. DOI: 10.1007/BF01114871.
- [63] E. M. Haacke, R. W. Brown, M. R. Thompson, and R. Venkatesan. *Magnetic Resonance Imaging: Physical Principles and Sequence Design*. John Wiley & Sons, 1999. ISBN: 9780471351283.
- [64] E. L. Hahn. “Spin echoes”. *Physical Review*, vol. 80, pp. 580–594, 1950. DOI: 10.1103/PhysRev.80.580.
- [65] A. I. Hashim, X. Zhang, J. W. Wojtkowiak, G. V. Martinez, and R. J. Gillies. “Imaging pH and metastasis”. *NMR in Biomedicine*, vol. 24, pp. 582–591, 2011. DOI: 10.1002/nbm.1644.
- [66] M. Hassan, J. Riley, V. Chernomordik, P. Smith, R. Pursley, S. B. Lee, J. Capala, and A. H. Gandjbakhche. “Fluorescence lifetime imaging system for in vivo studies”. *Molecular Imaging*, vol. 6, pp. 229–236, 2007. DOI: 10.2310/7290.2007.00019.
- [67] S. Hu, A. Balakrishnan, R. A. Bok, B. Anderton, P. E. Z. Larson, S. J. Nelson, J. Kurhanewicz, D. B. Vigneron, and A. Goga. “¹³C Pyruvate imaging reveals alterations in glycolysis that precede c-Myc-induced tumor formation and regression”. *Cell Metabolism*, vol. 14, pp. 131–142, 2011. DOI: 10.1016/j.cmet.2011.04.012.
- [68] Edward David Hughes and Herbert Ben Watson. “The reaction of bromine with aliphatic acids. Part III. α - and γ -ketonic acids”. *Journal of the Chemical Society (Resumed)*, pp. 1945–1954, 1929. DOI: 10.1039/JR9290001945.
- [69] C. Hundshammer, S. Düwel, and F. Schilling. “Imaging of extracellular pH using hyperpolarized molecules”. *Israel Journal of Chemistry*, vol. 57, pp. 788–799, 2017. DOI: 10.1002/ijch.201700017.
- [70] S. Hunjan, R. P. Mason, V. D. Mehta, P. V. Kulkarni, S. Aravind, V. Arora, and P. P. Antich. “Simultaneous intracellular and extracellular pH measurement in the heart by ¹⁹F-NMR of 6-fluoropyridoxol”. *Magnetic Resonance in Medicine*, vol. 39, pp. 551–556, 1998. DOI: 10.1002/mrm.1910390407.
- [71] R. E. Hurd, Y. F. Yen, A. Chen, and J. H. Ardenkjaer-Larsen. “Hyperpolarized ¹³C metabolic imaging using dissolution dynamic nuclear polarization”. *Journal of Magnetic Resonance Imaging*, vol. 36, pp. 1314–1328, 2012. DOI: 10.1002/Jmri.23753.
- [72] T. L. Hwang, P. C. M. van Zijl, and S. Mori. “Accurate quantitation of water-amide proton exchange rates using the Phase-Modulated CLEAN chemical EXchange (CLEANEX-PM) approach with a Fast-HSQC (FHSQC) detection scheme”. *Journal of Biomolecular NMR*, vol. 11, pp. 221–226, 1998. DOI: 10.1023/A:1008276004875.

- [73] P. R. Jensen, T. Peitersen, M. Karlsson, R. in 't Zandt, A. Gisselsson, G. Hansson, S. Meier, and M. H. Lerche. "Tissue-specific short chain fatty acid metabolism and slow metabolic recovery after ischemia from hyperpolarized NMR in vivo". *Journal of Biological Chemistry*, vol. 284, pp. 36077–36082, 2009. DOI: 10.1074/jbc.M109.066407.
- [74] W. Jiang, L. Lumata, W. Chen, S. Zhang, Z. Kovacs, A. D. Sherry, and C. Khemtong. "Hyperpolarized ^{15}N -pyridine derivatives as pH-sensitive MRI agents". *Scientific Reports*, vol. 5, p. 9104, 2015. DOI: 10.1038/srep09104.
- [75] A. K. Jindal, M. E. Merritt, E. H. Suh, C. R. Malloy, A. D. Sherry, and Z. Kovacs. "Hyperpolarized ^{89}Y -complexes as pH sensitive NMR probes". *Journal of the American Chemical Society*, vol. 132, pp. 1784–1785, 2010. DOI: 10.1021/ja910278e.
- [76] A. W. K. de Jong. "L'action de l'acide chlorhydrique sur l'acide pyruvique. (Premier Mémoire)". *Recueil des Travaux Chimiques des Pays-Bas et de la Belgique*, vol. 20, pp. 81–101, 1901. DOI: 10.1002/rec1.19010200303.
- [77] A. W. K. de Jong. "Les transformations des sels de l'acide pyruvique. (Quatrième Mémoire)". *Recueil des Travaux Chimiques des Pays-Bas et de la Belgique*, vol. 25, pp. 229–232, 1906. DOI: 10.1002/rec1.19060250703.
- [78] S. Kadlecak, H. Shaghghi, S. Siddiqui, H. Profka, M. Pourfathi, and R. Rizi. "The effect of exogenous substrate concentrations on true and apparent metabolism of hyperpolarized pyruvate in the isolated perfused lung". *NMR in Biomedicine*, vol. 27, pp. 1557–1570, 2014. DOI: 10.1002/nbm.3219.
- [79] Y. Kato, S. Ozawa, C. Miyamoto, Y. Maehata, A. Suzuki, T. Maeda, and Y. Baba. "Acidic extracellular microenvironment and cancer". *Cancer Cell International*, vol. 13, pp. 1–8, 2013. DOI: 10.1186/1475-2867-13-89.
- [80] K. J. Kearfott, L. Junck, and D. A. Rottenberg. " ^{11}C -Dimethylloxazolidinedione (DMO) - biodistribution, radiation absorbed dose, and potential for PET measurement of regional brain pH". *Journal of Nuclear Medicine*, vol. 24, pp. 805–811, 1983.
- [81] J. Keeler. *Understanding NMR Spectroscopy*. 2nd ed. John Wiley & Sons, 2011. ISBN: 9781119964933.
- [82] K. R. Keshari and D. M. Wilson. "Chemistry and biochemistry of ^{13}C hyperpolarized magnetic resonance using dynamic nuclear polarization". *Chemical Society Reviews*, vol. 43, pp. 1627–1659, 2014. DOI: 10.1039/c3cs60124b.
- [83] O. Khagai, R. F. Schulte, M. A. Janich, M. I. Menzel, E. Farrell, A. M. Otto, J. H. Ardenkjaer-Larsen, S. J. Glaser, A. Haase, M. Schwaiger, and F. Wiesinger. "Apparent rate constant mapping using hyperpolarized $[1-^{13}\text{C}]$ -pyruvate". *NMR in Biomedicine*, vol. 27, pp. 1256–1265, 2014. DOI: 10.1002/nbm.3174.
- [84] R. U. Kirss, T. C. Eisenschmid, and R. Eisenberg. "Parahydrogen induced polarization in hydrogenation reactions catalyzed by ruthenium phosphine complexes". *Journal of the American Chemical Society*, vol. 110, pp. 8564–8566, 1988. DOI: 10.1021/ja00233a053.

- [85] D. E. Korenchan, R. R. Flavell, C. Baligand, R. Sriram, K. Neumann, S. Sukumar, H. VanBrocklin, D. B. Vigneron, D. M. Wilson, and J. Kurhanewicz. “Dynamic nuclear polarization of biocompatible ^{13}C -enriched carbonates for in vivo pH imaging”. *Chemical Communications*, vol. 52, pp. 3030–3033, 2016. DOI: 10.1039/c5cc09724j.
- [86] D. E. Korenchan, C. Taglang, C. von Morze, J. E. Blecha, J. W. Gordon, R. Sriram, P. E. Z. Larson, D. B. Vigneron, H. F. VanBrocklin, J. Kurhanewicz, D. M. Wilson, and R. R. Flavell. “Dicarboxylic acids as pH sensors for hyperpolarized ^{13}C magnetic resonance spectroscopic imaging”. *Analyst*, vol. 142, pp. 1429–1433, 2017. DOI: 10.1039/c7an00076f.
- [87] R. W. von Korff. “ ^{14}C -Pyruvate, purity and stability”. *Analytical Biochemistry*, vol. 8, pp. 171–178, 1964. DOI: 10.1016/0003-2697(64)90043-0.
- [88] D. J. Kushner, A. Baker, and T. G. Dunstall. “Pharmacological uses and perspectives of heavy water and deuterated compounds”. *Canadian Journal of Physiology and Pharmacology*, vol. 77, pp. 79–88, 1999. DOI: 10.1139/y99-005.
- [89] P. E. Larson, A. B. Kerr, A. P. Chen, M. S. Lustig, M. L. Zierhut, S. Hu, C. H. Cunningham, J. M. Pauly, J. Kurhanewicz, and D. B. Vigneron. “Multiband excitation pulses for hyperpolarized ^{13}C dynamic chemical-shift imaging”. *Journal of Magnetic Resonance*, vol. 194, pp. 121–127, 2008. DOI: 10.1016/j.jmr.2008.06.010.
- [90] J. H. Lee, J. Y. Park, D. Y. Kim, S. H. Ahn, K. H. Han, H. J. Seo, J. D. Lee, and H. J. Choi. “Prognostic value of ^{18}F -FDG PET for hepatocellular carcinoma patients treated with sorafenib”. *Liver International*, vol. 31, pp. 1144–1149, 2011. DOI: 10.1111/j.1478-3231.2011.02541.x.
- [91] M. H. Levitt. *Spin Dynamics: Basics of Nuclear Magnetic Resonance*. 2nd ed. John Wiley & Sons, 2013. ISBN: 9781118681848.
- [92] E. Liepinsh and G. Otting. “Proton exchange rates from amino acid side chains – implications for image contrast”. *Magnetic Resonance in Medicine*, vol. 35, pp. 30–42, 1996. DOI: 10.1002/mrm.1910350106.
- [93] D. Ling, W. Park, S. J. Park, Y. Lu, K. S. Kim, M. J. Hackett, B. H. Kim, H. Yim, Y. S. Jeon, K. Na, and T. Hyeon. “Multifunctional tumor pH-sensitive self-assembled nanoparticles for bimodal imaging and treatment of resistant heterogeneous tumors”. *Journal of the American Chemical Society*, vol. 136, pp. 5647–5655, 2014. DOI: 10.1021/ja4108287.
- [94] J. M. Llovet, A. Burroughs, and J. Bruix. “Hepatocellular carcinoma”. *Lancet*, vol. 362, pp. 1907–1917, 2003. DOI: 10.1016/S0140-6736(03)14964-1.
- [95] J. M. Llovet, A. M. Di Bisceglie, J. Bruix, B. S. Kramer, R. Lencioni, A. X. Zhu, M. Sherman, M. Schwartz, M. Lotze, J. Talwalkar, and G. J. Gores for the Panel of Experts in HCC-Design Clinical Trials. “Design and endpoints of clinical trials in hepatocellular carcinoma”. *Journal of the National Cancer Institute*, vol. 100, pp. 698–711, 2008. DOI: 10.1093/jnci/djn134.

- [96] J. M. Llovet, S. Ricci, V. Mazzaferro, P. Hilgard, E. Gane, J. F. Blanc, A. C. de Oliveira, A. Santoro, J. L. Raoul, A. Forner, M. Schwartz, C. Porta, S. Zeuzem, L. Bolondi, T. F. Greten, P. R. Galle, J. F. Seitz, I. Borbath, D. Haussinger, T. Giannaris, M. Shan, M. Moscovici, D. Voliotis, and J. Bruix for the Sharp Investigators Study Group. “Sorafenib in advanced hepatocellular carcinoma”. *New England Journal of Medicine*, vol. 359, pp. 378–390, 2008. DOI: 10.1056/NEJMoa0708857.
- [97] D. L. Longo, W. Dastru, G. Digilio, J. Keupp, S. Langereis, S. Lanzardo, S. Prestigio, O. Steinbach, E. Terreno, F. Uggeri, and S. Aime. “Iopamidol as a responsive MRI-chemical exchange saturation transfer contrast agent for pH mapping of kidneys: in vivo studies in mice at 7 T”. *Magnetic Resonance in Medicine*, vol. 65, pp. 202–211, 2011. DOI: 10.1002/mrm.22608.
- [98] D. L. Longo, P. Z. Sun, L. Consolino, F. C. Michelotti, F. Uggeri, and S. Aime. “A general MRI-CEST ratiometric approach for pH imaging: demonstration of in vivo pH mapping with iobitridol”. *Journal of the American Chemical Society*, vol. 136, pp. 14333–14336, 2014. DOI: 10.1021/ja5059313.
- [99] M. P. Lowe, D. Parker, O. Reany, S. Aime, M. Botta, G. Castellano, E. Gianolio, and R. Pagliarin. “pH-dependent modulation of relaxivity and luminescence in macrocyclic gadolinium and europium complexes based on reversible intramolecular sulfonamide ligation”. *Journal of the American Chemical Society*, vol. 123, pp. 7601–7609, 2001. DOI: 10.1021/ja0103647.
- [100] N. W. Lutz, Y. Le Fur, J. Chiche, J. Pouyssegur, and P. J. Cozzone. “Quantitative in vivo characterization of intracellular and extracellular pH profiles in heterogeneous tumors: a novel method enabling multiparametric pH analysis”. *Cancer Research*, vol. 73, pp. 4616–4628, 2013. DOI: 10.1158/0008-5472.CAN-13-0767.
- [101] S. Macholl, M. S. Morrison, P. Iveson, B. E. Arbo, O. A. Andreev, Y. K. Reshetnyak, D. M. Engelman, and E. Johannesen. “In vivo pH imaging with ^{99m}Tc -pHLIP”. *Molecular Imaging and Biology*, vol. 14, pp. 725–734, 2012. DOI: 10.1007/s11307-012-0549-z.
- [102] S. G. Mallat and Z. F. Zhang. “Matching pursuits with time-frequency dictionaries”. *IEEE Transactions on Signal Processing*, vol. 41, pp. 3397–3415, 1993. DOI: 10.1109/78.258082.
- [103] I. Marco-Rius, M. C. D. Tayler, M. I. Kettunen, T. J. Larkin, K. N. Timm, E. M. Serrao, T. B. Rodrigues, G. Pileio, J. H. Ardenkjaer-Larsen, M. H. Levitt, and K. M. Brindle. “Hyperpolarized singlet lifetimes of pyruvate in human blood and in the mouse”. *NMR in Biomedicine*, vol. 26, pp. 1696–1704, 2013. DOI: 10.1002/nbm.3005.
- [104] L. Marelli, R. Stigliano, C. Triantos, M. Senzolo, E. Cholongitas, N. Davies, J. Tibballs, T. Meyer, D. W. Patch, and A. K. Burroughs. “Transarterial therapy for hepatocellular carcinoma: Which technique is more effective? A systematic review of cohort and randomized studies”. *CardioVascular and Interventional Radiology*, vol. 30, pp. 6–25, 2007. DOI: 10.1007/s00270-006-0062-3.

- [105] S. A. Margolis and B. Coxon. “Identification and quantitation of the impurities in sodium pyruvate”. *Analytical Chemistry*, vol. 58, pp. 2504–2510, 1986. DOI: 10.1021/ac00125a033.
- [106] M. Mayr, F. Burkhalter, and G. Bongartz. “Nephrogenic systemic fibrosis: clinical spectrum of disease”. *Journal of Magnetic Resonance Imaging*, vol. 30, pp. 1289–1297, 2009. DOI: 10.1002/jmri.21975.
- [107] N. McVicar, A. X. Li, M. Suchý, R. H. Hudson, R. S. Menon, and R. Bartha. “Simultaneous in vivo pH and temperature mapping using a PARACEST-MRI contrast agent”. *Magnetic Resonance in Medicine*, vol. 70, pp. 1016–1025, 2013. DOI: 10.1002/mrm.24539.
- [108] P. Melnikov and L. Z. Zanon. “Clinical effects of cesium intake”. *Biological Trace Element Research*, vol. 135, pp. 1–9, 2010. DOI: 10.1007/s12011-009-8486-7.
- [109] L. Mignon, P. Dutta, G. V. Martinez, P. Foroutan, R. J. Gillies, and B. F. Jordan. “Monitoring chemotherapeutic response by hyperpolarized ^{13}C -fumarate MRS and diffusion MRI”. *Cancer Research*, vol. 74, pp. 686–694, 2014. DOI: 10.1158/0008-5472.CAN-13-1914.
- [110] M. Mikawa, N. Miwa, M. Brautigam, T. Akaike, and A. Maruyama. “ Gd^{3+} -loaded polyion complex for pH depiction with magnetic resonance imaging”. *Journal of Biomedical Materials Research*, vol. 49, pp. 390–395, 2000. DOI: 10.1002/(SICI)1097-4636(20000305)49:3<390::AID-JBM12>3.0.CO;2-Q.
- [111] C. M. Montgomery, A. S. Fairhurst, and J. L. Webb. “Metabolic studies on heart mitochondria. III. The action of parapyruvate on alpha-ketoglutaric oxidase”. *Journal of Biological Chemistry*, vol. 221, pp. 369–376, 1956.
- [112] C. M. Montgomery and J. L. Webb. “Detection of a new inhibitor of the tricarboxylic acid cycle”. *Science*, vol. 120, pp. 843–844, 1954. DOI: 10.1126/science.120.3125.843.
- [113] C. M. Montgomery and J. L. Webb. “Metabolic studies on heart mitochondria. II. The inhibitory action of parapyruvate on the tricarboxylic acid cycle”. *Journal of Biological Chemistry*, vol. 221, pp. 359–68, 1956.
- [114] B. F. Moon, K. M. Jones, L. Q. Chen, P. L. Liu, E. A. Randtke, C. M. Howison, and M. D. Pagel. “A comparison of iopromide and iopamidol, two acidoCEST MRI contrast media that measure tumor extracellular pH”. *Contrast Media & Molecular Imaging*, vol. 10, pp. 446–455, 2015. DOI: 10.1002/cmri.1647.
- [115] R. B. Moon and J. H. Richards. “Determination of intracellular pH by ^{31}P magnetic resonance”. *Journal of Biological Chemistry*, vol. 248, pp. 7276–7278, 1973.
- [116] C. von Morze, P. E. Z. Larson, S. Hu, K. Keshari, D. M. Wilson, J. H. Ardenkjaer-Larsen, A. Goga, R. Bok, J. Kurhanewicz, and D. B. Vigneron. “Imaging of blood flow using hyperpolarized ^{13}C urea in preclinical cancer models”. *Journal of Magnetic Resonance Imaging*, vol. 33, pp. 692–697, 2011. DOI: 10.1002/jmri.22484.

- [117] C. von Morze, P. E. Z. Larson, S. Hu, H. A. I. Yoshihara, R. A. Bok, A. Goga, J. H. Ardenkjaer-Larsen, and D. B. Vigneron. “Investigating tumor perfusion and metabolism using multiple hyperpolarized ^{13}C compounds: HP001, pyruvate and urea”. *Magnetic Resonance Imaging*, vol. 20, pp. 305–311, 2012. DOI: 10.1016/j.mri.2011.09.026.
- [118] M. Nakanishi, M. Chuma, S. Hige, T. Omatsu, H. Yokoo, K. Nakanishi, T. Kamiyama, K. Kubota, H. Haga, Y. Matsuno, Y. Onodera, M. Kato, and M. Asaka. “Relationship between diffusion-weighted magnetic resonance imaging and histological tumor grading of hepatocellular carcinoma”. *Annals of Surgical Oncology*, vol. 19, pp. 1302–1309, 2012. DOI: 10.1245/s10434-011-2066-8.
- [119] K. Nath, D. S. Nelson, A. M. Ho, S. C. Lee, M. M. Darpolor, S. Pickup, R. Zhou, D. F. Heitjan, D. B. Leeper, and J. D. Glickson. “ ^{31}P and ^1H MRS of DB-1 melanoma xenografts: lonidamine selectively decreases tumor intracellular pH and energy status and sensitizes tumors to melphalan”. *NMR in Biomedicine*, vol. 26, pp. 98–105, 2013. DOI: 10.1002/nbm.2824.
- [120] S. J. Nelson, J. Kurhanewicz, D. B. Vigneron, P. E. Larson, A. L. Harzstark, M. Ferrone, M. van Criekinge, J. W. Chang, R. Bok, I. Park, G. Reed, L. Carvajal, E. J. Small, P. Munster, V. K. Weinberg, J. H. Ardenkjaer-Larsen, A. P. Chen, R. E. Hurd, L. I. Odegardstuen, F. J. Robb, J. Tropp, and J. A. Murray. “Metabolic imaging of patients with prostate cancer using hyperpolarized $[1-^{13}\text{C}]$ pyruvate”. *Science Translational Medicine*, vol. 5, 198ra108, 2013. DOI: 10.1126/scitranslmed.3006070.
- [121] S. J. Nelson, E. Ozhinsky, Y. Li, I. Park, and J. Crane. “Strategies for rapid in vivo ^1H and hyperpolarized ^{13}C MR spectroscopic imaging”. *Journal of Magnetic Resonance*, vol. 229, pp. 187–197, 2013. DOI: 10.1016/j.jmr.2013.02.003.
- [122] P. M. Nielsen, A. Eldirdiri, L. B. Bertelsen, H. S. Jorgensen, J. H. Ardenkjaer-Larsen, and C. Laustsen. “Fumarase activity: an in vivo and in vitro biomarker for acute kidney injury”. *Scientific Reports*, vol. 7, p. 40812, 2017. DOI: 10.1038/srep40812.
- [123] P. Nikolaou, B. M. Goodson, and E. Y. Chekmenev. “NMR hyperpolarization techniques for biomedicine”. *Chemistry – A European Journal*, vol. 21, pp. 3156–3166, 2015. DOI: 10.1002/chem.201405253.
- [124] A. Nishie, T. Tajima, Y. Asayama, K. Ishigami, D. Kakihara, T. Nakayama, Y. Takayama, D. Okamoto, N. Fujita, A. Taketomi, K. Yoshimitsu, and H. Honda. “Diagnostic performance of apparent diffusion coefficient for predicting histological grade of hepatocellular carcinoma”. *European Journal of Radiology*, vol. 80, e29–e33, 2011. DOI: 10.1016/j.ejrad.2010.06.019.
- [125] M. Oishi, S. Sumitani, and Y. Nagasaki. “On-off regulation of ^{19}F magnetic resonance signals based on pH-Sensitive PEGylated nanogels for potential tumor-specific smart ^{19}F MRI probes”. *Bioconjugate Chemistry*, vol. 18, pp. 1379–1382, 2007. DOI: 10.1021/bc7002154.

- [126] A. S. Ojugo, P. M. McSheehy, D. J. McIntyre, C. McCoy, M. Stubbs, M. O. Leach, I. R. Judson, and J. R. Griffiths. “Measurement of the extracellular pH of solid tumours in mice by magnetic resonance spectroscopy: a comparison of exogenous ^{19}F and ^{31}P probes”. *NMR in Biomedicine*, vol. 12, pp. 495–504, 1999. DOI: 10.1002/(SICI)1099-1492(199912)12:8<495::AID-NBM594>3.0.CO;2-K.
- [127] J. M. Park, L. D. Recht, S. Josan, M. Merchant, T. Jang, Y. F. Yen, R. E. Hurd, D. M. Spielman, and D. Mayer. “Metabolic response of glioma to dichloroacetate measured in vivo by hyperpolarized ^{13}C magnetic resonance spectroscopic imaging”. *Neuro-Oncology*, vol. 15, pp. 433–441, 2013. DOI: 10.1093/neuonc/nos319.
- [128] H. Pelicano, D. S. Martin, R. H. Xu, and P. Huang. “Glycolysis inhibition for anticancer treatment”. *Oncogene*, vol. 25, pp. 4633–4646, 2006. DOI: 10.1038/sj.onc.1209597.
- [129] R. J. Perkins, R. K. Shoemaker, B. K. Carpenter, and V. Vaida. “Chemical equilibria and kinetics in aqueous solutions of zymonic acid”. *The Journal of Physical Chemistry A*, vol. 120, pp. 10096–10107, 2016. DOI: 10.1021/acs.jpca.6b10526.
- [130] V. Prey, E. Waldmann, and H. Berbalk. “Zur Kenntnis der Brenztraubensäure”. *Monatshefte für Chemie und verwandte Teile anderer Wissenschaften*, vol. 86, pp. 408–413, 1955. DOI: 10.1007/BF00903624.
- [131] P. Provent, M. Benito, B. Hiba, R. Farion, P. Lopez-Larrubia, P. Ballesteros, C. Remy, C. Segebarth, S. Cerdan, J. A. Coles, and M. L. Garcia-Martin. “Serial in vivo spectroscopic nuclear magnetic resonance imaging of lactate and extracellular pH in rat gliomas shows redistribution of protons away from sites of glycolysis”. *Cancer Research*, vol. 67, pp. 7638–7645, 2007. DOI: 10.1158/0008-5472.CAN-06-3459.
- [132] E. M. Purcell, H. C. Torrey, and R. V. Pound. “Resonance absorption by nuclear magnetic moments in a solid”. *Physical Review*, vol. 69, pp. 37–38, 1946. DOI: 10.1103/PhysRev.69.37.
- [133] N. Raghunand, C. Howison, A. D. Sherry, S. Zhang, and R. J. Gillies. “Renal and systemic pH imaging by contrast-enhanced MRI”. *Magnetic Resonance in Medicine*, vol. 49, pp. 249–257, 2003. DOI: 10.1002/mrm.10347.
- [134] R. J. Rapf, R. J. Perkins, B. K. Carpenter, and V. Vaida. “Mechanistic description of photochemical oligomer formation from aqueous pyruvic acid”. *The Journal of Physical Chemistry A*, vol. 121, pp. 4272–4282, 2017. DOI: 10.1021/acs.jpca.7b03310.
- [135] A. E. Reed Harris, A. Pajunoja, M. Cazaunau, A. Gratien, E. Pangui, A. Monod, E. C. Griffith, A. Virtanen, J. F. Doussin, and V. Vaida. “Multiphase photochemistry of pyruvic acid under atmospheric conditions”. *The Journal of Physical Chemistry A*, vol. 121, pp. 3327–3339, 2017. DOI: 10.1021/acs.jpca.7b01107.

- [136] G. D. Reed, C. von Morze, R. Bok, B. L. Koelsch, M. Van Criekinge, K. J. Smith, H. Shang, P. E. Larson, J. Kurhanewicz, and D. B. Vigneron. “High resolution ^{13}C MRI with hyperpolarized urea: in vivo T_2 mapping and ^{15}N labeling effects”. *IEEE Transactions on Medical Imaging*, vol. 33, pp. 362–371, 2014. DOI: 10.1109/TMI.2013.2285120.
- [137] S. B. Reeder, J. H. Brittain, T. M. Grist, and Y. F. Yen. “Least-squares chemical shift separation for ^{13}C metabolic imaging”. *Journal of Magnetic Resonance Imaging*, vol. 26, pp. 1145–1152, 2007. DOI: 10.1002/Jmri.21089.
- [138] F. Reineri, T. Boi, and S. Aime. “Parahydrogen induced polarization of ^{13}C carboxylate resonance in acetate and pyruvate”. *Nature Communications*, vol. 6, p. 5858, 2015. DOI: 10.1038/ncomms6858.
- [139] B. A. Riggle, Y. F. Wang, and I. J. Dmochowski. “A ‘smart’ ^{129}Xe -NMR biosensor for pH-dependent cell labeling”. *Journal of the American Chemical Society*, vol. 137, pp. 5542–5548, 2015. DOI: 10.1021/jacs.5b01938.
- [140] P. B. Roemer, W. A. Edelstein, C. E. Hayes, S. P. Souza, and O. M. Mueller. “The NMR phased array”. *Magnetic Resonance in Medicine*, vol. 16, pp. 192–225, 1990. DOI: 10.1002/mrm.1910160203.
- [141] D. A. Rottenberg, J. Z. Ginos, K. J. Kearfott, L. Junck, V. Dhawan, and J. O. Jarden. “In vivo measurement of brain tumor pH using [^{11}C]DMO and positron emission tomography”. *Annals of Neurology*, vol. 17, pp. 70–79, 1985. DOI: 10.1002/ana.410170116.
- [142] F. Schilling, S. Düwel, U. Köllisch, M. Durst, R. F. Schulte, S. J. Glaser, A. Haase, A. M. Otto, and M. I. Menzel. “Diffusion of hyperpolarized ^{13}C -metabolites in tumor cell spheroids using real-time NMR spectroscopy”. *NMR in Biomedicine*, vol. 26, pp. 557–568, 2013. DOI: 10.1002/nbm.2892.
- [143] D. J. Scholz, M. A. Janich, U. Köllisch, R. F. Schulte, J. H. Ardenkjaer-Larsen, A. Frank, A. Haase, M. Schwaiger, and M. I. Menzel. “Quantified pH imaging with hyperpolarized ^{13}C -bicarbonate”. *Magnetic Resonance in Medicine*, vol. 73, pp. 2274–2282, 2015. DOI: 10.1002/mrm.25357.
- [144] D. J. Scholz, A. M. Otto, J. Hintermair, F. Schilling, A. Frank, U. Köllisch, M. A. Janich, R. F. Schulte, M. Schwaiger, A. Haase, and M. I. Menzel. “Parameterization of hyperpolarized ^{13}C -bicarbonate-dissolution dynamic nuclear polarization”. *Magnetic Resonance Materials in Physics, Biology and Medicine*, vol. 28, pp. 591–598, 2015. DOI: 10.1007/s10334-015-0500-9.
- [145] M. A. Schroeder, P. Swietach, H. J. Atherton, F. A. Gallagher, P. Lee, G. K. Radda, K. Clarke, and D. J. Tyler. “Measuring intracellular pH in the heart using hyperpolarized carbon dioxide and bicarbonate: a ^{13}C and ^{31}P magnetic resonance spectroscopy study”. *Cardiovascular Research*, vol. 86, pp. 82–91, 2010. DOI: 10.1093/cvr/cvp396.
- [146] G. Schwarzenbach and Ch. Wittwer. “Über das Keto-Enol-Gleichgewicht bei cyclischen α -Diketonen”. *Helvetica Chimica Acta*, vol. 30, pp. 663–669, 1947. DOI: 10.1002/hlca.19470300232.

- [147] V. Seshan and N. Bansal. “In vivo ^{31}P and ^{23}Na NMR spectroscopy and imaging”, pp. 557–607. In: *NMR spectroscopy techniques*. Ed. by M. D. Bruch. 2nd ed. New York: Dekker, 1996. ISBN: 0-8247-9450-8.
- [148] R. V. Shchepin, D. A. Barskiy, A. M. Coffey, T. Theis, F. Shi, W. S. Warren, B. M. Goodson, and E. Y. Chekmenev. “ ^{15}N hyperpolarization of imidazole- $^{15}\text{N}_2$ for magnetic resonance pH sensing via SABRE-SHEATH”. *ACS Sensors*, vol. 1, pp. 640–644, 2016. DOI: 10.1021/acssensors.6b00231.
- [149] V. R. Sheth, G. Liu, Y. Li, and M. D. Pagel. “Improved pH measurements with a single PARACEST MRI contrast agent”. *Contrast Media & Molecular Imaging*, vol. 7, pp. 26–34, 2012. DOI: 10.1002/cmmi.460.
- [150] A. Sikka, E. M. E. Barnes, and H. C. Keun. “The role of biophysics and engineering in investigating tumour pH and its regulation”. *Convergent Science Physical Oncology*, vol. 3, p. 013003, 2017. DOI: 10.1088/2057-1739/aa5cd9.
- [151] R. van Sluis, Z. M. Bhujwalla, N. Raghunand, P. Ballesteros, J. Alvarez, S. Cerdan, J. P. Galons, and R. J. Gillies. “In vivo imaging of extracellular pH using ^1H MRSI”. *Magnetic Resonance in Medicine*, vol. 41, pp. 743–750, 1999. DOI: 10.1002/(SICI)1522-2594(199904)41:4<743::AID-MRM13>3.0.CO;2-Z.
- [152] K. Snoussi, J. W. Bulte, M. Gueron, and P. C. M. van Zijl. “Sensitive CEST agents based on nucleic acid imino proton exchange: detection of poly(rU) and of a dendrimer-poly(rU) model for nucleic acid delivery and pharmacology”. *Magnetic Resonance in Medicine*, vol. 49, pp. 998–1005, 2003. DOI: 10.1002/mrm.10463.
- [153] J. Spengler, S. N. Osipov, E. Heistracher, A. Haas, and K. Burger. “Hexafluoroacetone as protecting and activating reagent: reactions of hexafluoroacetone with α -keto acids”. *Journal of Fluorine Chemistry*, vol. 125, pp. 1019–1023, 2004. DOI: 10.1016/j.jfluchem.2004.01.021.
- [154] A. Steingoetter, J. Svensson, Y. Kosanke, R. M. Botnar, M. Schwaiger, E. Rummeny, and R. Braren. “Reference region-based pharmacokinetic modeling in quantitative dynamic contrast-enhanced MRI allows robust treatment monitoring in a rat liver tumor model despite cardiovascular changes”. *Magnetic Resonance in Medicine*, vol. 65, pp. 229–238, 2011. DOI: 10.1002/mrm.22589.
- [155] F. H. Stodola, O. L. Shotwell, and L. B. Lockwood. “Zymonic acid, a new metabolic product of some yeasts grown in aerated culture. I. Structure studies”. *Journal of the American Chemical Society*, vol. 74, pp. 5415–5418, 1952. DOI: 10.1021/ja01141a057.
- [156] T. T. Tapmeier, A. Moshnikova, J. Beech, D. Allen, P. Kinchesh, S. Smart, A. Harris, A. McIntyre, D. M. Engelman, O. A. Andreev, Y. K. Reshetnyak, and R. J. Muschel. “The pH low insertion peptide pHLIP variant 3 as a novel marker of acidic malignant lesions”. *Proceedings of the National Academy of Sciences of the United States of America*, vol. 112, pp. 9710–9715, 2015. DOI: 10.1073/pnas.1509488112.

- [157] T. Theis, M. L. Truong, A. M. Coffey, R. V. Shchepin, K. W. Waddell, F. Shi, B. M. Goodson, W. S. Warren, and E. Y. Chekmenev. “Microtesla SABRE enables 10 % ^{15}N nuclear spin polarization”. *Journal of the American Chemical Society*, vol. 137, pp. 1404–1407, 2015. DOI: 10.1021/ja512242d.
- [158] T. Torizuka, N. Tamaki, T. Inokuma, Y. Magata, S. Sasayama, Y. Yonekura, A. Tanaka, Y. Yamaoka, K. Yamamoto, and J. Konishi. “In vivo assessment of glucose metabolism in hepatocellular carcinoma with FDG-PET”. *Journal of Nuclear Medicine*, vol. 36, pp. 1811–1817, 1995.
- [159] M. L. Truong, T. Theis, A. M. Coffey, R. V. Shchepin, K. W. Waddell, F. Shi, B. M. Goodson, W. S. Warren, and E. Y. Chekmenev. “ ^{15}N -Hyperpolarization by reversible exchange using SABRE-SHEATH”. *Journal of Physical Chemistry C*, vol. 119, pp. 8786–8797, 2015. DOI: 10.1021/acs.jpcc.5b01799.
- [160] A. L. Vavere, G. B. Biddlecombe, W. M. Spees, J. R. Garbow, D. Wijesinghe, O. A. Andreev, D. M. Engelman, Y. K. Reshetnyak, and J. S. Lewis. “A novel technology for the imaging of acidic prostate tumors by positron emission tomography”. *Cancer Research*, vol. 69, pp. 4510–4516, 2009. DOI: 10.1158/0008-5472.Can-08-3781.
- [161] T. J. Vogl, S. Zangos, J. O. Balzer, M. Nabil, P. Rao, K. Eichler, W. O. Bechstein, S. Zeuzem, and A. Abdelkader. “Transarterial chemoembolization (TACE) in hepatocellular carcinoma: technique, indication and results”. *RöFo: Fortschritte auf dem Gebiet der Röntgenstrahlen und bildgebenden Verfahren*, vol. 179, pp. 1113–1126, 2007. DOI: 10.1055/s-2007-963285.
- [162] E. Waldmann, V. Prey, and F. Jelinek. “Zur Kenntnis der Brenztraubensäure”. *Monatshefte für Chemie und verwandte Teile anderer Wissenschaften*, vol. 85, pp. 872–881, 1954. DOI: 10.1007/BF00898714.
- [163] F. N. Wang, S. L. Peng, C. T. Lu, H. H. Peng, and T. C. Yeh. “Water signal attenuation by D_2O infusion as a novel contrast mechanism for ^1H perfusion MRI”. *NMR in Biomedicine*, vol. 26, pp. 692–698, 2013. DOI: 10.1002/nbm.2914.
- [164] X. Wang, D. C. Niu, Q. Wu, S. Bao, T. Su, X. H. Liu, S. J. Zhang, and Q. G. Wang. “Iron oxide/manganese oxide co-loaded hybrid nanogels as pH-responsive magnetic resonance contrast agents”. *Biomaterials*, vol. 53, pp. 349–357, 2015. DOI: 10.1016/j.biomaterials.2015.02.101.
- [165] F. Wiesinger, E. Weidl, M. I. Menzel, M. A. Janich, O. Khagai, S. J. Glaser, A. Haase, M. Schwaiger, and R. F. Schulte. “IDEAL spiral CSI for dynamic metabolic MR imaging of hyperpolarized $[1-^{13}\text{C}]$ pyruvate”. *Magnetic Resonance in Medicine*, vol. 68, pp. 8–16, 2012. DOI: 10.1002/mrm.23212.
- [166] D. M. Wilson, K. R. Keshari, P. E. Z. Larson, A. P. Chen, S. Hu, M. van Criekinge, R. Bok, S. J. Nelson, J. M. Macdonald, D. B. Vigneron, and J. Kurhanewicz. “Multi-compound polarization by DNP allows simultaneous assessment of multiple enzymatic activities in vivo”. *Journal of Magnetic Resonance*, vol. 205, pp. 141–147, 2010. DOI: 10.1016/j.jmr.2010.04.012.

- [167] T. H. Witney, M. I. Kettunen, D. E. Hu, F. A. Gallagher, S. E. Bohndiek, R. Napolitano, and K. M. Brindle. “Detecting treatment response in a model of human breast adenocarcinoma using hyperpolarised [1-¹³C]pyruvate and [1,4-¹³C₂]fumarate”. *British Journal of Cancer*, vol. 103, pp. 1400–1406, 2010. DOI: 10.1038/sj.bjc.6605945.
- [168] Ludwig Wolff. “II. Ueber die Parabrenztraubensäure”. *Justus Liebigs Annalen der Chemie*, vol. 305, pp. 154–165, 1899. DOI: 10.1002/jlac.18993050203.
- [169] Ludwig Wolff. “Ueber ein neues Condensationsproduct der Brenztraubensäure”. *Justus Liebigs Annalen der Chemie*, vol. 317, pp. 1–22, 1901. DOI: 10.1002/jlac.19013170102.
- [170] S. Woo, J. M. Lee, J. H. Yoon, I. Joo, J. K. Han, and B. I. Choi. “Intravoxel incoherent motion diffusion-weighted MR imaging of hepatocellular carcinoma: correlation with enhancement degree and histologic grade”. *Radiology*, vol. 270, pp. 758–767, 2014. DOI: 10.1148/radiol.13130444.
- [171] M. A. Worns and P. R. Galle. “HCC therapies – lessons learned”. *Nature Reviews Gastroenterology & Hepatology*, vol. 11, pp. 447–452, 2014. DOI: 10.1038/nrgastro.2014.10.
- [172] Y. Wu, W. Zhang, J. Li, and Y. Zhang. “Optical imaging of tumor microenvironment”. *American journal of nuclear medicine and molecular imaging*, vol. 3, pp. 1–15, 2013.
- [173] C. Yang, B. Ko, C. T. Hensley, L. Jiang, A. T. Wasti, J. Kim, J. Sudderth, M. A. Calvaruso, L. Lumata, M. Mitsche, J. Rutter, M. E. Merritt, and R. J. DeBerardinis. “Glutamine oxidation maintains the TCA cycle and cell survival during impaired mitochondrial pyruvate transport”. *Molecular Cell*, vol. 56, pp. 414–424, 2014. DOI: 10.1016/j.molcel.2014.09.025.
- [174] Y. F. Yen, P. Le Roux, D. Mayer, R. King, D. Spielman, J. Tropp, K. Butts Pauly, A. Pfefferbaum, S. Vasanawala, and R. Hurd. “T₂ relaxation times of ¹³C metabolites in a rat hepatocellular carcinoma model measured in vivo using ¹³C-MRS of hyperpolarized [1-¹³C]pyruvate”. *NMR in Biomedicine*, vol. 23, pp. 414–423, 2010. DOI: 10.1002/nbm.1481.
- [175] G. Zabow, S. J. Dodd, and A. P. Koretsky. “Shape-changing magnetic assemblies as high-sensitivity NMR-readable nanoprobess”. *Nature*, vol. 520, pp. 73–77, 2015. DOI: 10.1038/nature14294.
- [176] M. Zaiss and P. Bachert. “Chemical exchange saturation transfer (CEST) and MR Z-spectroscopy in vivo: a review of theoretical approaches and methods”. *Physics in Medicine and Biology*, vol. 58, R221–R269, 2013. DOI: 10.1088/0031-9155/58/22/R221.
- [177] S. R. Zhang, M. Merritt, D. E. Woessner, R. E. Lenkinski, and A. D. Sherry. “PARACEST agents: modulating MRI contrast via water proton exchange”. *Accounts of Chemical Research*, vol. 36, pp. 783–790, 2003. DOI: 10.1021/ar020228m.

- [178] S. R. Zhang, K. C. Wu, and A. D. Sherry. “A novel pH-sensitive MRI contrast agent”. *Angewandte Chemie – International Edition*, vol. 38, pp. 3192–3194, 1999. DOI: 10.1002/(SICI)1521-3773(19991102)38:21<3192::AID-ANIE3192>3.0.CO;2-%23.
- [179] X. M. Zhang, Y. X. Lin, and R. J. Gillies. “Tumor pH and its measurement”. *Journal of Nuclear Medicine*, vol. 51, pp. 1167–1170, 2010. DOI: 10.2967/jnumed.109.068981.
- [180] J. Y. Zhou, J. F. Payen, D. A. Wilson, R. J. Traystman, and P. C. M. van Zijl. “Using the amide proton signals of intracellular proteins and peptides to detect pH effects in MRI”. *Nature Medicine*, vol. 9, pp. 1085–1090, 2003. DOI: 10.1038/nm907.

List of publications

Peer-reviewed articles

1. Christian Hundshammer, **Stephan Düwel**, Simone S. Köcher, Malte Gersch, Benedikt Feuerecker, Christoph Scheurer, Axel Haase, Steffen J. Glaser, Markus Schwaiger, Franz Schilling. “Deuteration of hyperpolarized ^{13}C -labelled zymonic acid enables sensitivity-enhanced dynamic MRI of pH.” *ChemPhys-Chem* 18(18):2422–2425 (2017). DOI: 10.1002/cphc.201700779.
2. Christian Hundshammer, **Stephan Düwel**, Franz Schilling. “Imaging of extracellular pH using hyperpolarized molecules.” *Israel Journal of Chemistry* 57(9):788–799 (2017). DOI: 10.1002/ijch.201700017.
3. **Stephan Düwel**, Christian Hundshammer, Malte Gersch, Benedikt Feuerecker, Katja Steiger, Achim Buck, Axel Walch, Axel Haase, Steffen J. Glaser, Markus Schwaiger, Franz Schilling. “Imaging of pH in vivo using hyperpolarized ^{13}C -labeled zymonic acid.” *Nature Communications* 8:15126 (2017). DOI: 10.1038/ncomms15126.
4. **Stephan Düwel***, Markus Durst*, Concetta Gringeri, Yvonne Kosanke, Claudia Gross, Martin A. Janich, Axel Haase, Steffen J. Glaser, Markus Schwaiger, Rolf F. Schulte, Rickmer Braren, Marion I. Menzel. “Multiparametric HCC characterization and therapy response evaluation by hyperpolarized ^{13}C magnetic resonance spectroscopic imaging.” *NMR in Biomedicine* 29(7):952–960 (2016). DOI: 10.1002/nbm.3561. * contributed equally
5. Franz Schilling, **Stephan Düwel**, Ulrich Köllisch, Markus Durst, Rolf F. Schulte, Steffen J. Glaser, Axel Haase, Angela M. Otto, Marion I. Menzel. “Diffusion of hyperpolarized ^{13}C -metabolites in tumor cell spheroids using real-time NMR spectroscopy.” *NMR in Biomedicine* 26(5):557–568 (2013). DOI: 10.1002/nbm.2892.
6. Enrico Chiavazza, Eugen Kubala, Concetta V. Gringeri, **Stephan Düwel**, Markus Durst, Rolf F. Schulte, Marion I. Menzel. “Earth’s magnetic field enabled scalar coupling relaxation of ^{13}C nuclei bound to fast-relaxing quadrupolar ^{14}N in amide groups.” *Journal of Magnetic Resonance* 227:35–38 (2013). DOI: 10.1016/j.jmr.2012.11.016.

Patent application

Franz Schilling, **Stephan Düwel**, Malte Gersch, Steffen J. Glaser (inventors), Technische Universität München (applicant). “pH-biosensors based on compounds produced from pyruvic acid for magnetic resonance imaging and spectroscopy and their uses.” *World patent application* WO2015055727 (23 April 2015). English.

Book chapter

Jan-Bernd Hövener, Jessica A. M. Bastiaansen, Arnaud Comment, **Stephan Düwel**, Jan Henrik Ardenkjær-Larsen. “MRI: In vivo magnetic resonance imaging and spectroscopy with hyperpolarized agents.” In Fabian Kiessling, Bernd J. Pichler, Peter Hauff (Eds.), *Small Animal Imaging: Basics and Practical Guide* (2nd ed., pp. 286–301). Cham, Switzerland, Springer (2017). DOI: 10.1007/978-3-319-42202-2_13.

Conference contributions

1. **Stephan Düwel**, Christian Hundshammer, Malte Gersch, Benedikt Feueracker, Axel Haase, Steffen J. Glaser, Markus Schwaiger, Franz Schilling. “In vivo pH imaging using hyperpolarized ¹³C-labelled zymonic acid.” *Proc. Intl. Soc. Mag. Reson. Med.* 25:3341, Honolulu, USA (2017). **Oral Power Pitch Presentation.**
2. Christian Hundshammer, Miriam Braeuer, Christpoh Müller, Adam Espe Hansen, Jorge Cabello, Mathias Schillmaier, Benedikt Feuerecker, **Stephan Düwel**, Sylvia Schachoff, Birgit Blechert, Michael Michalik, Jan-Bernd Hövener, Steffen J. Glaser, Axel Haase, Franz Schilling, Andreas Kjaer, Stephan Nekolla, Markus Schwaiger. “Multiparametric tumor characterization using simultaneous ¹H-MRI, [¹⁸F]FDG PET and hyperpolarized [1-¹³C]pyruvate MRSI.” *Proc. Intl. Soc. Mag. Reson. Med.* 25:6097, Honolulu, USA (2017). Poster presentation.
3. **Stephan Düwel**, Christian Hundshammer, Malte Gersch, Benedikt Feueracker, Axel Haase, Steffen J. Glaser, Markus Schwaiger, Franz Schilling. “Imaging of pH in vivo using hyperpolarized ¹³C-labelled zymonic acid.” *4th International Workshop on Personalized Medicine*, Brisbane, Australia (2016). **Talk.**
4. **Stephan Düwel**, Christian Hundshammer, Malte Gersch, Benedikt Feueracker, Axel Haase, Steffen J. Glaser, Markus Schwaiger, Franz Schilling. “Imaging of pH in vivo using hyperpolarized ¹³C-labelled zymonic acid.” *European Molecular Imaging Meeting*, Utrecht, Netherlands (2016). **Talk.**

5. Christian Hundshammer, **Stephan Düwel**, Malte Gersch, Benedikt Feuerecker, Axel Haase, Steffen J. Glaser, Markus Schwaiger, Franz Schilling. “Characterization and deuterium enrichment of a novel ^{13}C enriched biosensor for pH-imaging.” *Proc. Intl. Soc. Mag. Reson. Med.* 24:5112, Singapore (2016). Poster presentation.
6. Alexander Joos, Norbert Löwa, **Stephan Düwel**, Christian Hundshammer, Frank Wiekhorst, Bernhard Gleich, Axel Haase. “Size-dependent MR relaxivities of magnetic nanoparticles.” *International Conference on the Scientific and Clinical Applications of Magnetic Carriers*, Vancouver, Canada (2016). Poster presentation.
7. **Stephan Düwel**, Christian Hundshammer, Malte Gersch, Benedikt Feuerecker, Axel Haase, Steffen J. Glaser, Markus Schwaiger, Franz Schilling. “A novel hyperpolarized biosensor for ^{13}C magnetic resonance spectroscopic imaging of pH.” *World Molecular Imaging Congress*, Honolulu, USA (2015). **Talk.**
8. Christian Hundshammer, **Stephan Düwel**, Malte Gersch, Benedikt Feuerecker, Axel Haase, Steffen J. Glaser, Markus Schwaiger, Franz Schilling. “Characterization and deuterium enrichment of a novel biosensor for pH-imaging.” *World Molecular Imaging Congress*, Honolulu, USA (2015). Poster presentation.
9. **Stephan Düwel**, Christian Hundshammer, Malte Gersch, Benedikt Feuerecker, Axel Haase, Steffen J. Glaser, Markus Schwaiger, Franz Schilling. “A new ^{13}C -labeled biosensor for hyperpolarized magnetic resonance spectroscopic imaging of pH in vivo.” *International Conference on Magnetic Resonance Microscopy*, Munich, Germany (2015). **Talk.**
10. **Stephan Düwel**, Malte Gersch, Benedikt Feuerecker, Christian Hundshammer, Markus Schwaiger, Steffen J. Glaser, Franz Schilling. “A novel pH-biosensor for magnetic resonance imaging and spectroscopy.” *BioVaria*, Munich, Germany (2014). Poster presentation.
11. **Stephan Düwel**, Patrick Christ, Ulrich Köllisch, Markus Durst, Concetta Gringeri, Franz Schilling, Marion I. Menzel, Rolf F. Schulte, Steffen J. Glaser, Markus Schwaiger, Axel Haase. “Thermal T_1 measurements for frequently used ^{13}C hyperpolarization agents at clinically available field strengths.” *Proc. Intl. Soc. Mag. Reson. Med.* 22:2772, Milan, Italy (2014). Poster presentation.
12. **Stephan Düwel**, Markus Durst, Concetta V. Gringeri, Yvonne Kosanke, Claudia Gross, Martin A. Janich, Markus Schwaiger, Axel Haase, Steffen J. Glaser, Rolf F. Schulte, Rickmer Braren, Marion I. Menzel. “Simultaneous examination of metabolism and perfusion of embolized hepatocellular carcinoma in rats by hyperpolarized fumarate and copolarization of pyruvate and urea.” *Proc. Intl. Soc. Mag. Reson. Med.* 21:0656, Salt Lake City, USA (2013). **Talk.**

13. Enrico Chiavazza, Eugen Kubala, Concetta V. Gringeri, **Stephan Düwel**, Markus Durst, Rolf F. Schulte, Marion I. Menzel. “Hyperpolarization quenching in ^{13}C nuclei bound to fast relaxing quadrupolar ^{14}N mediated by scalar coupling relaxation in amide groups exposed to Earth’s magnetic field.” *Proc. Intl. Soc. Mag. Reson. Med. 21:1919*, Salt Lake City, USA (2013). Poster presentation.
14. Markus Durst, **Stephan Düwel**, Concetta V. Gringeri, Yvonne Kosanke, Claudia Gross, Rickmer Braren, Axel Haase, Marion I. Menzel, Rolf F. Schulte. “Multiband excitation pulses for treatment response studies with hyperpolarized ^{13}C fumarate.” *Proc. Intl. Soc. Mag. Reson. Med. 21:1931*, Salt Lake City, USA (2013). Poster presentation.
15. Franz Schilling, **Stephan Düwel**, Ulrich Köllisch, Markus Durst, Steffen J. Glaser, Axel Haase, Marion I. Menzel, Angela M. Otto. “Ratio of lactate-to-pyruvate apparent diffusion coefficients is an indicator of necrosis in tumor cells.” *Proc. Intl. Soc. Mag. Reson. Med. 21:3921*, Salt Lake City, USA (2013). Poster presentation.
16. **Stephan Düwel**, Christian Schneider, Martin Enderlein, Thomas Huber, Manuel Mielenz, Johannes Ströhle, Tobias Schätz. “Frequency-quadrupled 285 nm diode laser system for photoionization of Mg using LBO as a second harmonic generation crystal.” German Physical Society Spring Conference, Dresden, Germany (2011). Poster presentation.
17. **Stephan Düwel**, Christian Schneider, Thomas Huber, Martin Enderlein, Johannes Ströhle, Tobias Schätz. “Optical trapping of an ion - a new route towards scalable quantum simulations.” European Conference on Trapped Ions, Durham, England (2010). Poster presentation.
18. **Stephan Düwel**, Christian Schneider, Martin Enderlein, Thomas Huber, Tobias Schätz. “Cooling of an optically trapped ion.” German Physical Society Spring Conference, Hannover, Germany (2010). Poster presentation.

Curriculum vitae

Academic education

- 06/2011–10/2017 **Doctoral studies** at the *Technische Universität München*, supervised by Prof. Steffen J. Glaser, *Department of Chemistry*, Prof. Axel Haase, *Munich School of BioEngineering* and Prof. Markus Schwaiger, *Department of Nuclear Medicine*.
- 01/2011–04/2011 Research assistant,
Max-Planck-Institute of Quantum Optics, Garching, Germany.
- 12/2010 **Diploma** in physics with honors, grade 1.06,
Ludwig-Maximilians-Universität, Munich, Germany.
- 11/2009–12/2010 **Diploma thesis**, “Messung der Temperatur von optisch gefangenen Ionen” in the laboratory of Dr. Tobias Schätz, Erstgutachter Prof. Dietrich Habs, *Max-Planck-Institute of Quantum Optics*, Garching, Germany.
- 09/2007–07/2008 Studies of physics as visiting special student,
California Institute of Technology, Pasadena, USA.
- 05/2006 **Prediploma** in physics, grade 1.11,
Ludwig-Maximilians-Universität, Munich, Germany.
- 10/2004–11/2009 Studies of physics,
Ludwig-Maximilians-Universität, Munich, Germany.
- 08/2003–05/2004 Civilian service in general hospital,
Kreisklinik Ebersberg, Ebersberg, Germany.
- 06/2003 **Abitur**, grade 1.0,
Gymnasium Grafing, Grafing, Germany.

Scholarships and awards

- 04/2017 Educational Stipend for attending the 25th annual conference of the International Society for Magnetic Resonance in Medicine (*ISMRM*), Honolulu, USA.
- 03/2016 **Young Investigator Award**, 11th European Molecular Imaging Meeting (*EMIM*), European Society for Molecular Imaging (*ESMI*), Utrecht, Netherlands, for the presentation on “Imaging of pH in vivo using hyperpolarized ¹³C-labelled zymonic acid”.
- 09/2015 Student Travel Stipend Award in recognition of the excellence of the abstract submission to the annual conference of the World Molecular Imaging Society (*WMIS*) in Honolulu, USA.
- 05/2014 Educational Stipend for attending the 22nd annual conference of the International Society for Magnetic Resonance in Medicine (*ISMRM*), Milan, Italy.
- 04/2013 **ISMRM Merit Award Magna Cum Laude**, 21st annual conference of the International Society for Magnetic Resonance in Medicine (*ISMRM*), Salt Lake City, USA, for the abstract of the presentation on “Simultaneous examination of metabolism and perfusion of embolized hepatocellular carcinoma in rats by hyperpolarized fumarate and copolarization of pyruvate and urea”.
- 04/2013 Educational Stipend for attending the 21st annual conference of the International Society for Magnetic Resonance in Medicine (*ISMRM*), Salt Lake City, USA.
- 03/2011 Stipend of the *Wilhelm and Else Heraeus-Foundation* for attending the spring conference of the German Physical Society (*DPG*), Dresden, Germany.
- 03/2010 Stipend of the *Wilhelm and Else Heraeus-Foundation* for attending the spring conference of the German Physical Society (*DPG*), Hannover, Germany.
- 2007 – 2008 Full scholarship, *Fulbright*, *California Institute of Technology*, Pasadena, USA.
- 2005 – 2010 Scholarship, *Max-Weber-Programm* of the *Studienstiftung des deutschen Volkes* within the *Bayerische Exzellenzförderung*.
- 2003 – 2005 Scholarship, *Bayerisches Begabtenförderungsgesetz*.
- 2003 – 2011 Scholarship, *Stiftung Maximilianeum*, Munich, Germany.
- 07/2002 Attendee, *Deutsche Schüler Akademie*, Marburg, Germany.
- 2000 – 2001 Full scholarship, American Secondary Schools for International Students and Teachers (*ASSIST*) exchange program at *St. Paul's School*, Concord, New Hampshire, USA.

Teaching

- 01/2014–02/2014 Supervision of laboratories and seminars of organic chemistry in the programs of biochemistry-molecular biotechnology (*BC-MBT*) and chemical engineering (*CIW*).
- 01/2013–02/2013 Supervision of laboratories and seminars of organic chemistry in the programs of biochemistry-molecular biotechnology (*BC-MBT*) and chemical engineering (*CIW*).
- 03/2012–04/2012 Supervision of laboratories of chemistry and biochemistry in the program of management and technology (*TUM-BWL*).

Acknowledgements

“I like to listen. I have learned a great deal from listening carefully.”

— Ernest Hemingway (* 1899; † 1961)

During my time at the *Department of Nuclear Medicine*, the *Department of Chemistry*, the *Munich School of BioEngineering* and *GE Global Research*, many people supported and inspired me, and this thesis would not have been possible without them. Without making the claim to be complete, I would like to thank:

- | Ψ \rangle *Prof. Steffen Glaser* for his inspirational enthusiasm for unsolved problems, for sharing his scientific knowledge and for giving me the freedom to pursue my own research interests.
- | Ψ \rangle *Prof. Axel Haase* for introducing me into the exciting field of NMR physics, for his support of my scientific projects and for sharing his extensive scientific network with his students.
- | Ψ \rangle *Prof. Markus Schwaiger* for his scientific support, for providing extensive funding and for successfully motivating a large group of people to work together towards a common goal in a truly great atmosphere.
- | Ψ \rangle *Franz Schilling* for involving me in the exciting “unknown-peak-puzzle”, for his enthusiasm for research at large and for being a wonderful mentor and friend.
- | Ψ \rangle *Dr. Marion Menzel* and *Dr. Rickmer Braren* for their persistence in publishing scientific results and for being available for advice whenever needed.
- | Ψ \rangle *Christian Hundhammer* for his help in all kinds of practical and theoretical biochemistry problems even at utterly impossible times of the day.
- | Ψ \rangle *Markus Durst*, *Ulrich Köllisch*, *Tim Sprenger*, *Johannes Scholz* and *Patrick Christ* for scientific help during a great time in the hyperpolarization group put together by Prof. Haase.

- $|\Psi\rangle$ *Dr. Rolf Schulte, Concetta Gringeri, Enrico Chiavazza and Eugen Kubala* for the good cooperation with *GE Global Research*.
- $|\Psi\rangle$ *Dr. Raimund Marx* for his assistance with everything involving chemical compounds, *Simone Köcher* for her help in running simulations to shed light on chemical structures under the influence of pH, *Ariane Garon* for pleasant lunchtime conversations in French and all members of the *Glaser group* for their diverse seminar presentations.
- $|\Psi\rangle$ *Dr. Bernhard Gleich, PD Dr. Angela Otto, Josef Hintermair, Alex Joos, Thomas Gaaß and Katharina Lang* for the nice atmosphere at the *Munich School of BioEngineering* and their help whenever needed.
- $|\Psi\rangle$ *Michael Michalik, Dr. Katja Steiger, Dr. Claudia Groß, Dr. Yvonne Kosanke, Miriam Mohring, Birgit Blechert, Sibylle Reeder, Markus Mittelhäuser, Geoff Topping and Piotr Dzien* from the *Department of Nuclear Medicine* for their assistance with tasks when otherwise I would have been lost.
- $|\Psi\rangle$ *Nahid Yusufi, Fabian Lohöfer, Andreas Poschenrieder, Antonia Richter and Sabine Mall* for creating a delightful atmosphere in and around the *Department of Nuclear Medicine*.
- $|\Psi\rangle$ *Dr. Christof Seidl* for giving me the opportunity to take an informative and wonderful trip to Brisbane.
- $|\Psi\rangle$ *Will Mander* from *Oxford Instruments* for i.a. saving our Hypersense polarizer from quenching.
- $|\Psi\rangle$ *Dr. Arnaud Comment* and *Prof. Jan Henrik Ardenkjaer-Larsen* for the pleasant cooperation working on the book chapter.
- $|\Psi\rangle$ *Achim Buck* and *Prof. Axel Walch* for the uncomplicated cooperation with the analytical pathology of the *Helmholtz Zentrum München*.
- $|\Psi\rangle$ *Malte Gersch* for a dauntless approach to outdated chemical synthesis instructions, *apl. Prof. Wolfgang Eisenreich* for an enlightening discussion as well as *Prof. Stephan Sieber* and *Prof. Bernd Reif* for selflessly granting access to their laboratories in the *Department of Chemistry*.
- $|\Psi\rangle$ *Jan-Bernd Hövener* and *Jessica Bastiaansen* for a long-lasting scientific and personal friendship.
- $|\Psi\rangle$ *Anna Bartels, Zohreh Varasteh* and *Benedikt Feuerecker* for the outstanding atmosphere in our office and for introducing me into three completely different but equally interesting ways of life.
- $|\Psi\rangle$ *My parents, my sister* and *my wife Charlotte* for your continuous support.